# COOPERATIVE WAVE MIXING IN ATOMS AND SOLIDS

A Dissertation

by

ZHENHUAN YI

Submitted to the Office of Graduate and Professional Studies of
Texas A&M University
in partial fulfillment of the requirements for the degree of

DOCTOR OF PHILOSOPHY

Chair of Committee, Marlan O. Scully
Committee Members, Alexei V. Sokolov
George R. Welch
Aleksei M. Zheltikov
Philip Hemmer
Head of Department, George R. Welch

May 2016

Major Subject: Physics

# ABSTRACT

Enhancing optical signal is a subject of long term interest with many applications, such as trace chemical detection in the lab and standoff detection in the atmosphere. It is well known that optical properties of multi-level atomic and molecular system can be controlled and manipulated efficiently using quantum coherence and interference resulting an enhancement in optical signals. In this dissertation we investigate methods both with/without utilizing coherence of atomic and molecular systems to enhance optical signals. We use resonant Raman scattering and surface-enhanced Raman scattering which do not rely on molecular coherence to boost Raman signal from molecules, several orders of magnitude enhancement has been achieved. When coherence is introduced into atomic systems, cooperative emission is produced as a result of coherence. The emission is named Superfluorescence (SF) or superradiance (SR) depending on the initial coherence of the prepared systems. We study the properties of SF, yoked SF (YSF) and SR, the transition from YSF to SR and quantum beat exhibits in YSF/SR signal. More than thirty folds of pulse energy is obtained from SR compare to that of YSF. Possible applications of these results are also discussed.

# ACKNOWLEDGEMENTS

I hereby thank all my family, my advisor, my colleagues, and my friends for their support and help during the years of my Ph.D study.

I sincerely thank my advisor, Marlan O. Scully, who has given me various opportunities to study and research in the field of quantum optics; his sharp instinct for physics and his teaching of philosophy in scientific career always inspire me, not to mention his kind support on many aspects of life. I also would like to thank my committee members: Philip Hemmer, Alexei V. Sokolov, George R. Welch and Aleksei M. Zheltikov for guiding and helping me in my research. Many thanks are owed to the teachers who gave wonderful classes during these years: Roland E. Allen, Katrin Becker, Alexey Belyanin, Edward Fry, Dudley Herschbach, Teruki Kamon, Saskia Mioduszewski, Christopher Pope, Valery Pokrovsky, M. Suhail Zubairy and Thomas Weimar. I also learned a lot from my colleagues: Narangerel Altangerel, Gombojav O. Ariunbold, Charles W. Ballmann, Tuguldur Begzjav, Han Cai, Ziyun Di, Konstantin E. Dorfman, Chengwei Huang, Pankaj K. Jha, Matthew T. Morrison, Yuri V. Rostovtsev, Vladmir A. Sautenkov, Alexander M. Sinyukov, Anton Shutov, Jonathan V. Thompson, Dmitri V. Voronine, Kai Wang, Luqi Yuan, Kimberly R. Chapin, Selina Garcia, Patrick Philpot, Clayton Holle, Jason Caswell, Steve Payne, Yujie Shen, Feng Zhu, Xiwen Zhang, Anatoly Svidzinsky, Hui Dong, Moochan Kim, Luojia Wang, Chris O'brian, Dawei Wang, Tao Peng, Shengwen Li and many others. Their help made this dissertation possible. I also thank all my friends for giving me a wonderful time in College Station.

I would like to thank my family (my wife, Hong Wan, my sons, Aaron and Christopher, and my parents) for accompanying and supporting me; they are always there for me, giving me strength and a lovely home.

# TABLE OF CONTENTS

# LIST OF FIGURES

# LIST OF TABLES

# 1. INTRODUCTION

“Let there be light”, and there was light. And light is, not only essential for one of the most important perceptions for human being, vision, but also crucial for development of the subject of physics: from the Michelson-Morley experiment to special relativity [2], from the Lamb shift to quantum electrodynamics [3], just to name a few. The human eye is very sensitive to green light: even a few photons of green light can catch one’s attention in a dark room. But in another sense, the human eye is not quite sensitive, i.e., in capability of resolving the frequency of light.

When monochromatic light scatters from a substrate (either gas, liquid or solid phase), away from absorption lines of the substrate, of course, most likely the light would come out without changing its frequency. But there is a small probability, about one out of a million, it shifts its frequency. The former case is called Rayleigh scattering, while the later is named Raman scattering, and the corresponding shift is called the Raman shift [4].

It is found that Raman shifts correspond to vibrational or rotational transitions of the scattering molecule that composed the substrate. By studying the pattern and intensity of the Raman lines, a lot of molecular information was uncovered. In general, different molecule has different features in its Raman spectra thus make the Raman spectrum the “finger prints” for molecules. Raman signal is typically so weak, acquiring a Raman spectrum takes a good amount of light and substrates and time.

Enhancing optical signal is, in general, a subject of long term interest with many applications, such as trace chemical detection in the lab and standoff detection in the atmosphere. In the lab, either under microscope or on the optical table, people have been using many ways to enhance the Raman signal; among them are the resonant enhanced Raman and surface-enhance Raman [5, 6] and even tip-enhanced Raman scattering [7], which does not need to account for coherence in the molecular system. It is also well known that optical properties of multi-level atomic and molecular systems can be controlled and manipulated efficiently using quantum coherence and interference resulting an enhancement in optical signals. Coherent anti-Stokes Raman Scattering is an example of using coherence of molecules to boost the signal [8, 9].

In the standoff detection/remote sensing side, the conventional atmospheric light detection and ranging (LIDAR) techniques [10, 11] have essential tools for detecting traces of air impurity at long distances. A tremendous amount of research has been devoted to upgrading conventional LIDAR techniques. Recently, coherent standoff spectroscopic (SOS) techniques have been proposed [12, 13]. In particular, one SOS technique [12] is intended to maintain a backward swept-gain for the successive two-photon induced superradiance (SR) [14, 15] or superfluorescence (SF) [16, 17] emissions. High-gain, directional backward SF emissions have been observed in air [18, 19, 20]. In this dissertation, our interest spans from generation and propagation of such SF pulses in atomic vapor and studying the properties of the pulses, enhancing the correlated emission, Yoked SF (YSF) [21], by driving YSF into SR, to quantum beat exhibits in YSF/SR signal. Some applications will also be discussed, such as probing dipole-dipole interaction and wave package control. The following sections outline the topics.

## 1.1 Enhanced signal in Resonant Raman and Surface-Enhanced Raman spectroscopy

As the first example of method without using atomic/molecular coherence to enhancing optical signal, an ultralow-power diode-laser radiation is employed to induce photodesorption [22, 23, 24, 25] of cesium from a partially transparent thin-film cesium adsorbate on a solid surface. Using resonant Raman scattering, which utilizes resonant transition in cesium molecules to enhance Raman signal by several orders of magnitude, we demonstrate that this photodesorption process enables an accurate local optical control of the density of dimer molecules in alkali-metal vapors.

Surface-enhanced Raman scattering (SERS) is another example of method using no coherence in the molecular system. SERS of rhodamine 6G was investigated on template-embedded gold nanorods produced by anodic aluminum oxide template-assisted nanofabrication. A signal enhancement factor of about $10^6$ was obtained. SERS substrate design principles were investigated in order to achieve maximum electromagnetic enhancement of both the incident and Raman-scattered fields.

### 1.2 Quantum coherence: from Yoked superfluorescence to superradiance

When coherence is introduced into an atomic system, cooperative emission as a result of coherence in the system can emit, faster than the single atom decay, a directional beam in a solid angle much smaller than the $4\pi$-angle of emissions such as spontaneous emission and Raman scattering signal. SF and SR are the names of the emissions depending on the initial coherence of the prepared system. Studies are carried out in atomic vapors. We study backward cooperative emissions from a dense sodium atomic vapor. Ultrashort pulses produced from a conventional amplified femtosecond laser system with an optical parametric amplifier are used to excite sodium atoms resonantly on the two-photon $3S_{1/2}{-}4S_{1/2}$ transition. Backward SF emissions (BSFEs), both on the $4S_{1/2} - 3P_{3/2}$ and $4S_{1/2} - 3P_{1/2}$ transitions, are observed. The picosecond temporal characteristics of the BSFE are observed using an ultrafast streak camera. The power laws for the dependencies of the average time delay and the intensity of the BSFEs on input power are analyzed in the sense of cooperative emission from non-identical atomic species. As a result, an absolute (rather than relative) time delay and its fluctuations (free of any possible external noise) are determined experimentally. The possibility of a backward swept-gain SF as an artificial laser guide star in the sodium layer in the mesosphere is also discussed.

We also investigate cooperative emissions from a rubidium vapor, and demonstrate a controlled transition from yoked SF to three-photon-induced SR by driving the medium with co-propagating ultrashort laser pulses, 30 folds more signal intensity is obtained in the case of SR. We study their temporal profiles and time delays on a picosecond time scale and compare the measured pulse shapes with simulations. Our results suggest strategies to improve efficiency of mirrorless lasers and SR light sources.

When the system transits from YSF to SR as we increase the pulse energy in the probe pulse, the delay between the SF and pump pulse is gradually reduced to that of SR, the probe pulse energy serves as a control knob. More interesting results are also obtained when the time delay between the pump and probe pulses are scanned. Quantum beat from coupled dual pathways, as a result of the scan, can be used to reveal dipole-dipole interaction and multi-photon (>5) interaction in the system we study. The phase of the beat pattern, which indicates the phase of excited wave package, could be controlled by fine tuning the spectrum of the pump pulse and/or by adding one more pump pulse to interfere with the other.

# 2. SEMICLASSICAL THEORY OF ATOM-FIELD INTERACTION

In this chapter, we will present some of the theoretical concepts and tools we often use in the study of interaction between radiation field and matter. The so-called semiclassical theory treats the atom quantum-mechanically while the radiation field is treated as a classical electromagnetic field. There are some good text books [3, 26] discuss the basics and many advanced topics in the field of quantum optics, one would surely be well equipped by reading them. Here, we first introduce an example of a two-level system interacting with a single mode of electromagnetic field. Then we will extend the discussion to three or more level systems. The concepts and tools will be naturally introduced during the discussion.

## 2.1 Electrical dipole approximation and interaction Hamiltonian

Let's start with Schrödinger equation (SE) with a minimal-coupling Hamiltonian which describes an electron interacts with an external electromagnetic (EM) field, which reads

$$\left\{-\frac{\hbar^2}{2m}\left[\nabla - i\frac{e}{\hbar}\mathbf{A}(\mathbf{r},t)\right]^2 + eU(\mathbf{r},t) + V(r)\right\}\psi(\mathbf{r},t) = i\hbar\frac{\partial\psi(\mathbf{r},t)}{\partial t}, \tag{2.1}$$

where $e$ is charge and $m$ is mass of the electron; $U$ is scalar and $\mathbf{A}$ is vector potentials of the EM field; $V(r)$ is the static potential which is usually the binding potential. We use radiation gauge, in which $U(\mathbf{r},t) = 0$ and $\nabla \cdot \mathbf{A} = 0$. Consider the electron is bound by the nuclear potential $V(r)$, and assume the nuclear is located at $\mathbf{r}_0$. If the wavelength of the EM field is much larger than the size of the bounded system (the atom), the dipole approximation is valid, and we can replace $\mathbf{A}(\mathbf{r},t)$ with $\mathbf{A}(\mathbf{r}_0,t)$, so the equation can be written as

$$\left\{-\frac{\hbar^2}{2m}\left[\nabla - i\frac{e}{\hbar}\mathbf{A}(\mathbf{r}_0,t)\right]^2 + V(r)\right\}\psi(\mathbf{r},t) = i\hbar\frac{\partial\psi(\mathbf{r},t)}{\partial t}. \tag{2.2}$$

Next we apply a gauge transformation

$$\psi(\mathbf{r},t) \to \psi(\mathbf{r},t)e^{i\chi(\mathbf{r},t)}, \tag{2.3}$$

with $\chi(\mathbf{r},t) = -e\mathbf{A}(\mathbf{r}_0,t)\cdot\mathbf{r}/\hbar$, thus

$$\begin{aligned} \mathbf{A}(\mathbf{r}_0,t) \quad &\to \quad \mathbf{A}(\mathbf{r}_0,t) + \frac{\hbar}{e}\nabla\chi(\mathbf{r},t) = 0, && (2.4)\\ U(\mathbf{r},t) \quad &\to \quad U(\mathbf{r},t) - \frac{\hbar}{e}\frac{\partial}{\partial t}\chi(\mathbf{r},t) = \mathbf{r}\cdot\frac{\partial}{\partial t}\mathbf{A}(\mathbf{r}_0,t). && (2.5) \end{aligned}$$

Note that radiation gauge implies that $\mathbf{E} = -\nabla U - \frac{\partial \mathbf{A}}{\partial t} = -\frac{\partial \mathbf{A}}{\partial t}$ and $\mathbf{B} = \nabla \times \mathbf{A}$, the Schrödinger equation now reads

$$\left\{-\frac{\hbar^2}{2m}\nabla^2 + V(r) - e\mathbf{r}\cdot\mathbf{E}(\mathbf{r}_0,t)\right\}\psi(\mathbf{r},t) = i\hbar\frac{\partial\psi(\mathbf{r},t)}{\partial t}, \tag{2.6}$$

with total Hamiltonian

$$H = H_0 + H_1, \tag{2.7}$$

where

$$H_0 = \frac{p^2}{2m} + V(r), \tag{2.8}$$

is the unperturbed Hamiltonian of the electron and

$$H_1 = -e\mathbf{r}\cdot\mathbf{E}(\mathbf{r}_0,t), \tag{2.9}$$

is the Hamiltonian describes atom-field interaction. Once we get the explicit expression of $V(r)$, then the SE with $H_0$ can be solved approximately with good enough accuracy in many cases. The light-atom interaction term $H_1$ is then treated as a perturbation to the unperturbed system. Assume that we have found the eigenstates of $H_0$, $\psi_i(\mathbf{r},t)$, which satisfies $H_0\psi_i = E_i\psi_i$, $i = a, b, c\ldots$, we can present $H_0$ in its own eigenstate representation. Using the bra ($\langle\,|$)and ket ($|\,\rangle$) notation, $\psi_i = |i\rangle$ and its complex conjugate is $\psi_i^* = \langle i|$. Using the completeness relation $\sum_i |i\rangle\langle i| = \mathbf{1}$, $H_0$ can be represented as

$$H_0 = \sum_{i,j} |i\rangle\langle i|H_0|j\rangle\langle j| = \sum_i E_i|i\rangle\langle i| = \sum_i \hbar\omega_i|i\rangle\langle i|, \tag{2.10}$$

where we have used $E_i = \hbar\omega_i$ . Similarly, we can express $H_1$ as

$$\begin{aligned} H_1 &= -e\mathbf{r}\cdot\mathbf{E}(\mathbf{r}_0,t) \\ &= -e\sum_{i,j}|i\rangle\langle i|\mathbf{r}|j\rangle\langle j|\cdot\mathbf{E}(t) \\ &= -\sum_{i,j}\wp_{ij}|i\rangle\langle j|\cdot\mathbf{E}(t), \end{aligned} \tag{2.11}$$

where $\wp_{ij} = \wp_{ji}^* = e\langle i|\mathbf{r}|j\rangle$ is the matrix element of the electric dipole moment and $\mathbf{E}(t)$ is the field at the atom, we omit the $\mathbf{r}_0$ since it is a constant here (position of the nuclear). The strength of the dipole moment $|\wp_{ij}|$ and the polarization of the radiation field is determined by the selection rules of the dipole transition. More discussions on selection rules can be found in many text books [1, 27, 28]. In the following section, we first consider a two-level system ($i = a,\ b$) interaction with a monochromatic field ($E(t) = \mathscr{E}\cos\nu t$), polarized in the $\hat{x}$ direction. It is easy to find

$$\begin{aligned} H_1 &= -\left[\wp_{ab}\mathscr{E}|a\rangle\langle b| + \wp_{ba}\mathscr{E}|b\rangle\langle a|\right]\cos\nu t \\ &= -\hbar\left[\Omega_R e^{-i\phi}|a\rangle\langle b| + \Omega_R e^{i\phi}|b\rangle\langle a|\right]\cos\nu t, \end{aligned} \tag{2.12}$$

where the Rabi frequency is $\Omega_R = \frac{|\wp_{ab}|\mathscr{E}}{\hbar}$, and $\wp_{ba} = |\wp_{ba}|e^{i\phi}$.

## 2.2 Interaction picture

Solving SE can be done in different pictures. In Schrödinger picture, the wave function $|\psi(\mathbf{r},t)\rangle$ carries the evolution of the quantum system. For a two-level system, the general wave function can be written as

$$|\psi(t)\rangle = C_a(t)|a\rangle + C_b(t)|b\rangle, \tag{2.13}$$

where $C_a$ and $C_b$ are the probability amplitudes for each eigenstate. Plugging it into the SE,

$$\frac{d}{dt}|\psi(t)\rangle = -\frac{i}{\hbar}(H_0 + H_1)|\psi(t)\rangle, \tag{2.14}$$

we get

$$\dot{C}_a(t) = -i\omega_a C_a + i\Omega_R e^{-i\phi}\cos(\nu t)C_b, \tag{2.15}$$

$$\dot{C}_b(t) = -i\omega_b C_b + i\Omega_R e^{i\phi}\cos(\nu t)C_a, \tag{2.16}$$

where "$\cdot$" means time derivative. We can introduce a slowly varying amplitudes:

$$c_a = C_a e^{i\omega_a t}, \tag{2.17}$$

$$c_b = C_b e^{i\omega_b t}, \tag{2.18}$$

Then it follows that

$$\dot{c}_a = i\frac{\Omega_R}{2}e^{-i\phi}c_b\left[e^{i(\omega-\nu)t}+e^{i(\omega+\nu)t}\right], \tag{2.19}$$

$$\dot{c}_b = i\frac{\Omega_R}{2}e^{i\phi}c_a\left[e^{-i(\omega-\nu)t}+e^{-i(\omega+\nu)t}\right], \tag{2.20}$$

where $\omega = \omega_a - \omega_b$. When the radiation frequency $\nu$ is close to transition frequency $\omega$, the second exponential terms with $\pm(\omega+\nu)$ oscillate much faster than the first and they usually average to a very small contribution during a time interval $\Delta t > 1/(\omega-\nu)$; by ignoring these two terms we make a rotating-wave approximation (RWA). Then these two coupled equations can be readily solved. And using the probability amplitudes we can evaluate the average value of any operators, $\langle O\rangle = \langle\psi(t)|O|\psi(t)\rangle$.

In Heisenberg picture, $|\psi(t)\rangle = U(t)|\psi(t=0)\rangle$, the unitary operator $U(t) = e^{-iHt/\hbar}$ carries the evolution of the system. We introduce another very useful picture, the interaction picture, by assuming $|\psi(t)\rangle = U_0(t)|\psi_I(t)\rangle$, with $U_0(t) = e^{-iH_0t/\hbar}$. As we will show below, $|\psi_I(t)\rangle$ carries the evolution of the system that has been caused only by interaction between the field and the atom. It is interesting to see that when we introduce $c_a$ and $c_b$ in equations (2.17) and (2.18), we are actually solving the problem in the interaction picture, by noticing that

$$\begin{aligned}|\psi_I(t)\rangle &= U_0^\dagger|\psi(t)\rangle\\ &= e^{-iHt/\hbar}\left(C_a(t)|a\rangle + C_b(t)|b\rangle\right)\\ &= C_a e^{i\omega_a t}|a\rangle + C_b e^{i\omega_b t}|b\rangle\\ &= c_a(t)|a\rangle + c_b(t)|b\rangle.\end{aligned} \tag{2.21}$$

To work in the interaction picture, we need to find the form of SE in this picture, which is

$$\begin{aligned}
i\hbar\frac{\partial}{\partial t}|\psi\rangle_I &= i\hbar\frac{\partial}{\partial t}[U_0^\dagger(t)|\psi\rangle] \\
&= i\hbar\{\frac{\partial}{\partial t}[U_0^\dagger(t)]|\psi\rangle + U_0^\dagger\frac{\partial}{\partial t}[|\psi\rangle]\} \\
&= (-H_0 + H_0 + U_0^\dagger V U_0)|\psi\rangle_I \\
&= \mathscr{V}(t)|\psi\rangle_I, \qquad (2.22)
\end{aligned}$$

where $\mathscr{V}(t) = U_0^\dagger V U_0$, assuming that $H = H_0 + V$. And from

$$H_0^n = (\hbar\omega_a)^n\, |a\rangle\langle a| + (\hbar\omega_b)^n\, |b\rangle\langle b|, \qquad (2.23)$$

we get

$$U_0 = e^{-i\omega_a t}|a\rangle\langle a| + e^{-i\omega_b t}|b\rangle\langle b|, \qquad (2.24)$$

and

$$\begin{aligned}
\mathscr{V}(t) = U_0^\dagger V U_0 &= -\hbar\Omega_R U_0^\dagger \left(e^{-i\phi}|a\rangle\langle b| + e^{i\phi}|b\rangle\langle a|\right)\cos\nu t \\
&= -\frac{\hbar\Omega_R}{2}\left(e^{-i\phi}|a\rangle\langle b|e^{i\omega t} + e^{i\phi}|b\rangle\langle a|e^{-i\omega t}\right)\left(e^{i\nu t} + e^{-i\nu t}\right). \qquad (2.25)
\end{aligned}$$

After RWA, we can get

$$\mathscr{V}(t) = -\frac{\hbar\Omega_R}{2}\left(e^{-i\phi}|a\rangle\langle b|e^{i(\omega-\nu)t} + e^{i\phi}|b\rangle\langle a|e^{-i(\omega-\nu)t}\right). \qquad (2.26)$$

In general the transformation adds a $e^{i(\omega_i-\omega_j)t}$ factor to the $|i\rangle\langle j|$ term. The equation can be further solved using the probability amplitude method or the perturbation expansion method often used in Heisenberg picture

$$|\psi_I(t)\rangle = U_I|\psi_I(t=0)\rangle, \tag{2.27}$$

where the time-evolution operator in interaction picture is

$$\begin{aligned} U_I(t) &= \mathscr{T}\exp\left[-\frac{i}{\hbar}\int_0^t \mathscr{V}(\tau)d\tau\right] \\ &= 1-\frac{i}{\hbar}\int_0^t dt_1\mathscr{V}(t_1)+\left(-\frac{i}{\hbar}\right)^2\int_0^t dt_1\int_0^{t_1} dt_2\mathscr{V}(t_1)\mathscr{V}(t_2)+\ldots. \end{aligned} \tag{2.28}$$

We will show examples using this method to calculate transition amplitudes between multi-levels through multi-photon processes in appendices A and B.

### 2.3 Enhancement factors in Resonance Raman and surface-enhanced Raman scattering

In Raman process, when the excitation wavelength is close to or in resonance with the electronic states of a molecule, the resonance Raman scattering (RRS) occurs. The resonance Raman scattering has long been a very important tool complementary to the non-resonance Raman scattering in the study of molecular properties [4, 29]. The enhanced cross section for RRS can be easily understand by noticing that the polarizability tensor has a Lorentzian profile factor

$$\frac{1}{\omega_{gm}-\omega_L-i\Gamma_m}, \tag{2.29}$$

where $\omega_{gm}$ is the transition frequency from electronic state $|m\rangle$ to ground state $|g\rangle$, $\omega_L$ is the the laser frequency and $\Gamma_m$ is the spontaneous decay rate of state $|m\rangle$. For non-resonance Raman scattering, the factor is governed by a large detuning between $\omega_{gm}$ and $\omega_L$, typically tens of terahertz (THz); but in the case of RRS, denominator of this factor reduces to the order to $\Gamma_m$, on the order of megahertz (MHz), which give an enhancement factor of $\sim 10^6$.

The signal enhancement in surface-enhanced Raman scattering (SERS) is much more complicate, as discussed in reference [5]. The list of factors need to be considered are: surface plasmons, excitation wavelength, the polarization of the exciting and scattered radiation, structural features of the SERS-active system, number density of molecules on the surface and so on. In experiments, estimation of enhancement factor (EF) can be obtained relatively easier by the equation [30, 31]

$$EF = \frac{[I_{SERS}][N_{bulk}]}{[I_{bulk}][N_{ads}]}, \tag{2.30}$$

where the intensity ratio between SERS ($I_{SERS}$) and bulk ($I_{bulk}$) signal can be directly measured and number of molecules ($N_{bulk}$ for the bulk signal, $N_{ads}$ for adsorbed molecules on surface of SERS material) involved in the process can be estimated from density and occupation volume of the molecule studied.

### 2.4 Superradiant, subradiant states and yoked superfluorescence system

In 1954, Dicke predicted the possibility of "super-radiant" spontaneous emission from a system of radiators with dipole transitions, either electric or magnetic [14]. Ever since, many important works have been done both theoretically and experimentally [*]. In extended system, "timing is everything" [32]. By attaching a proper phase factor, governed by the propagation of radiation (thus timing), for each excited atom, the generalized result is the timed Dicke state

$$|\Psi\left(N|1_{\mathbf{k_0}}\right)\rangle = \frac{1}{\sqrt{N}} \sum_j e^{i\mathbf{k}_0\cdot\mathbf{r}_j} |b_1, b_2, \ldots, a_j, \ldots, b_N\rangle|0\rangle, \tag{2.31}$$

---

[*] For more references, please refer to introduction of Chapter 6

where one atom is excited by a photon of wave vector $\mathbf{k}_0$, $\mathbf{r}_j$ is the position of the $j$th atom; we assume two-level system, $|a\rangle$ is the excited state and $|b\rangle$ is the ground state of the atoms. And as shown in the reference [32], the emission from this state is directional, and it is a superradiant state.

The superradiant state is only a set of particular states in the Hilbert space which describes $N$ spinors (a two level atom can be treated as a pseudospin). In general, there are $2^N$ independent states. From group theory, as Dicke taught us, only $N+1$ states belongs to superradiant group which can be excited by directly absorbs photons from the ground state. It can be shown that in the superradiant group, the decay rate from state $|N, m\rangle$ to $|N, m-1\rangle$ is $(N+m)(N-m+1)$ times of single atom decay rate [33]. All other states can be grouped as subradiant states in the sense that these states do not decay to superradiant states (thus not accessible by direct absorption of photons), and for some of these states, their decay to ground state is much slower. Reference [33] shows examples of the subradiant states.

We can generalize the timed Dicke state to weak excitation limit when $m$ atoms are excited while $m \ll N$ holds. The state can be written as

$$|\Psi\left(N|m_{\mathbf{k_0}}\right)\rangle = C \sum_{j_1,\cdots,j_m} e^{i\mathbf{k}_0\cdot\left(\mathbf{r}_{j_1}+\cdots+\mathbf{r}_{j_m}\right)} |b_1, b_2, \cdots, a_{j_1}, \cdots, a_{j_m}, \cdots, b_N\rangle|0\rangle, \quad (2.32)$$

where $C$ is a normalization factor.

Most of the experiments we present in last a few chapters are working on so-called Yoked superfluorescence (YSF) system [21], which can be simplified to a three-level system, as shown in Figure 2.1, $|a\rangle$ is the excited state, $|b\rangle$ is the intermediate state and $|c\rangle$ is the ground state of the atoms. To get an idea of the emission from the system, we will proceed the following simple argument. The full problem can be treated by the Maxwell-Bloch equations, as shown in reference [34], for example.

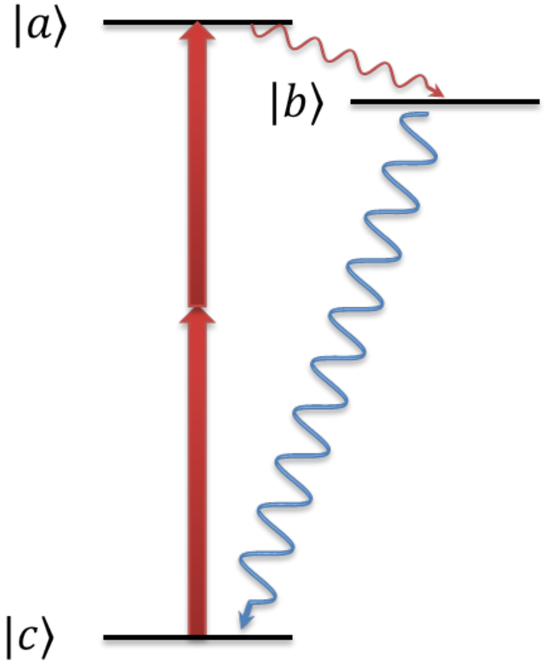

Figure 2.1: Scheme of a three-level Yoked superfluorescence (YSF) system.

Using the language of timed Dicke state, we start from state

$$|c_1, \cdots, c_N\rangle \otimes |m\rangle_{\mathbf{k}_0}, \tag{2.33}$$

Let's assume that the photons from excitation beam have wave vector $\mathbf{k}_0$, after the excitation, the state is

$$C \sum_{j_1,\cdots,j_m} e^{i\mathbf{k}_{ac}\cdot\left(\mathbf{r}_{j_1}+\cdots+\mathbf{r}_{j_m}\right)} |c_1, c_2, \cdots, a_{j_1}, \cdots, a_{j_m}, \cdots, c_N\rangle|0\rangle, \tag{2.34}$$

where $\mathbf{k}_{ac} = 2\mathbf{k}_0$, $C$ is normalization factor. If the system coherently emits photons,

i. e., superradiant emission, and the atoms go to state $|b\rangle$,

$$C \sum_{j_1,\cdots,j_m} e^{i(\mathbf{k}_{ac} \pm \mathbf{k}_{ab})\cdot\left(\mathbf{r}_{j_1}+\cdots+\mathbf{r}_{j_m}\right)} |c_1, c_2, \cdots, b_{j_1}, \cdots, b_{j_m}, \cdots, c_N\rangle |m\rangle_{\mathbf{k}_{ab}}. \tag{2.35}$$

The sign before $\mathbf{k}_{ab}$ depends on the direction of the emission: if the emission goes in the same direction (forward emission) of $\mathbf{k}_0$, the sign is minus; and if the emission goes to opposite direction (backward emission) of $\mathbf{k}_0$, it is plus sign. In the case of forward emission, $|\mathbf{k}_{ac} - \mathbf{k}_{ab}| = |\mathbf{k}_{bc}| = \omega_{bc}/c$, so the state can further emit photons in the same direction of $\mathbf{k}_0$, of an angular frequency $\omega_{bc}$. But in the case of backward emission, the $\mathbf{k}$ vectors are not phase-matching, thus could not emit in superradiant way; in general, the corresponding state is not a eigenstate of the system, thus a superposition of superradiant and subradiant states.

For the YSF system, the coherence $\rho_{ab}$ and $\rho_{bc}$ are coupled, so does the forward emissions. The superfluorescence emission on the upper transition ($|a\rangle \rightarrow |b\rangle$) induces simultaneous superrandiant emission on the lower transition ($|b\rangle \rightarrow |c\rangle$), but the increase of emission on the lower transition will deplete state $|b\rangle$ and reduce $\rho_{ab}$, thus suppress the emission on the upper transition, this is the reason it's named "yoked". But for backward emission, lack of lower transition in fact helps faster build-up of the emission on the upper transition than the forward emission.

# 3. ULTRALOW-POWER LOCAL LASER CONTROL OF THE DIMER DENSITY IN ALKALI-METAL VAPORS THROUGH PHOTODESORPTION[*]

## 3.1 Introduction

Alkali-metal vapor systems are in high demand as time and frequency standards [35], playing an important role in optical metrology [36], and are widely used to test fundamental principles in optical and atomic physics [3]. Besides wide range of applications, the alkali-metal vapor is one of the most attractive and powerful model systems for laser-matter interaction, which has enabled some of the most significant discoveries in natural sciences from pioneering experimental demonstrations of radiation pressure on atoms [37], optical pumping [38, 39], and hyperfine structure measurements [40] to coherent population trapping [41], magneto-optical trapping [42], and Bose-Einstein condensation [43].

A routine technique for the preparation of alkali-metal vapors for a broad variety of laboratory experiments and applications is based on heated alkali-vapor cells. Alkali vapors in such cells include atomic and molecular components whose overall pressure is controlled by the temperature of the cell [44]. Several elegant techniques have been proposed to control the densities of the atomic and molecular fractions in alkali-metal vapors. In particular, Lintz and Bouchiat [45] have demonstrated the laser induced destruction of cesium dimers in a cesium vapor through a quasiresonant process assisted by collisions of cesium molecules with excited-state cesium atoms and

---

[*] Reprinted with permission from "Ultralow-power local laser control of the dimer density in alkali-metal vapors through photodesorption," by Pankaj K. Jha, Konstantin E. Dorfman, Zhenhuan Yi, Luqi Yuan, Vladimir A. Sautenkov, Yuri V. Rostovtsev, George R. Welch, Aleksei M. Zheltikov, and Marlan O. Scully, 2012, Applied Physics Letters 101 (9), 091107. Copyright [2012] by the American Institute of Physics.

later on Ban et al [46]. extended this approach to rubidium. Sarkisyan et al. [47] also developed a simple method of thermal dissociation of cesium dimers in cesium vapor cells.

In the past decade, laser induced atomic desorption (LIAD) [22, 23, 24, 25] technique has gained much attention for controlling the atomic density in cells coated with paraffin etc. In such cells, the atoms get adsorbed on their inner surface with time. In a typical LIAD experiment, a desorption laser illuminates a coated vapor cell and its effect is studied by the analyzing the absorption/transmission of a weak probe field resonant to some atomic/molecular transition of the alkali vapor. Work related to this area has been primarily focused on controlling the atomic densities for e.g., Rb, Cs, K, Na, etc. First initiative in the direction of control over dimer concentration using LIAD was studied by the Berkeley group [25].

In this chapter, we extend the laser-induced photodesorption technique to ultralow laser power and use resonant Raman spectroscopy to demonstrate that LIAD (Refs. [48] and [49]) enables an accurate local control of the dimer density in alkali-metal vapors. Our experimental strategy is based on studying the backscattered Raman signal from the alkali-metal vapor while illuminating a thin film of metal, deposited on the window of an uncoated vapor cell, using continuous wave (cw) laser at milli-watt power [see inset Figure 3.1]. In our experiment, we used a cylindrical uncoated Pyrex cell with a diameter of 3 cm and a length of 7.5 cm. After desorption from the film, the alkali monomers (atoms) can form dimers, trimers, and higher order oligomers by colliding with each other. Possibility of dimers adsorption on the surface of the film is beyond the scope of the current work.

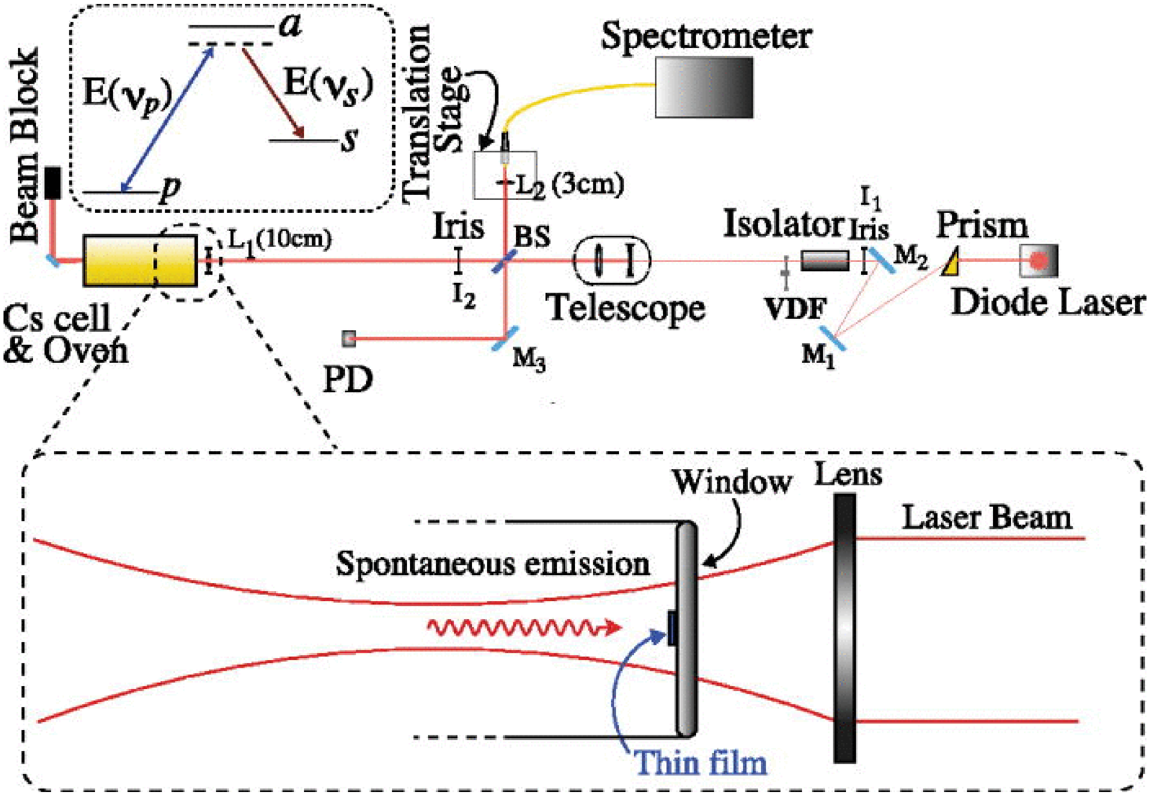

Figure 3.1: Experimental setup. The upper inset shows a simple three-level model for Raman scattering. Here, the lower two levels $p$ and $s$ and upper level a are the vibrational states the ground state $X^1\Sigma_g^+$ and the excited state $B^1\Pi_u$ of cesium dimer, respectively. The lower inset shows the zoomed part near the window. A thin film of metallic cesium is condensed on one side of the cell inside the oven. The Raman signal generated in the backward direction is collected and analyzed using the spectrometer. VDF is variable density filter; L is lens and BS is beam splitter.

## 3.2 Experiment

Our experimental setup is shown in Figure 3.1. A tunable free-running single-mode diode laser [Sanyo DL7140-201] was used for spectroscopy of cesium dimers. While the laser wavelength of the diode laser can be set coarsely by adjusting the temperature (+0.04 nm/K), fine frequency tuning was performed by varying the injection current (-0.04 $\text{cm}^{-1}$/mA). The input laser beam was collimated by an aspheric lens, and a prism was used to compress the beam size along the horizontal axis to make it circular. Unfocussed and collimated beam diameter was $\sim$ 3 mm. The telescope system was further introduced to expand the beam diameter by a factor of 2 and a variable density filter (VDF) controlled the intensity of the beam. The collimated laser beam was focused into the cell using a lens L1 [focal length $f = 10$ cm] into the cell. A circular thin film of cesium was deposited on the inner surface of the cell window at a distance of $\sim$ 3 cm from the lens. The backscattered Raman signal was collected into a multimode fiber, which conducts the light into a diffraction spectrometer [Ocean Optics HR2000: spectral resolution 0.065 nm]. Irises were used to collimate the beams and block diffused scattered radiation due to reflections from the cell windows and other optics.

The laser wavelength was set resonant to the electronic transition $X^1\Sigma_g^+ \leftrightarrow B^1\Pi_u$ of the cesium dimer. The absorption band of the transition $X^1\Sigma_g^+ \leftrightarrow B^1\Pi_u$ ranges from 755 nm to 810 nm [50]. In Figure 3.2(a), we have shown one such spectrum collected in the backward direction. We tuned the pump laser wavelength to the resonance [†] by observing the intensity of one of the Raman peaks (796.16 nm). The maximum value of the intensity corresponds to pump wavelength $\lambda_p = 779.9010$ nm (air) [WA-1500 wave meter from Burleigh]. In Figure 3.3, we have plotted the

---

[†] The width of the response of Raman signal against the single photon detuning will be governed by Doppler broadening.

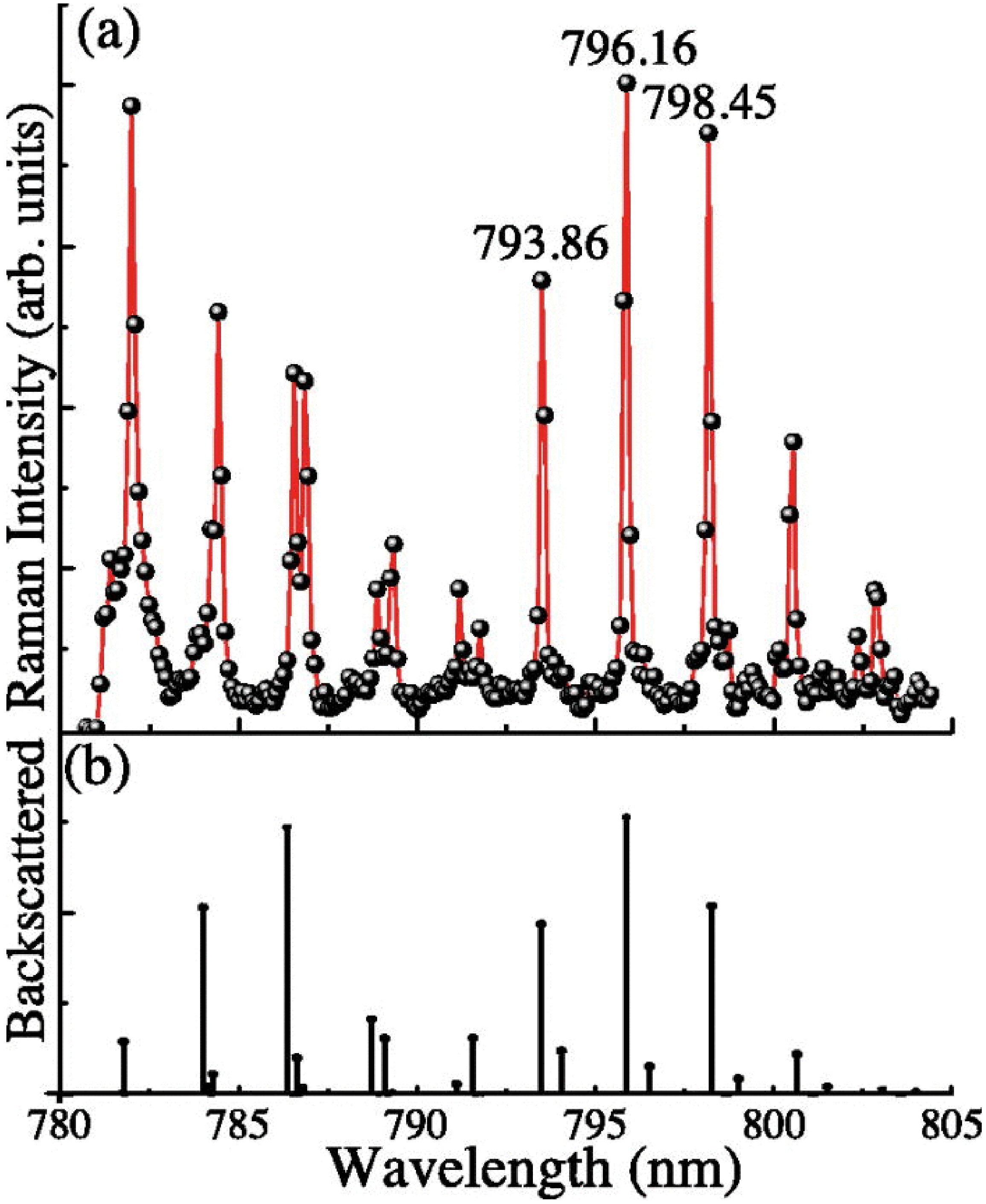

Figure 3.2: Raman spectra in the backward direction (arb. units) (a) experimental and (b) numerical simulation.

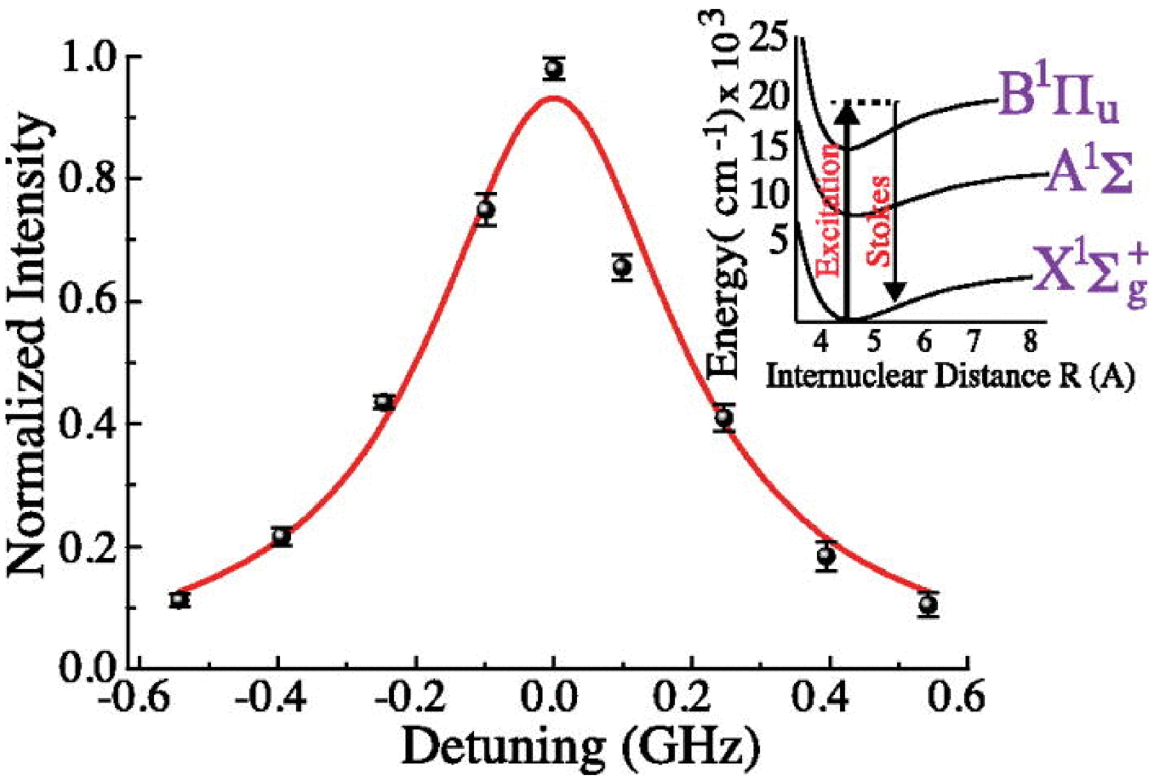

Figure 3.3: Resonance enhancement of the Raman peak at 796.16 nm as a function of the one-photon detuning. Full width at half maximum value (∼0.3 GHz) is consistent with the Doppler broadening from the vapor phase. Insert shows the energy levels of Cesium dimer relevant to our experiment.

resonance enhancement of the peak (796.16 nm) against the one photon detuning $\Delta = \omega_{ap} - \nu_p$, which indicates the high sensitivity of the Raman response to the pump wavelength. To simulate the spontaneous Raman spectral response, we used [51]

$$S_{Raman}(\nu_p, \nu_s) = 2\pi \sum_{p,s} P(p) |\chi_{sp}(\nu_p)|^2 \delta(\omega_{sp} + \nu_s - \nu_p), \tag{3.1}$$

where

$$\chi_{sp}(\nu_p) = \sum_a \frac{\wp_{sa}\wp_{ap}}{-\omega_{ap} + \nu_p + i\Gamma}. \tag{3.2}$$

Here, $\nu_p$ and $\nu_s$ are the pump and the Stokes frequency, respectively. $P(p)$ is the normalized thermal population distribution given as $P(p) = e^{-E_p/kT} / \sum_p e^{-E_p/kT}$. $\hbar\omega_{ij}$ and $\wp_{ij}$ are the energy difference and the transition dipole moment between the levels $i$ and $j$, respectively. We have approximately calculated the Franck-Condon factors (FCF) by using the exact eigenfunctions of the Morse potential [52]. $\Gamma$ is the transverse relaxation rate. $E_\nu = \hbar\omega(\nu + \frac{1}{2}) - \hbar\omega x(\nu + \frac{1}{2})^2$ is the energy of vibrational level $\nu$, where $\omega$ is the vibrational frequency and $\omega x$ is the vibrational anharmonicity [53]. For cesium dimer [27] ground state, $X^1\Sigma_g^+$, $\omega_g \sim 42.20\,\mathrm{cm}^{-1}$ and $\omega_g x_g \sim 0.0819\,\mathrm{cm}^{-1}$ while in the excited state, $B^1\Pi_u$, $\omega_e \sim 34.33\,\mathrm{cm}^{-1}$ and $\omega_e x_e \sim 0.08\,\mathrm{cm}^{-1}$. Different amplitudes of the FCFs for different transitions between the vibrational levels of the electronic states $X^1\Sigma_g^+$ and $B^1\Pi_u$ indicate that the dipole moment for different transition has different magnitude [54], since the square of the dipole moment is proportional to the FCFs. Consequently, the gains for different transitions are different. Figure 3.2(b) shows the simulated spectrum in the Stokes region using Eqn. (3.1), which is an excellent agreement with the experimental data shown in Figure 3.2(a).

The main result of our work is shown in Figure 3.4 where we have plotted the

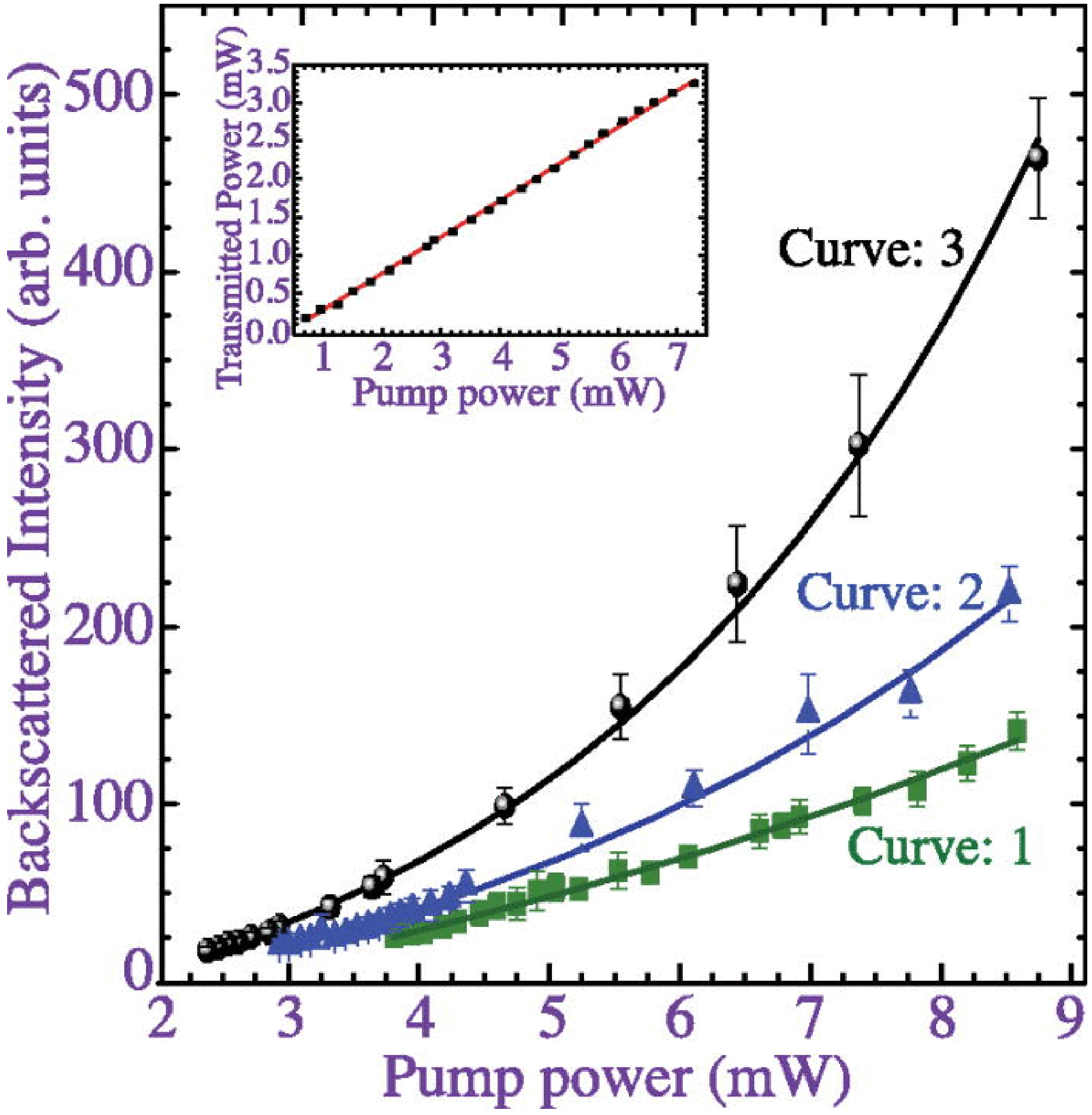

Figure 3.4: Plot of the backscattered intensity (arb. units) of the Raman peak at 796.16 nm vs the pump power for three different choices of the cell temperature in the presence of the film. Dots illustrate the experimental data and solid lines are fitting using Eqn. (3.3). The inset shows the transmission of pump laser through the metal film.

intensity of Raman peak (796.16 nm) as a function of the pump power for different cell temperatures. Here, curves 1, 2, and 3 correspond to the cell temperature $T_c$ = 513 K, 526 K, and 543 K, respectively. In our experiment, we also monitored the transmission through the metal film before and after the measurements of laser induced fluorescence (LIF) from cesium vapor. The linear dependence between transmitted power and input power shown in Figure 3.4 (inset) indicates that under our experimental conditions, the transmission through the film is independent of the pump power. As the fluorescence signal depends on the input power which indicates that the laser light induces desorption of cesium atoms from the metal film. Power independence of the film transmission can be explained by moderate reduction of the film, of the order of several monolayers. The efficiency of the desorption increases with the cell temperature.

To fit our experimental data, we assumed the following fitting function:

$$I = \sum_{n=1} \alpha_n P^n, \tag{3.3}$$

the coefficients $\alpha_n (n = 1, 2, 3 \ldots)$ contains the information about the number density of the dimers, differential cross section, geometry of the gain medium, contribution due to photodesoprtion, etc. In the absence of the film $\alpha_n = 0$ for $n \geq 2$. We further normalize Eqn. (3.3) with respect to the linear contribution ($I_1 = \alpha_1 P$), which yields

$$\frac{I}{I_1} = 1 + \beta_1 P + \beta_2 P^2 + \ldots, \tag{3.4}$$

where $\beta_n = \alpha_{n+1}/\alpha_1$. Next, we simplify our analysis by considering $n = 1$ term only. To account for the background noise, we added $I_0$ in Eqn. (3.3). Generally, the intensity of the Stokes radiation from a volume of the medium of unit area and a length $dz$ is given by [55]

$$dI = N_0(T_c)\frac{d\sigma}{d\Omega}\zeta P dz, \tag{3.5}$$

where $N_0(T_c)$ is the density of the scattering molecules, $d\sigma/d\Omega$ is the differential cross section of the spontaneous Raman scattering, $\zeta$ is the solid angle in which the scattering is observed, and $P$ is the power of the laser radiation. In Table 3.1, we present the fitting parameter $\beta_1 = \alpha_2/\alpha_1$ and estimated the number density of the cesium dimers. The numbers in the parentheses corresponds to the error in the fitting parameters. Here, $T_c$ is the cell temperature and $N_1$ is the number density of the dimers when the pump power is $P \sim 8.5$ mW. In order to estimate for $N_1$, we use

$$N = N_0(1 + \beta_1 P). \tag{3.6}$$

From the estimated values at $T_c = 543$K and $P$ ~8.5 mW, the number density of the cesium dimers is ~7 times larger than in the absence of atomic desorption from the film. We also observed enhancement in dimer density even at lower cell temperature $T_c = 513$ K. Let us introduce an effective temperature $T_e$, which is equivalent to the cell temperature at which the number density of cesium dimers is $N_e = N_1$. Using the vapor pressure formula [44], we estimated for $T_e$ and the results are shown in Table 3.1. We see that the effective temperature can be as high as ~ 54 K above the cell temperature.

For all the estimates, we have assumed that the spontaneous Raman is the dominant phenomena here. To support the assumption that the nonlinear behavior of the Raman signal is not due to stimulated Raman scattering (SRS), we estimate the gain coefficient for SRS under our experimental conditions. For SRS, the Stokes intensity

| Curve | T$_c$(K) | $\beta_1$ | $N_1/N_0$ | T$_e$(K) |
|---|---|---|---|---|
| 1 | 513 | 0.1734 (0.009) | 2.474 (0.108) | 567 |
| 2 | 526 | 0.2972 (0.016) | 3.526 (0.421) | 578 |
| 3 | 543 | 0.6704 (0.025) | 6.698 (0.267) | 597 |

Table 3.1: Numerical values of the fitting parameter $\beta_1 = \alpha_2/\alpha_1$, the number density of the cesium dimers at maximum pump power $P \sim 8.5$ mW, and the effective cell temperature $T_e$.

in the backward direction, assuming that pump intensity is not depleted, is given by [55]

$$\frac{d}{dz} I_s^b(z) = -g I_s^b(z) I_p, \tag{3.7}$$

with the gain coefficient [55]

$$g = \left( \frac{N|\wp_{ap}|^2|\wp_{as}|^2 \nu_s n_{ps}^0}{2\epsilon_0^2 c^2 \hbar^3 \Delta^2 \Gamma_{ph}} \right). \tag{3.8}$$

Here, $n_{ps}^0 = \varrho_{pp}^{(0)} - \varrho_{ss}^{(0)}$ is the population inversion and $\Gamma_{ph}$ is the decay rate of the Raman coherence. In the temperature range from 470 K - 540 K, the atomic number density $N_a$ and the molecular number density $N_m$ lies in the range $10^{15} - 10^{16}\,\mathrm{cm}^{-3}$ and $10^{13} - 10^{14}\,\mathrm{cm}^{-3}$, respectively. The ratio [44] of $N_a$ to $N_m$ is order of $10^2$. In the experiment, we optically pumped the cesium dimers, the cell temperature $T_c \sim$ 545 K, and molecular density $2 \times 10^{14}\,\mathrm{cm}^{-3}$ , with a cw milli-watt laser tuned to the wavelength $\lambda_p = 779.90$ nm. The diameter of the focused beam at the waist is $d = 4\lambda_p f/\pi D \sim 34$ $\mu$m, where the unfocused beam diameter $D$ and the focal length of the lens $f$ are 0.6 cm and 10 cm, respectively. The depth of the focus is $L = 8\lambda_p f^2/\pi D^2 \sim 0.11$ cm. The pump intensity at the waist is $I_p \sim 300\,\mathrm{W/cm}^2$. The differential spontaneous cross section was estimated as $d\sigma/d\Omega \sim 3 \times 10^{21}\,\mathrm{cm}^{-2}$. For the resonance enhanced Raman, the Doppler broadening $\Delta_D = k_p \nu_{th} \sim 2 \times 10^9\,\mathrm{s}^{-1}$

and we assumed the decay rate of Raman coherence $\Gamma_{ph} \sim 1$ GHz. From Eqn. (3.7) and the experimental parameters, we obtained $g \sim 1.2 \times 10^{-2}\,\mathrm{W}^{-1}\mathrm{cm}^{-1}$. Hence the estimate for $gI_pL \sim 0.4$ clearly indicates that the contribution from SRS can be safely neglected.

## 3.3 Conclusion

In this chapter, we used ultralow-power cw diode laser to optically control the density of cesium dimers through photodesorption from a thin film of cesium in an uncoated Pyrex cell. To probe the dimer concentration, we collect the spontaneous Raman signal in the backward direction, which serves the two-fold purpose: (a) the signal is from the dimers and (b) to demonstrate the idea of remote detection of chemicals using ultralow-power cw lasers. We observed a nonlinear behavior in the peak intensity against the pump power contrary to the linear dependence behavior well known from the spontaneous Raman theory. The deviation from the linear behavior is due to the contribution from the cesium dimers produced through photodesorption from the thin film on the window. Under the experimental conditions, we estimated that the number density of the dimers increased substantially in the presence of the film.

The main goal of this work is to make a significant step in the direction of LIAD technique, which offers a powerful control over atomic/dimer density in coated cells. An optical control over the vapor density, as shown here, will offer an additional tool for numerous applications of the alkali-metal vapors, e.g., time and frequency standards [35], optical metrology [36], testing fundamental principles in optical and atomic physics [3], as well as to be the most attractive and powerful model systems of laser-matter interaction.

# 4. SURFACE-ENHANCED RAMAN SCATTERING ON TEMPLATE-EMBEDDED GOLD NANOROD SUBSTRATES*

## 4.1 Introduction

Surface-enhanced Raman scattering (SERS) is a powerful tool for obtaining molecular chemical information [5, 6]. Electromagnetic and chemical enhancement mechanisms are responsible for a large signal enhancement [56, 57, 58, 59]. Many different nanostructures have been fabricated to study the SERS effect, including rough metallic surfaces via chemical etching [60], aggregates of nanoparticles [61], Ag and Au nanorods and nanowires fabricated by chemical and electrochemical methods [62, 63], and nanoparticle arrays prepared by nanosphere lithography [64] or electron-beam lithography [65], among others. However, reproducibility of the largest enhancement factors remains challenging.

Anodic aluminum oxide (AAO) templates have been widely employed to fabricate various array structures for SERS applications and have shown good reproducibility. Recently, Wang et al. used silver nanoparticle arrays as SERS substrates with tunable interparticle gaps in the sub-10 nm regime by regulating the wall thickness of porous AAO nanochannels [66]. Genov et al. reported a relationship between the particle size and the interparticle spacing that affected the SERS enhancement based on the theoretical studies of two-dimensional (2D) arrays of metal nanoparticles [67]. These studies have shown that geometric parameters determine the enhancement of local electromagnetic fields. However, many SERS experiments were performed using the same excitation wavelength for substrates with different geometric parameters due

---

*Reprinted with permission from "Surface-Enhanced Raman scattering on template-embedded gold nanorod substrates" by Ziyun Di, Isabel Schultz, Zhenhuan Yi, Kai Wang, Dmitri V. Voronine, Wenhao Wu and Alexei V. Sokolov, 2014. Journal of Modern Optics, vol. 61, pp. 72-76, Copyright [2014] by Taylor & Francis.

to the lack of a broadly tunable laser excitation source. Additionally, it was shown that the excitation wavelength plays an important role in the SERS enhancement [58, 68]. Here we emphasize that the maximum SERS intensity is achieved when the localized surface plasmon resonance (LSPR) strongly enhances both the incident and the scattered intensities, assuming that the electromagnetic (EM) mechanism mostly contributes to the observed SERS enhancement.

In this chapter, SERS was investigated of rhodamine 6G (R6G) molecules on template-embedded Au nanorods with diameters up to 200 nm and with a gap size between the adjacent nanorods of 100 nm. The SERS enhancement factor obtained was about $10^6$. Such substrates have received little attention previously. We discuss the origin of SERS with different geometric substrate parameters and use a simplified model to explain the results.

## 4.2 Experimental methods

The Au nanorods were fabricated by electrochemical deposition into the pores of AAO membranes (Whatman Inc.) with a typical pore diameter of 200 nm and interpore distance of 300 nm, as shown in Figure 4.1(a). Before the electrochemical deposition, a layer of Au film with thickness of 100 nm was coated on the back of the membrane, serving as a back electrode. Commercial gold electrolyte solution (Auruna 5000) was used for electrodeposition. In order to acquire a high filling rate, a low plating current density with a typical value of $2.2 - 2.5\,\mathrm{mA/cm^2}$ was adopted. After the pores of the AAO membranes were filled, the back Au layer electrode was mechanically polished using $Al_2O_3$ powders with size of 300 nm. The sample was subsequently carefully cleaned using acetone, isoproponal, and deionized water. Figure 4.1(b) shows the top view of Au nanorods embedded in the AAO membrane.

The surface morphology of the AAO templates was measured using a scan-

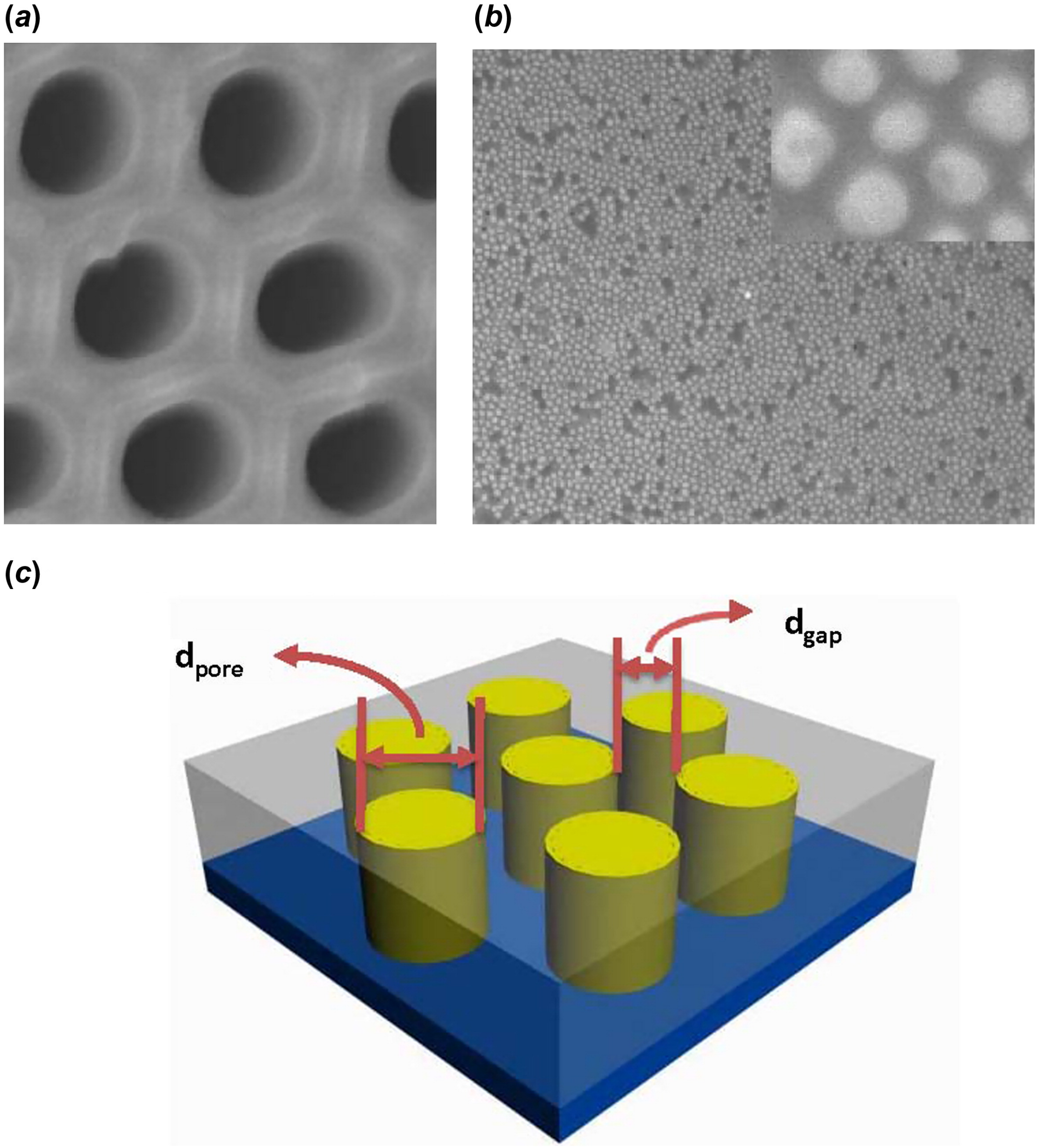

Figure 4.1: SEM morphologies of (a) bare AAO template and (b) AAO template-embedded Au nanorods (the inset is a magnification). (c) Schematic illustration of AAO-template-embedded Au nanorods. $d_{pore} = 200$ nm is the diameter of Au nanorods and $d_{gap} = 100$ nm is the gap distance between adjacent nanorods.

ning electron microscope (SEM). SEM images of the AAO template and the AAO template-embedded Au nanorods are shown in Figures 4.1 (a) and (b), respectively, indicating that the nanopores are quite uniform. Figure 4.1(c) shows a schematic illustration of the AAO-template-embedded Au nanorods, where $d_{pore} = 200$ nm is the diameter of Au nanorods and $d_{gap} = 100$ nm is the gap size between the adjacent nanorods. Rhodamine 6G (R6G) was used as the analyte to test the SERS effect of this substrate. The SERS substrates were immersed into the R6G solution for 30 min and then washed to remove the excess amount of R6G followed by drying in air, thus forming a monolayer. R6G on bare AAO templates was used as a reference. The SERS spectra of R6G were recorded using a confocal Raman microscope with an electric-cooled CCD detector and 180° backscattering detection. The excitation source was a 532 nm cw laser with 3 mW power at the sample. The exposure time for all of the spectra was 10 s. All the measurements were carried out at room temperature.

## 4.3 Results and discussion

Figure 4.2 shows the Raman spectra of R6G absorbed on the bare AAO template (red) and on the AAO-template-embedded Au nanorods (black). Background was subtracted from the spectra. There is a rather weak Raman signal of R6G on the bare AAO template. However, R6G absorbed on the AAO-template-embedded Au nanorods shows a remarkable Raman signal enhancement. Compared to the bare AAO template, R6G adsorbed on the AAO-template-embedded Au nanorod substrate exhibits ~30-fold enhancement in Raman intensity. The enhancement factor (EF) was estimated using Eqn. 2.30: EF $= [I_{SERS}][N_{bulk}]/[I_{bulk}][N_{ads}]$ [30, 31], where $I_{SERS}$ and $I_{bulk}$ are the Raman intensities at a selected vibrational mode in SERS and in spontaneous bulk Raman spectra, respectively. $N_{ads}$ and $N_{bulk}$ are the ad-

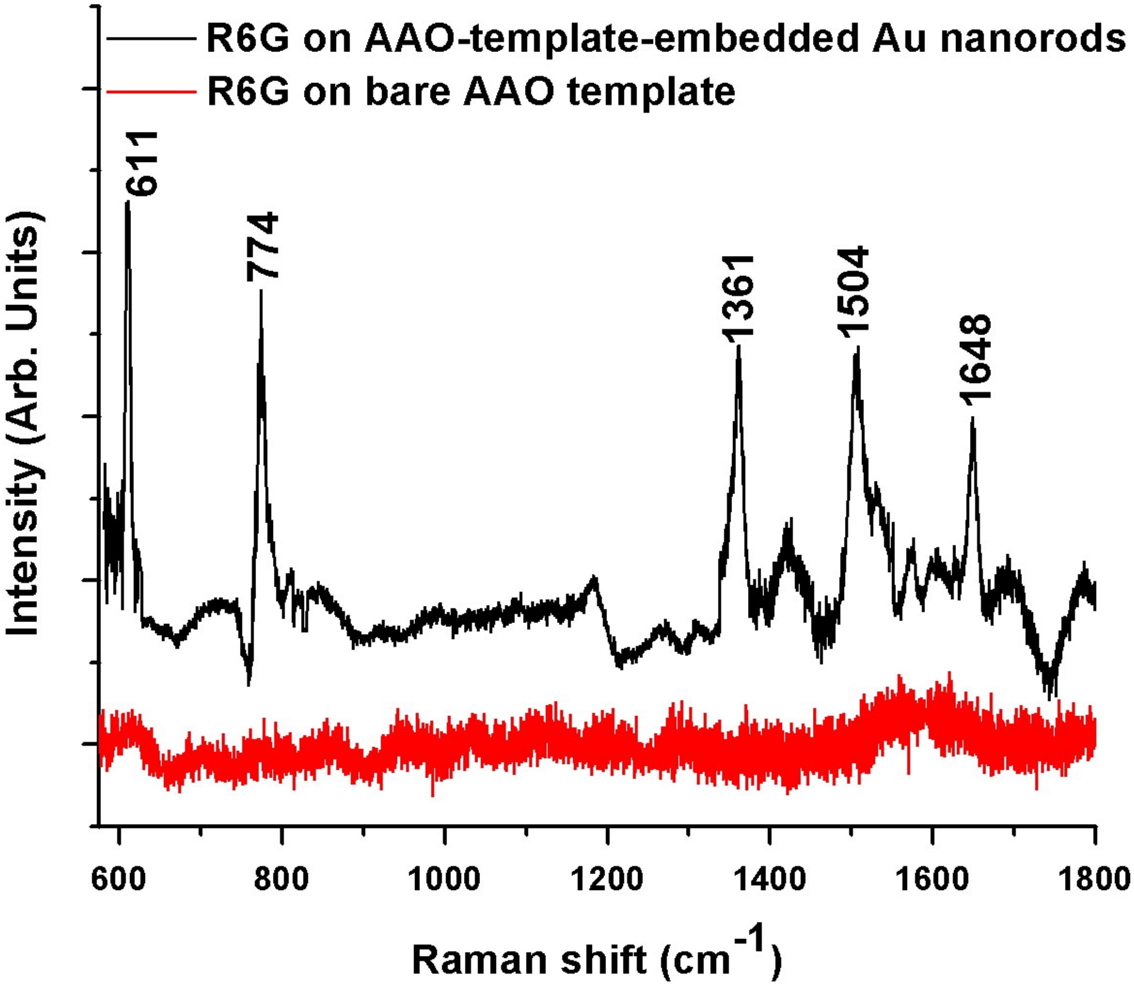

Figure 4.2: Raman spectra of R6G adsorbed on bare AAO template (red) and AAO-template-embedded Au nanorods (black). The spectra are vertically shifted for convenience.

sorbed and bulk numbers of molecules exposed to the optical excitation, respectively; $N_{ads}$ can be obtained according to $[N_{ads}] = N_d A_{laser} A_N/\sigma$, where $N_d$ is the number density of the nanorods, $A_{laser}$ is the area of the laser beam cross section, $A_N$ is the nanorod footprint area, and $\sigma$ is the surface area occupied by an adsorbed molecule ($\sigma = 4\,\mathrm{nm}^2$ for R6G [69]). Using this method, an SERS enhancement factor as large as $\sim 10^6$ was obtained with the diameter of laser focal point $\sim 2\ \mu$m SERS substrates with large Au nanorod diameters have previously received little attention. Here, we investigate the relationship between the geometry of the SERS substrates and the SERS performance.

It is known that the AAO template-embedded Au nanorod arrays are good candidates for investigating the geometric effects of metallic nanostructures by changing the pore diameter and the pore distance of the AAO template and then examining the SERS signals. Many works [58, 61, 66] have been performed to demonstrate how the EM enhancement depends on the geometry of the system. It is necessary to achieve maximum EM enhancement of both the incident field and the Raman scattering. Consequently, one should either prepare the sample to make the LSPR in the proper location for a fixed laser frequency or set the wavelength to a higher frequency than the LSPR in a tunable laser system. According to the previous research by McFarland et al. [70], the magnitude of the energy separation between the excitation profile maximum and the LSPR extinction maximum is roughly half of the vibrational energy. With this motivation, we numerically investigated the plasmon resonances of a simplified model of 2D arrays consisting of 21 Au nanospheres with varying diameter and gap size.

We assumed that the molecules are adsorbed on the top of the Au nanospheres, according to the discussion in [71]. The nanospheres were homogeneously distributed. Our numerical results are based on the model described in [72, 73]. Figure 4.3 shows

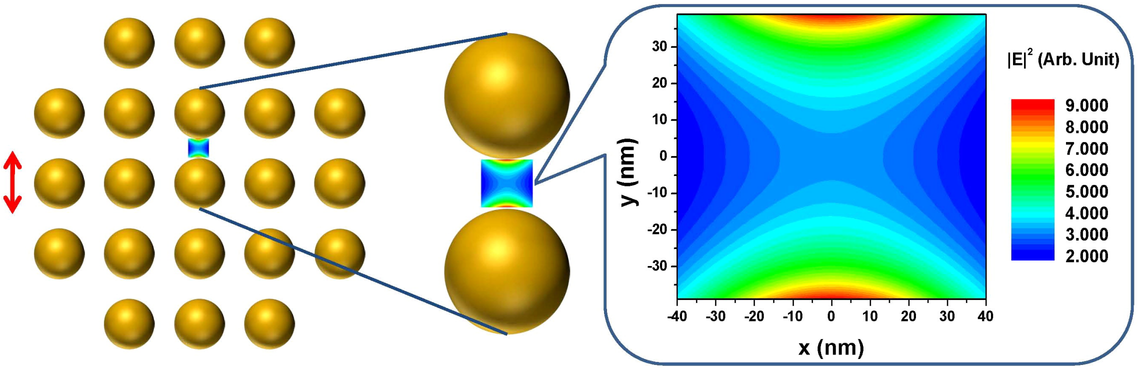

Figure 4.3: Electric field intensity distribution between adjacent Au spheres with 200 nm diameter and 80 nm gap size. The excitation wavelength is 532 nm. Arrow indicates the polarization of incident electric field.

the electromagnetic field intensity distribution in the area between the adjacent gold nanospheres with a diameter $d = 200$ nm and a gap size between the adjacent spheres $d_{gap} = 80$ nm. The field intensity reaches a maximum near the surface of the spheres. The excitation wavelength is 532 nm and the electric field is incident normal to the inter-sphere axis. We also performed simulations using randomly displaced (inhomogeneously distributed) nanospheres with an average displacement of $\sim 5$ nm. The results were similar to the ordered array in Figure 4.3.

Next we investigated the dependence of the plasmon resonance on the geometry of the SERS substrate. Figure 4.4(a) shows the scattering cross section (SCS) for illumination normal to the sample plane with the electric field polarization parallel to the axis joining the nanosphere centers (same as in Figure 4.3). The simulations were carried out for the same gap size $d_{gap} = 10$ nm but with different nanosphere diameters $d$. Figure 4.4(a) shows the plasmon resonance position as a function of $d$. When the diameter increases from 20 nm to 100 nm, a typical red shift of the resonance is observed. Note that the resonance lies in the vicinity of the laser wavelength. However, in the practical SERS substrate fabrication, the gap distance varies with the change of the diameter of the nanorods due to the constraints of the AAO template-assisted fabrication method. Increase of the nanorod diameter is usually accompanied by the increase of the gap distance.

Finally we consider the geometry of the nanosphere arrays matching the experimental parameters. Figure 4.4(b) shows the SCS for different substrate parameters. A similar red-shift behavior of the resonance wavelength is also observed for increasing the sphere diameter while keeping the ratio $d/d_{gap}$ the same. This observation agrees well with the reflectance spectra of the samples in [71] in which the broadband extinction features were related to the LSPR. It is well known that both LSPR and the Raman excitation wavelength play an important role for the SERS performance. Our results indicate that the excitation wavelength dependence of the SERS performance is more complicated in the visible regime [67] than in the longer wavelength excitation regime which is consistent with the experimental observation of reference [74] in which the geometry dependence of SERS performance is more pronounced for 785 nm than for 514.5 nm excitation. These design principles may be helpful as a guiding tool for the SERS substrate optimization and for other surface-enhanced nonlinear optical spectroscopies such as time-resolved coherent Raman scattering [75].

## 4.4 Conclusion

In summary, a simple method of AAO template-assisted nanofabrication was used to fabricate 2D arrays of gold nanorods as SERS substrates. SERS spectra of R6G were measured and $\sim 10^6$ enhancement factors were obtained. The origin of the SERS signal enhancement was investigated by numerical simulations of 2D arrays of Au nanospheres with different diameters and gap size. The simplified model is able to explain the major features of the experiments. This approach may be further

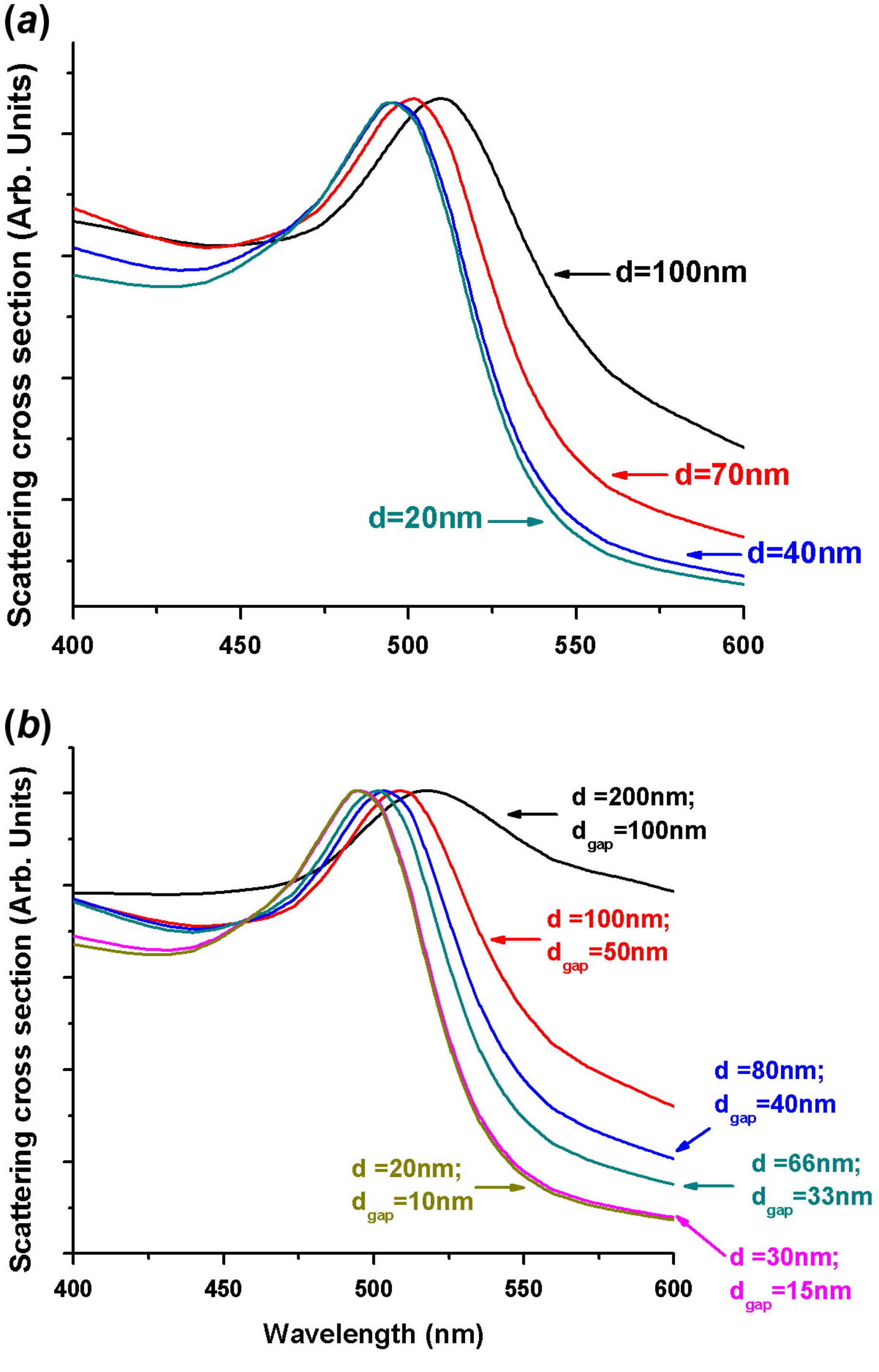

Figure 4.4: Scattering cross sections for Au nanosphere arrays with (a) different diameters $d$ and the same gap size $d_{gap} = 10$ nm, and (b) different diameters $d$ and gap size $d_{gap}$ while keeping the ratio of these two parameters the same.

extended to optimize the SERS substrate design.

# 5. PULSED COOPERATIVE BACKWARD EMISSIONS FROM NON-DEGENERATE ATOMIC TRANSITIONS IN SODIUM*

## 5.1 Introduction

Species-specific remote sensing/spectroscopy in the sky has been a profound challenge in modern applied physics. The conventional atmospheric light detection and ranging (LIDAR) techniques [10, 11] have essential tools for detecting traces of air impurity at long distances. A tremendous amount of research has been devoted to upgrading conventional LIDAR techniques. Among them, the femtosecond-LIDAR, based on commercially available high intensity femtosecond (fs) lasers, has been demonstrated [76]. A fs filament formation [77] in air enables propagation of fs pulses for distances of tens of kilometers in scale. In any case, LIDAR techniques rely on incoherent light-scattering processes which are the fundamental limitation for LIDAR's performance. Therefore, an emerging new technology is inevitable.

Recently, coherent standoff spectroscopic (SOS) techniques have been proposed [12, 13]. In particular, one SOS technique [12] is intended to maintain a backward swept-gain for the successive two-photon induced superradiance (SR) [14, 15] / superfluorescence (SF) [16, 17] emissions. In general, in SF or SR, a macroscopic dipole moment of the medium builds up from initially incoherently or coherently excited atomic states. As an extension of the usual SF for two-level atoms, two-photon absorption laser-induced backward SF has recently been observed in cesium [21] and rubidium (Rb) [78, 79]. Coherent temporal control of backward SF in Rb vapor

---

*Reprinted with permission from "Pulsed cooperative backward emissions from non-degenerate atomic transitions in sodium" by Jonathan V Thompson, Charles W Ballmann, Han Cai, Zhenhuan Yi, Yuri V Rostovtsev, Alexei V Sokolov, Phillip Hemmer, Aleksei M Zheltikov, Gombojav O Ariunbold and Marlan O Scully, 2014. New Journal of Physics 16 103017, Copyright [2014] by IOP Publishing Ltd and Deutsche Physikalische Gesellschaft.

has been studied as an improvement over conventional standoff sensing [79], and highgain, directional backward superfluorescence emissions have been observed in air [18, 19]. The backward emissions interpreted as coherence-brightened laser-like [34] (via the presence of atomic coherence) and laser-like [18] (via the absence of atomic coherence) are produced from two-photon excited oxygen atoms as a result of the two-photon photolysis of oxygen molecules in ambient air. Numerical simulations [34] in terms of cooperative phenomena (SF, SR, etc) have been performed to elucidate the observed experimental results in [19].

In this chapter, we study the backward superfluorescent emissions (BSFEs) from two-photon excited sodium (Na) atomic vapor. There are many advantages to working specifically with Na atoms. This two-photon excitation mechanism of Na is similar to that in Ref. [18, 19]. However, any relaxations (collisions, dephasings, spontaneous emissions, etc), photolysis, or ionizations are discarded for dense Na vapor. This is because superfluorescent emissions occur for short timescales before other relaxation processes have any effect. It is also clean, in the sense that it involves the ground ($3S_{1/2}$) and the lowest possible two-photon excited ($4S_{1/2}$) states. Since the closely spaced Na D-lines are involved, one should expect double BSFEs that are in the infrared range (around 1140 nm). Conventional spectrometers and ultrafast streak cameras have adequate quantum efficiency in this wavelength range. This is not the case in the Rb atomic system, where the center wavelength of the BSFE is about 5 $\mu$m [79]. Moreover, the present research is of great interest from the viewpoint of standoff sensing with SF. The last, but not least, consideration that we mention here is the existence of an atomic layer of Na in the mesosphere. An extensive research effort has recently been dedicated to the practical implementations of an artificial Na laser guide star (LGS) for ground-based telescopes that can improve images distorted due to the atmospheric layer by using adaptive optical techniques

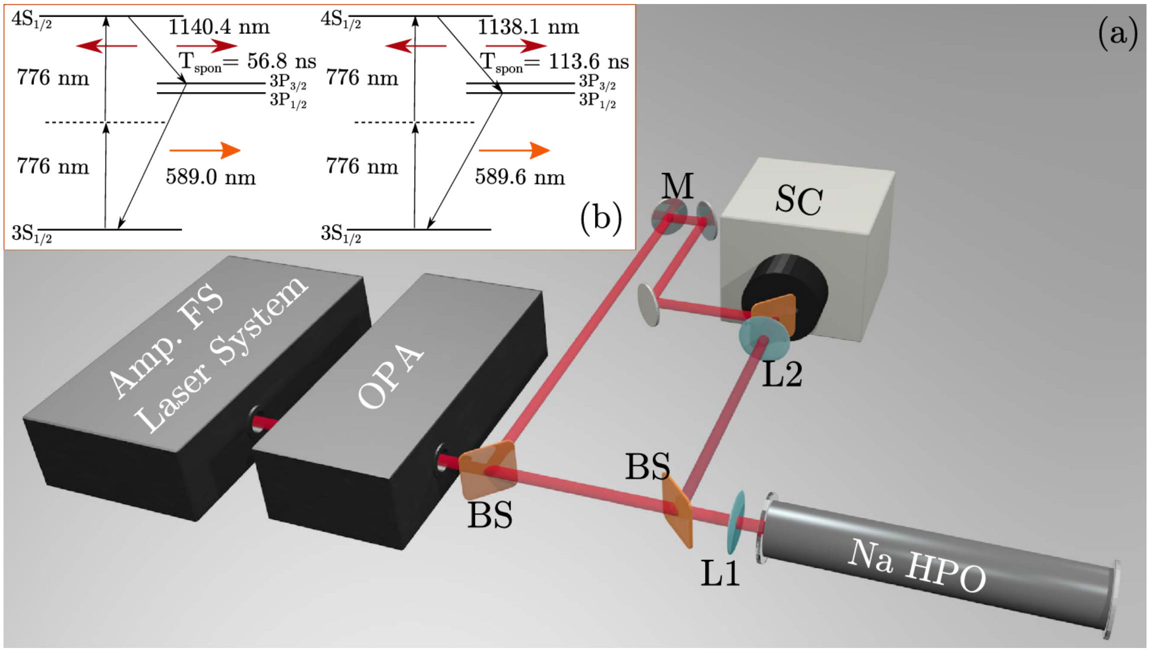

Figure 5.1: (a) Experimental setup: Amp. FS laser system (a femtosecond amplified laser system); OPA (optical parametric amplifier); BS (beamsplitter); L1,2 (lenses); SC (streak camera) and Na HPO (Na heat pipe oven at 450 °C). (b) The atomic level scheme.

[80]. The conventional approach for LGS is based on resonance fluorescence with the Na D2- line (589 nm) [81, 82, 83]. However, there are several fundamental limits [84], including the saturation effect and the limited number of return photons, to name two. To overcome the saturation effect, polychromatic LGS has been extensively studied.In spite of some scalability limitations, the present research may have possible applications in polychromatic LGS technology.

The rest of this paper consists of sections dedicated to the experimental setup, observed results, discussion of the results, and conclusions.

## 5.2 Experimental setup

In Figure 5.1(a), the experimental setup is sketched. The experimental setup consists of a commercial Ti:sapphire amplified laser system (Coherent, Inc.) with an optical parametric amplifier (OPA, Coherent, Inc. OPerA-VIS/UV), a homemade heatpipe oven containing Na metal (Na HPO), two types of fiber spectrometers (Ocean Optics USB2000+, STellarNet EPP2000-NIR-InGaAs), and a Hamamatsu (C5680 with a minimum resolution of 2 ps) streak camera. From the OPA we obtained 100 fs long pulses, centered at 776 nm with a 20 nm full width at half maximum (FWHM) and up to 17 mW average power at a repetition rate of 1 kHz. The beam size was about 3 mm. A reflective attenuator (not shown in Figure 5.1(a)) was used to control the power of the input beam to the heatpipe oven. The reference 776 nm input pulse shown in Figure 5.1(a) was used to remove laser jitter and obtain relative pulse delay with the streak camera. Its temporal width of about 5 ps also determines the camera resolution obtained in the experiment. Either a 40 or 50 cm focal-length lens was used to focus the input beam into the middle of the heatpipe oven. The properties of the BSFE were qualitatively reproducible for both cases. Therefore, in the following, only the results from the 40 cm lens configuration are presented. Fifteen grams of Na were loaded into the center of the pipe at the time of construction [85, 86]. The heatpipe oven has an inner diameter of 2.5 cm, a total length of 61 cm, and tilted windows to avoid reflections. The heated region is about 15 cm long with a density of $1.7 \times 10^{16}$ atoms per $\text{cm}^3$ at 450 °C and 15 Torr Argon (buffer gas) pressure. A 1 mm microscope glass slide was used as a beam splitter for detection of the backward emissions.

The Na atomic level scheme and two-photon excitation mechanism are shown in Figure 5.1(b). The input 776 nm ultrashort pulses excite the Na atoms via a two-photon process resonant to the $3S_{1/2} - 4S_{1/2}$ transition. The macroscopic atomic dipole moment can eventually build up to initiate the backward and forward SF emissions at 1140 and 1138 nm (on the $4S_{1/2} - 3P_{3/2}$ and $4S_{1/2} - 3P_{1/2}$ transitions, respectively) as well as the forward SF emissions at 589.0 and 589.6 nm (on the

$3P_{3/2} - 3S_{1/2}$ and $3P_{1/2} - 3S_{1/2}$ transitions, respectively). The forward SF emissions occur simultaneously, and are also referred to as yoked-SF [21]. The generated BSFEs at 1140 and 1138 nm were filtered to eliminate a residual of the 776 nm light by an 830 nm long-pass filter (Semrock, EdgeBasic BLP01-830R-25). To measure the generated forward signals, the microscope glass slides were also used (not shown in Figure 5.1(a)).

## 5.3 Observed results

The backward emissions are measured both by spectrometer and streak camera. A simple measurement of the backward emission yields an estimate of the divergence angle to be no larger than 17.5 mrad. The spectra of the backward emitted light were collected by the spectrometer and averaged over 20 samples for different input power.

The normalized spectra are plotted in two different ways in Figure 5.2. Note here that the resolution of the spectrometer ($\sim 0.7$ nm) is not sufficient to clearly separate the 1140 nm and 1138 nm emission peaks. The edges at the spectral FWHM are plotted by white solid curves. As we see in Figure 5.2, the normalized spectra become broader to the blue-side as power increases. This is because of an increased portion of the 1138 nm spectral component in addition to 1140 nm in the actual measured spectra.

The integrated intensity of the backward spectra is plotted as a function of input power as blue circles in Figure 5.3. The nonlinear power dependence of the integrated intensity on input power is demonstrated. Backward emitted light was also focused into the streak camera with a 10 cm lens. Two hundred samples were taken by streak camera for each power setting. Some averaged temporal profiles (filled green curves) of the BSFEs for different input powers are also shown normalized in log-

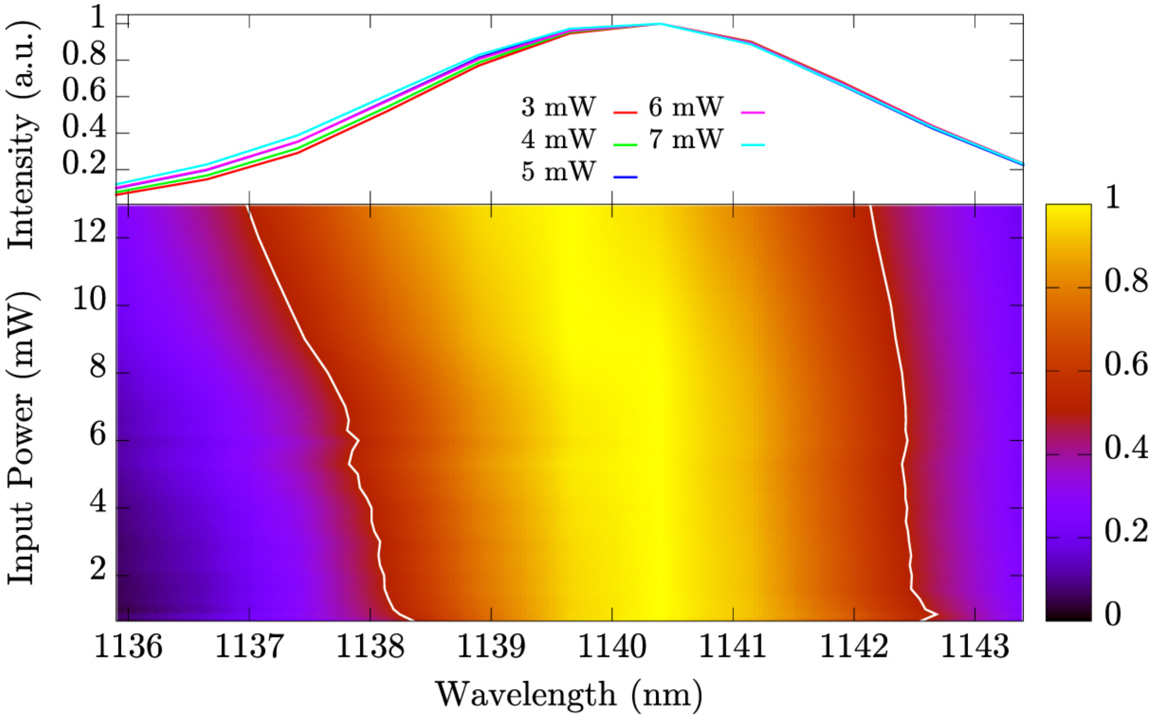

Figure 5.2: The spectra of BSFEs as functions of input power where the three dimensional figure in the bottom was interpolated from experimental data.

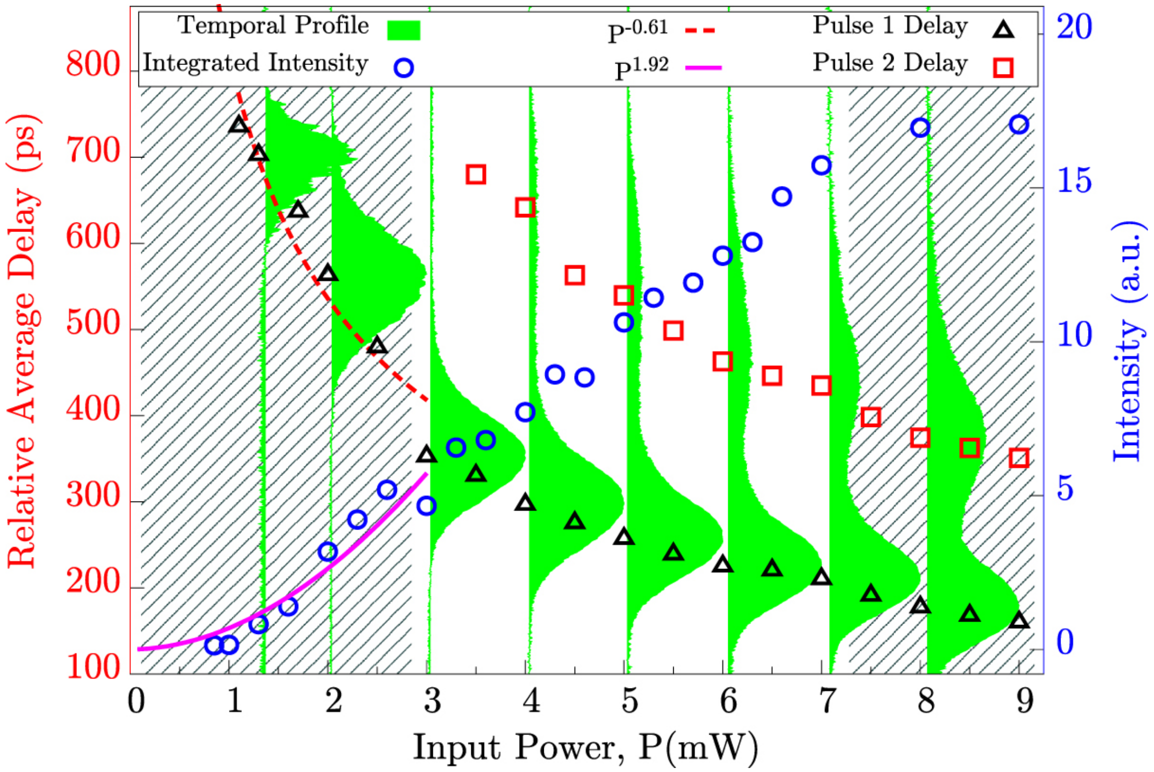

Figure 5.3: Experimentally observed data. The averaged temporal pulse shapes (in log-scale and normalized), relative average time delay, and integrated intensity of the backward emitted light as functions of input power are depicted by the filled green curves, red squares and black triangles, and blue circles, respectively.

scale in Figure 5.3. For low-input power (below 3 mW), only the 1140 nm SF was measured. In this case, the average delay and integrated intensity are fitted with $\sim P^{-1}$ and $\sim P^2$, respectively, where $P$ is the input power. Note that since the threshold power is too small, it is not included here. This type of pure/single SF has already been studied in the literature [21, 78, 79]. However, for input power above 3 mW, picosecond time-resolved double SF pulses were recorded. We identify the second, delayed pulse as a 1138 nm SF pulse, as seen in Figure 5.2. We obtained the average delay of the SF pulses with respect to the incident pump laser (reference) pulse and its dependence on the input laser intensity. The average time-delay of the 1140 nm and 1138 nm SF pulses relative to the reference input pulse are plotted as functions of input power, shown as black triangles and red squares, respectively, in Figure 5.3. Additionally, the forward SF pulses on the upper and lower transitions were also measured for different input powers. The ratio between the forward and backward SF (at about 1140 nm) pulse energies on the upper transitions was about 30. The conversion efficiency of the input 776 nm into the backward emission was 0.0035 %.

## 5.4 Discussion

A cooperative emission in two nonidentical atoms has been theoretically studied in reference [87]. Similarly, cooperative emissions from nondegenerate atomic transitions are sophisticated, and rigorous experimental and theoretical tests are beyond the framework of the present work. Clearly, a simultaneous observation of the double SF pulses in atomic vapor is intriguing in its own right. To understand the observed data, we estimate the following. For the sake of simplicity, half of the excited atoms independently emit 1140 nm SF pulses, and the other half emit 1138 nm SF pulses. An SF scaling parameter, $\tau_R \sim T_{spon}/N$, and an initial (tipping) angle are the only parameters necessary to fully determine the whole SF process [17], where $T_{spon}$ and $N$ are the spontaneous lifetime and number of excited atoms, respectively.

We observe that the spontaneous lifetime, $T_{spon}$, for the $4S_{1/2} - 3P_{3/2}$ transition (56.8 ns) is two times faster than that for the $4S_{1/2} - 3P_{1/2}$ transition (113.6 ns). Consequently, the 1138 nm SF pulse is delayed by two times more than the 1140 nm SF pulse. From this simple statement, one can find an offset between the relative and absolute time-delay for each power. This is a complicated task to determine experimentally. Our analysis is for the unshaded region in Figure 5.3, (i.e., the interval between 3 to 7 mW input power). The offset corrected data for this region are shown in Figure 5.4, where the offset was about 17 ps and depended very little on input power. The data were fitted with power laws. As a result, the SF delay is approximately proportional to the inverse of the input power. Note that for two-photon excitation, the number of excited atoms is proportional to the square of the input power. Therefore, this is quantitative evidence that each of the backward 1140 nm and 1138 nm emissions is independently governed by the laws of oscillatory SF phenomena. Similar (single, but not double) oscillatory SF in Rb vapor was reported in our earlier work [88].

Naively, one would expect that starting from the same excited level, $4S_{1/2}$, to two states, $3P_{1/2}$ and $3P_{3/2}$, the SF would go via the channel with larger coupling to electromagnetic radiation, similar to mode competition in laser physics [26]. In Figure 5.3, we actually observe two SF pulses. Their relative intensities depend on the level of pump intensity, but the delay times for both SF pulses are different by a factor of 2. This is related to the different electric dipole moments for these transitions because the delay time is inversely proportional to the spontaneous emission rate, $\gamma$. For these two transitions, the spontaneous lifetime and cooperative frequencies differ by this same factor of 2. Indeed, the SF pulse (Rabi frequency) starts as $\Omega_{SF} \propto$

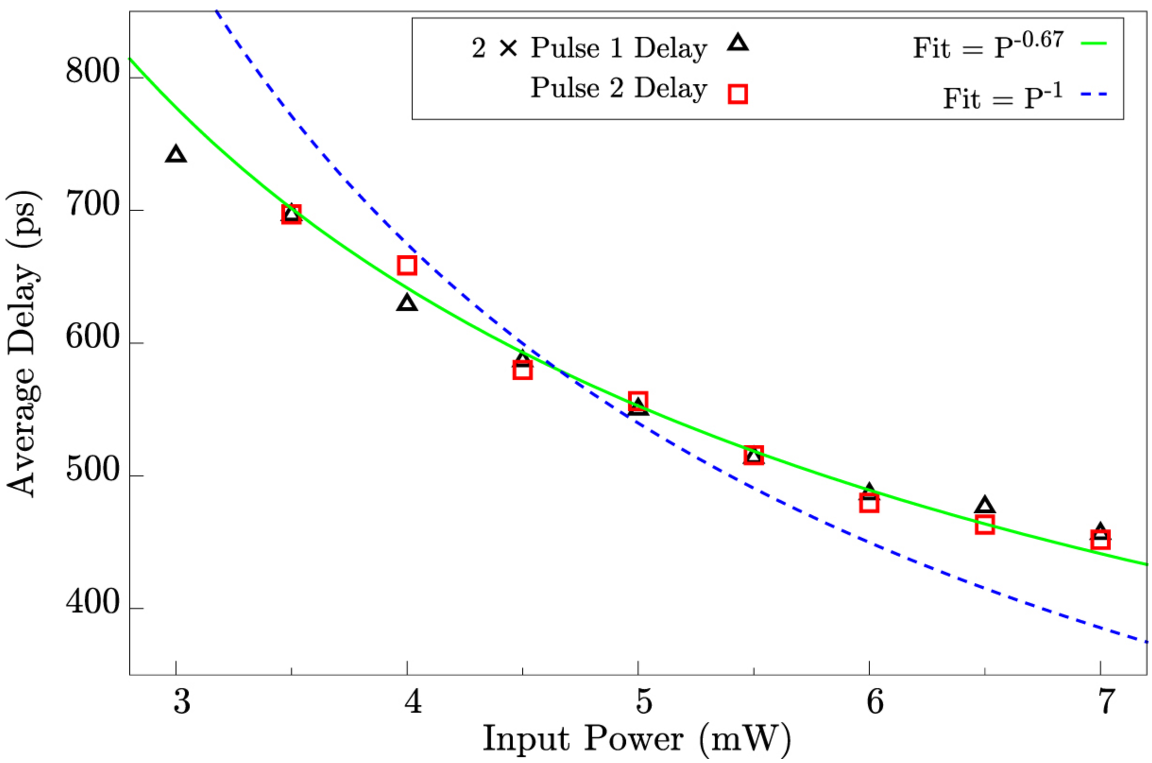

Figure 5.4: Absolute average time delay of the BSFE with the measurement-related offset removed. The time delay of the 1140 nm BSFE is multiplied by a factor of two to show its relationship with the 1138 nm time delay. The data points are fitted by a power law.

$\sqrt{D\gamma/t}I_1(2\sqrt{2D\gamma t})$, and the delay time, $t_{delay} \simeq 1/(D\gamma)$, where $D = 3\lambda^2 Nz/(8\pi)$, $I_1$, $t$, $z$, and $\lambda$ are the linear optical density, first-order Bessel function, time, pulse propagation distance, and SF center wavelength, respectively. Because the delays of the SF pulses are different by a factor 2 (the ratio of the spontaneous emission rates), they do not overlap in space, and the coherence between the $3P_{1/2}$ and $3P_{3/2}$ states does not play any role.

Based on the simplified theoretical estimations, we find the total number of excited atoms, $N$, to be $10^{10}$ and the $\tau_R$ for the 1140 nm SF pulse to be $\tau_R \approx 20$ ps at an input power of 2 mW. As expected, the two sets of time-delay data for the 1140

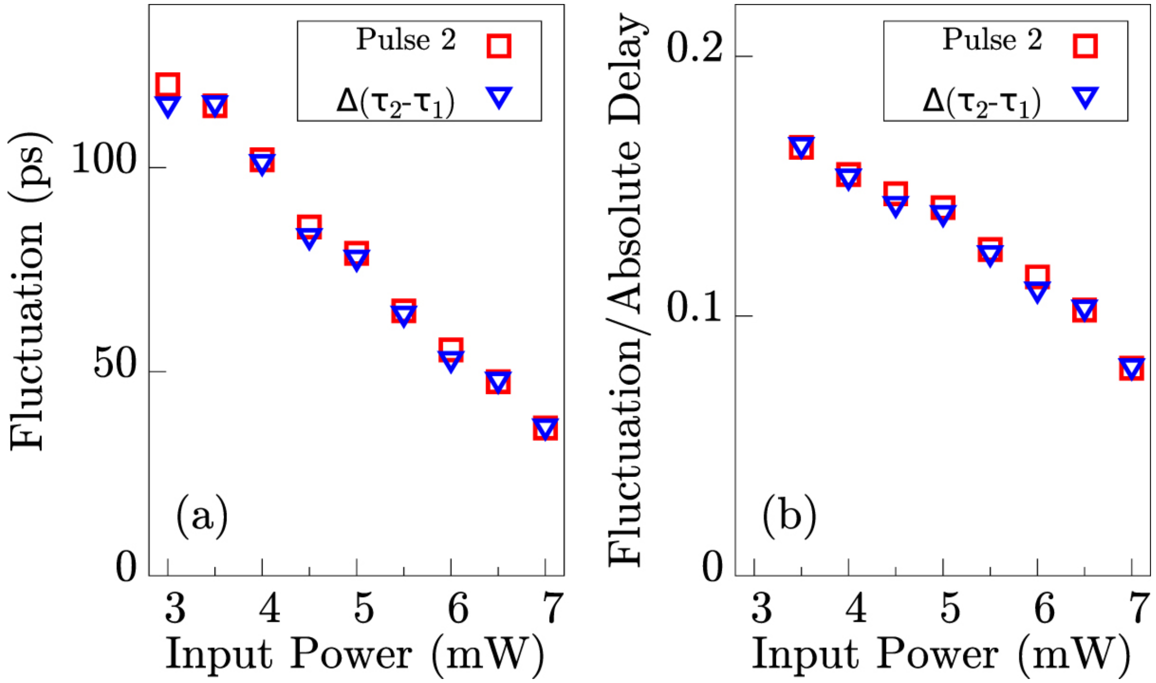

Figure 5.5: Root-mean-square fluctuations $\left(\sqrt{\langle(\Delta\tau_i)^2\rangle}\right)$ in time delay of the 1138 nm SF pulses as a function of input power. (b) The ratio of the fluctuations and average time delay $\left(\sqrt{\langle(\Delta\tau_i)^2\rangle}/\langle\tau_i\rangle\right)$ versus input power.

nm and 1138 nm SF pulses coincide by a factor of two, as shown in Figure 5.4. Due to a high gain factor used when recording data with the streak camera, the temporal shape of the 1140 nm pulse might be distorted compared to the 1138 nm pulse. We obtained the width of the 1138 nm SF pulse for different input powers and compared it to the average time delay. The 1138 nm pulse width is inversely proportional to input power.

We also attained the time delay fluctuations for each backward SF pulse separately via the formula $\sqrt{\langle(\Delta\tau_i)^2\rangle} = \sqrt{\langle\tau_i^2\rangle - \langle\tau_i\rangle^2}$, where $\tau_i$ is the time delay of a single BSFE relative to the laser reference pulse, as captured by the streak camera. Additionally, histograms for the statistical distribution as in reference [89] were constructed. The fluctuation of the 1138 nm SF as a function of input power is shown in Figure 5.5(a). The time-delay fluctuations decrease as input power increases. The quantum fluctuations in alkali vapor were measured in references [90, 89]. The fluctuations of the difference between the two pulses were also obtained and shown in Figure 5.5. This difference removes the non-reproducible extrinsic fluctuations (e.g., the laser pulse shot to shot noise). The power dependence of the ratio between the fluctuations and average time delay is shown in Figure 5.5(b). It is interesting to point out that this ratio for the 1138 nm SF pulses clearly demonstrates an inverse dependence on input power, as is expected. A quantum theory predicts this ratio for SF from $N$ two-level atoms to be proportional to $1/\ln(N)$ [91].

The present study of backward emissions from Na is important for LGS technology. Although several worldwide large telescopes already operate with LGS, the number of return photons is fundamentally limited [81]. To overcome these specific limitations, so-called polychromatic LGS has emerged [82]. The concept of polychromatic LGS is to utilize either single-photon (at 330 nm [83]) or nondegenerate two-photon (at 569 and 589 nm [84] or at 1140 and 589 nm [81]) excitations of Na atoms and detect cascade fluorescence at different wavelengths, including 589 nm. In particular, the pulsed bichromatic LGS scheme proposed in Ref. [81] uses nondegenerate two-photon excitation, whereas a resonant degenerate two-photon excitation is used in the present work. In Ref. [81] they estimated that for their bichromatic LGS scheme, about 50 photons (25 times above the detection limit) can be collected in a solid angle of $\sim 10^{-9}$ steradian (sr) from the $4\pi$ sr-radiated fluorescence from $\sim 10^{12}$ excited atoms in the sodium layer of the mesosphere. The tendency of directionality of BSFE increases the number of return photons in the same solid angle ($10^{-9}$ sr). A simple estimation has been given in our previous work [79], where it is estimated that a 100 J laser pulse directed into the mesosphere would return a photon flux of

$10^8$ per second, per square centimeter. We estimate there to be hundreds of return photons.

## 5.5 Conclusion

In conclusion, we observed backward cooperative emissions from nonidentical Na atomic species. Temporally well-separated, nondegenerate double superfluorescence pulses were measured. The average time delay and its fluctuations of the measured superfluorescence pulses are determined with minimum possible systematic/experimental errors.

The present excitation scheme, which could be applied as a type of polychromatic laser guide star, has several advantages over conventional, monochromatic laser guide star. For instance, the fundamental problems of saturation (less than 50% of the atomic population can be transferred to the excited state via one-photon processes) and differential tilt (refraction due to the atmosphere) can be solved using the present two-photon excitation scheme with or without involving cooperative phenomena where nearly 100% population excitation can be achieved; differential tilt can be corrected with a polychromatic (double superfluorescence pulses) return signal. Although only about four sodium atoms per $\mathrm{mm}^3$ exist in the mesosphere, a 10 km-thick layer could still validate cooperative effects via e.g., gain sweeping and provide for a better collimation in the backward direction, thus increasing the number of return photons. A rigorous numerical simulation for both fluorescence (the same as in reference [81]) and superfluorescence (together with an implementation of the backward swept-gain technique [12]) from the Na layer utilizing the present two-photon excitation mechanism will be given elsewhere.

# 6. OBSERVING THE TRANSITION FROM YOKED SUPERFLUORESCENCE TO SUPERRADIANCE*

## 6.1 Introduction

Superradiant light sources have recently been investigated as “sky lasers” for atmospheric remote sensing applications [12, 13, 92, 93]. The efficiency of state-of-the-art backward lasers should be increased to enable many promising applications [18, 19]. Laboratory-scale simple schemes can be used to mimic more complicated atmospheric experiments and to help understanding the basic physics. Furthermore, the possibility to generate superrandiant UV and X-ray sources may lead to various biomedical applications [94, 95].

In his seminal work, Dicke predicted enhancement of the spontaneous emission rate from a system of coherently excited atoms confined to a region with dimensions smaller than the wavelength [14]. This effect is known as Dicke superradiance (SR) [96, 97]. Collective spontaneous emission from extended atomic samples was later studied by Eberly and Rehler [15]. The first experimental demonstration of the cooperative emission effect was performed by Skribanowitz *et. al.* using optically pumped HF gas [98]. MacGillivray and Feld provided a theoretical explanation of how an initially inverted two-level system evolves into a superradiant state [17, 99].

When the macroscopic dipole develops spontaneously in a system of incoherently excited atoms, the resulting cooperative emission is called superfluorescence (SF) [16, 100]. SF also produces a short pulse similar to SR but with a characteristic time delay due to the time needed to generate the coherence. Recent experimental

---

*Reprinted with permission from “Observing the transition from yoked superfluorescence to superradiance” by Zhenhuan Yi, Pankaj K. Jha, Luqi Yuan, Dmitri V. Voronine, Gombojav O. Ariunbold, Alexander M. Sinyukov, Ziyun Di, Vladmir A. Sautenkov, Yuri V. Rostovtsev, and Alexei V. Sokolov, 2015. Optics Communications 351 (0), 45-49, Copyright [2015] by Elsevier B.V.

demonstrations of new SF sources were realized in atomic [101] and semiconductor systems [102]. In a three-level cascade scheme (Fig. 6.1), the radiation from the lower transition ($a \to b$) is generated by the coupling between the two-photon pumping ($b \to c$) and the SF between levels $c$ and $a$. Thus the name yoked superfluorescence (YSF) is used to indicate the coupling of the two simultaneous radiation fields [21]. This phenomenon has been studied both theoretically [103, 104] and experimentally [21, 88, 79, 105, 106]. Picosecond time-resolved studies of SR [107, 108] and SF [109] were explored recently. Also the transitions between various regimes of cooperative emission based on the system parameters, such as the temperature or collisional dephasing, were investigated [34, 110, 111]. It is interesting to compare SR and YSF between the same atomic levels and to obtain laser control parameters to optimize intensity and pulse shape of the cooperative emission.

In this chapter, we investigate the generation of the 420 nm radiation from an atomic vapor of $^{87}$Rb. The atoms are excited by two photons from the $5S$ to $9S$ states by using ultrashort laser pulses centered at 656 nm (Fig. 6.1). We consider two scenarios. First, in the pure YSF, the pump pulse generates coherence between the $5S$ and $9S$ states and transfers population to the upper level, leading to population inversion and SF on the transition between the levels $9S$ and $6P$. The coupling between the SF and the coherence generates 420 nm YSF radiation on the lower transition between $6P$ and $5S$ in the forward direction with respect to the pump pulse. The second scenario is a three-photon-induced SR process. We drive the $9S \leftrightarrow 6P$ transition by ultrashort laser pulses centered at 1491 nm and temporally overlapped with the pump pulse. We compare the 420 nm signals with and without the drive field. Numerical simulations using master equations are in a good qualitative agreement with the experimental results.

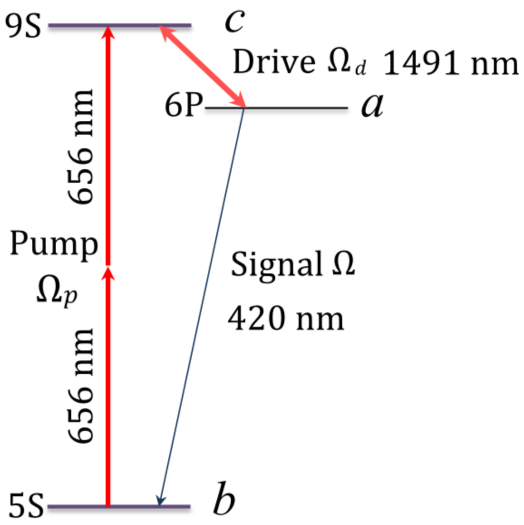

Figure 6.1: Simplified energy level diagram of $^{87}Rb$. $\Omega$'s are the Rabi frequencies of corresponding fields.

## 6.2 Experimental procedure

The experimental setup is shown in Fig. 7.1. The 656 and 1491 nm, 60 fs laser pulses were collinearly focused into a thin 1.9 mm-long rubidium vapor cell. The cell is made of sapphire which allows high temperature operation and has a cylindrical shape with total length of 5.3 mm, two 1.7 mm-thick windows and a diameter of 1 inch. The generated signal was analyzed using a spectrometer and a picosecond streak camera. The 656 nm (pump) and 1491 nm (drive) laser pulses were generated from two optical parametric amplifiers (OPAs, Coherent) pumped by 800 nm, 30 fs laser pulses from a Ti:Sapphire femtosecond laser system (Coherent) with 1 kHz repetition rate. Both pulses were linearly polarized, with the same polarization. The pulse energy of each beam was controlled by a continuous variable neutral density filter. The drive beam was sent through a pair of 90-degree cornered mirrors mounted on a digitally controlled translation stage (Newport) to precisely adjust the time

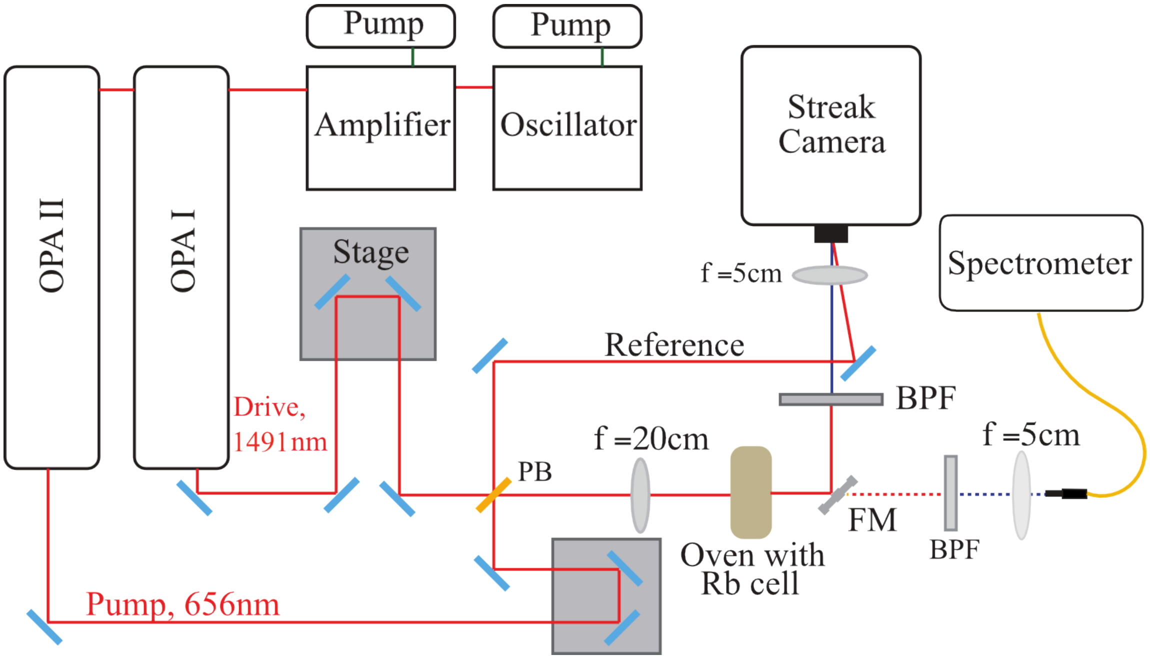

Figure 6.2: Experimental setup for observing the transition from YSF to SR. The pump and drive laser pulses are collinearly combined and focused onto the Rb cell. FM is a flip mirror; BPF is a band-pass filter centered at 420 nm with FWHM of 10 nm.

delay between the pump and drive pulses. Both beams were collinearly combined by a pellicle beamsplitter (PB) and were focused by a 200 mm focal length lens into the Rb cell. The number density of $^{87}$Rb atoms was estimated to be $1.3 \times 10^{15}$ cm$^{-3}$. The transmitted 656 nm beam after the PB was used as a reference for the streak camera. This beam and the generated signal from the cell were focused onto the entrance slit of the streak camera by a lens with focal length of 5 cm. The time resolution was optimized to $\sim 2$ ps.

## 6.3 Simulation

To get an insight into the temporal behavior of the SR signals in the experiment, a detailed numerical simulation was performed. The pump field ($\Omega_p$) is two-photon resonant with the transition between the levels $b$ and $c$ (See Figure 6.1). The drive field ($\Omega_d$) is resonant with the upper transition between the levels $c$ and $a$. The pump and drive fields are fully coherent laser pulses generated from OPAs as described in section 6.2. They were modeled as Gaussian functions in eqs. (2)-(6). The coherent drive field generates coherence between levels $c$ and $a$ which leads to cooperative emissions. The emitted field ($\Omega$) is generated at the lower transition through the field propagation equation

$$\frac{\partial \Omega}{\partial z} + \frac{1}{c}\frac{\partial \Omega}{\partial t} = i\eta\rho_{ab}, \tag{6.1}$$

with the coupling constant $\eta = \frac{3}{8\pi}N\lambda^2\gamma$, where the atomic number density is $N \sim 10^{15}$ cm$^{-3}$, the wavelength of this transition $\lambda = 420$ nm, and the spontaneous emission rate $\gamma \sim 6$ $\mu$s$^{-1}$. The density matrix was calculated using the master equation [3]. The detailed simulation procedure can be found in reference [34]. Briefly we used the following equations,

$$\begin{aligned}
\dot{\rho}_{ca} &= -\Gamma_{ca}\rho_{ca} - i\Omega_d(\rho_{cc}-\rho_{aa}) - i\Omega^*\rho_{cb}, && (6.2)\\
\dot{\rho}_{ab} &= -\Gamma_{ab}\rho_{ab} - i\Omega(\rho_{aa}-\rho_{bb}) + i\Omega_d^*\rho_{cb}, && (6.3)\\
\dot{\rho}_{cb} &= -\Gamma_{cb}\rho_{cb} - i\frac{\Omega_p^2}{\Delta}(\rho_{cc}-\rho_{bb}) + i\Omega_d\rho_{ab} - i\Omega\rho_{ca}, && (6.4)\\
\dot{\rho}_{cc} &= -\gamma_{ca}\rho_{cc} + \left(i\Omega_d\rho_{ac} + i\frac{\Omega_p^2}{\Delta}\rho_{bc} + c.c.\right), && (6.5)\\
\dot{\rho}_{aa} &= \gamma_{ca}\rho_{cc} - \gamma_{ab}\rho_{aa} + \left(-i\Omega_d\rho_{ac} + i\Omega\rho_{ba} + c.c.\right), && (6.6)
\end{aligned}$$

$$\rho_{aa} + \rho_{bb} + \rho_{cc} = 1. \tag{6.7}$$

where Ω's are the Rabi frequencies of corresponding fields; $\rho$'s are components of density matrix; $\Gamma_{ij}$ is the decoherence rate between level $i$ and level $j$, $\gamma_{ij}$ is the spontaneous decay rate from level $i$ to level $j$, and $\Delta$ is the single photon detuning between the pump field and the nearest intermediate state, which is state 5P in this case.

The pump and drive pulses were focused into a 1.9-mm-long pencil-like active medium with the cross-sectional area of $10^{-9}$ m$^2$. The pump field generates coherence $\rho_{cb}$ and transfers part of the population into the level $c$. If there is no drive field, then the population inversion will induce the SF on the upper transition. The coupling between this SF and the coherence $\rho_{cb}$ results in the emission on the lower transition. When we apply a strong drive field on the upper transition, it will dominate over the weak SF field and will couple with the coherence $\rho_{cb}$ to generate a stronger signal field on the lower transition.

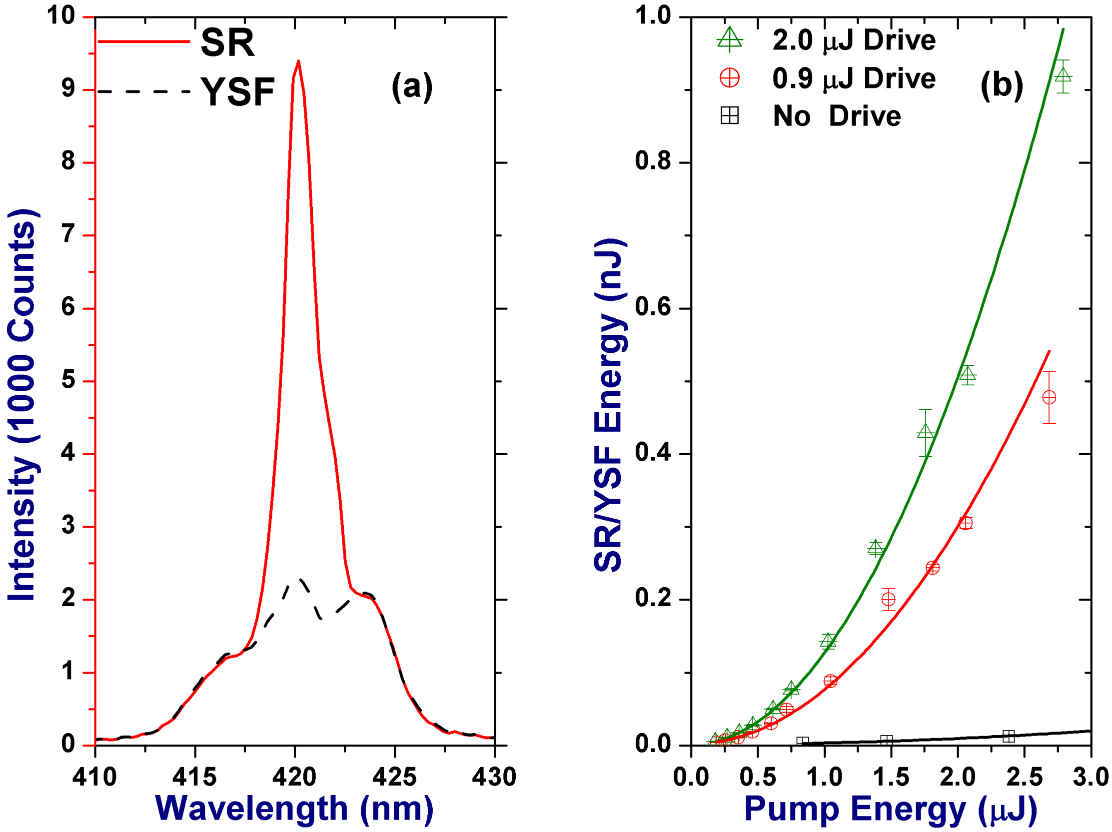

Figure 6.3: (a) Cooperative emission spectra on the $6P \rightarrow 5S$ transition with 0.9 mW (solid red) and without (dashed black) drive. (b) Pump energy dependence of the 420 nm emission peak without drive (black squares) and with 0.9 mW (red circles) and 2.0 mW (green triangles) drive. The solid lines are parabolic fits.

## 6.4 Results

The spectra of the SR (solid red) and YSF (dashed black) are shown in Figure 6.3(a). They were obtained with 0.9 mW average power and without drive, respectively. The broadband background was cut off by the bandpass filter. Both spectra show a peak at 420 nm. The SR intensity is an order of magnitude stronger than that of YSF.

Pump energy dependence was measured for no drive (black squares) and for two drive powers: 0.9 mW (red circles) and 2.0 mW (green triangles), as shown in Figure 6.3(b). Solid lines are parabolic fits of the data, indicating a two-photon nature of the pumping process for the SR signals. This can be seen from Eqs. (6.1), (6.3) and (6.4), which show that the signal Rabi frequency ($\Omega$) is proportional to the square of the pump Rabi frequency ($\Omega_p$) in the linear regime: $\Omega \propto \rho_{ab} \propto \Omega_d^* \rho_{cb} \propto \Omega_d^* \Omega_p^2$. There was a large increase in the output of the 420 nm signal with the increase of the drive energy. This can be understood qualitatively as follows. The 420 nm emission is induced by the coherence on the $6P \rightarrow 5S$ transition ($\rho_{ab}$), which depends on the coupling between the coherence on the $9S \leftrightarrow 5S$ transition ($\rho_{cb}$) and the drive field ($\Omega_d$). When the drive power is low, this dependence is linear, so there is more energy deposited in the $6P \rightarrow 5S$ transition for the drive power 0.9 mW compared to the YSF process (no drive). However, further increase in the drive power brings the system into a non-linear regime. Therefore, the signal at 420 nm will not increase as much as it does in the linear regime (See the plot for the 2 mW drive in Figure 6.3(b)). Using these measurements, we estimated a factor of ∼30 increase in the conversion efficiency of the SR with 2.0 mW drive with respect to YSF at the pump energy of 2.5 $\mu$J. Similar enhancement in lasing schemes using an external drive have been reported in other systems [112, 113, 114]. Recent studies of generation

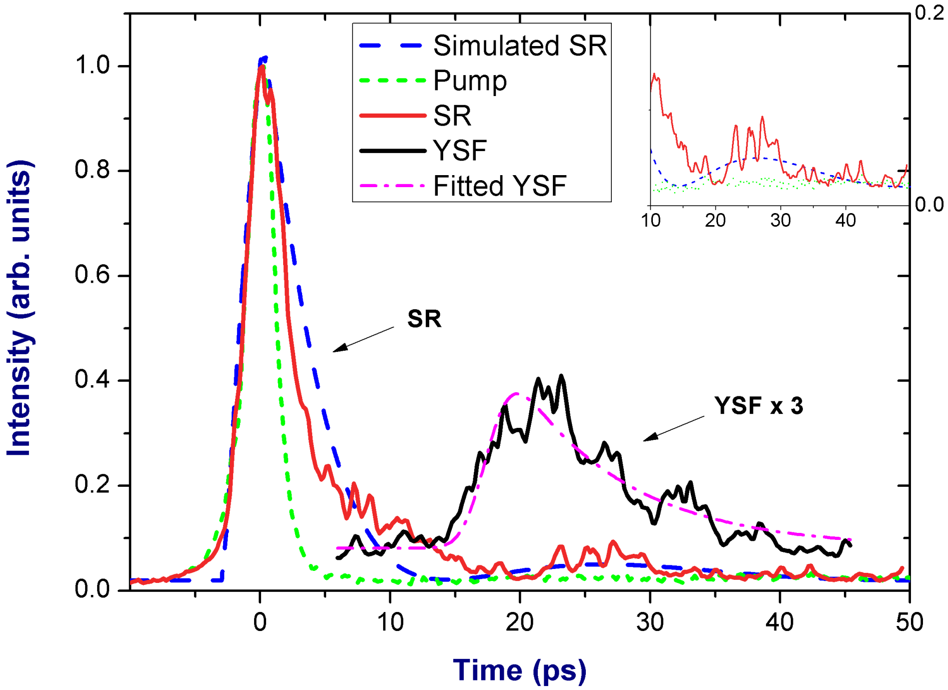

Figure 6.4: Temporal profiles of the pump pulse (solid green), YSF (solid black) and three-photon-induced SR (solid red) measured by a streak camera, together with simulated SR (dashed blue) and fitted YSF (solid magenta).The inset shows a zoom-in region containing the weak SR oscillation.

of directional coherent emission in Rb vapor using continuous-wave lasers achieved higher efficiency [115, 116]. The difference of those studies from our work is the four wave mixing (FWM) origin of the 420 nm emission versus the SR-enhanced nature of the radiation. The similarity is that the interplay between the population and coherence leads to radiation enhancement. This indicates the possibility of extending these techniques to a broader range of energy level schemes and to different atomic systems for mirrorless generation of coherent radiation.

The temporal behavior of the SR and YSF signals is shown in Figure 6.4. The experimental curves are averaged over the data collected by the streak camera. One unit of the intensity (Y-axis), based on our estimation, correspond to $\sim 1.2$ Watt in power. The pump pulse (solid green) is reference for time zero, and is normalized to the height of SR. The 60-fs pump pulse generates a  2.4 ps signal on the streak camera due to its convolution with the instrument response function. The drive pulse arrives at the same time with the pump. A time delay of $\sim$ 17.5 ps for the YSF signal is observed. This is necessary to build up enough coherence to generate the SF at the $9S \rightarrow 6P$ transition. The YSF pulse has a duration of $\sim$ 9 ps. Introduction of the 2.0 mW drive field leads to the SR pulse bursts without delay, and with a shorter pulse width. This is because the drive pulse arrives at the same time with the pump and is strong enough to induce the coherence between $9S$ and $6P$ states instantaneously, so that the cloud of atoms emits the SR without delay.

The simulated SR pulse (dashed blue) is also shown in Figure 6.4. The simulation gives a good qualitative description of the experiment. The quantitative comparison is, however, beyond this level of theory. Therefore the maximum of the simulated SR curve was fit to the maximum of the experimental SR signal. The pulse shape consists of a strong peak followed by a weaker oscillation and corresponds to the experimental SR pulse shape (solid red). The weak oscillation appears as a minor bump. However, it is a significant feature of the cooperative emission which is present both in the experiment and simulation. The inset in Figure 6.4 shows a zoom-in region containing the weak oscillation. Similar oscillating (ringing) behavior has recently been observed and simulated in coherence-brightened oxygen laser studies [19, 34]. The nature of such oscillations indicates that the coherence plays an important role. Because the relaxation times here are much longer than the time-window of interest ($\sim$ 100 ps). Oscillating behavior has also been observed in other Rb experiment [108]. However, long optical path of the cell used in this experiment modulated the pulse shape. Here we used a thin cell with a short optical path. Therefore, the pulse propagation effects in SR can be neglected and oscillations due to collective emission are more clearly observed. However, the physics of the YSF process is different and the pulse propagation effects cannot be neglected because the upper transition collective damping time much smaller than the signal propagation time. The $\sim 0.2$ THz oscillation in the YSF signal can be attributed to propagation effects.

We fit the YSF data with a exponential decay model which takes into account the convolution with the resolution streak camera response function:

$$P(t) = \int_{t_0}^{\infty} Ae^{-\frac{\tau - t_0}{\tau} - 2\frac{(t-\tau)^2}{w^2}} d\tau + A_0, \tag{6.8}$$

where $A$ and $A_0$ are the signal peak power and background, respectively, $t_0$ is the delay and $\tau$ is the decay time. $w$=2.4 ps is the the streak camera resolution. The fitting gives $t_0 = 17.5$ ps and $\tau = 8.6$ ps. To compare these results with theoretical predictions, we recall the collective damping time [117] which is related to the width of the YSF signal is

$$\tau_r = \frac{8\pi}{3} \frac{T_1}{n\lambda^2 L}, \tag{6.9}$$

where $T_1$ is the spontaneous lifetime, $\lambda$ is the wavelength, $L$ is the length of the excited atomic emsenble, and $n$ is the excited atom density. The delay time [118] is giving by

$$\tau_D = \tau_r [\frac{1}{4} \ln(2\pi N)]^2, \tag{6.10}$$

where $N = nAL$ is the total number of excited atoms in the gain volume, $A$ is the cross-section area of the medium. The decay time of YSF is determined by $T_1$ of the lower transition $a \to b$ while the delay time is determined by $T_1$ of the upper transition $c \rightarrow a$, which can be estimated it using Weisskopf-Wigner theory [3]. These equations predict the signal decay time $\tau_r \simeq 9$ ps, which agrees our fit parameters of 8.6 ps, and the delay of $\tau_D \simeq 5$ ps which is shorter than our fit of 17.5 ps. The experimental measurements and the theoretical predictions match each other quantitatively well. The slight difference could be due to uncertainty of the $T_1$ estimations.

## 6.5 Conclusion

In this chapter, we investigated the SR and YSF emission at 420 nm in $^{87}$Rb, with/without a drive field on the $9S \rightarrow 6P$ transition, respectively. We observed the transition from YSF to SR by varying the power of the drive field and measured an increase in radiation energy, with ∼30 fold increase in the conversion efficiency. The temporal profiles of both the YSF and SR were measured and a numerical simulation of the SR was compared with the experimental results. The theoretical formalism may be applied to other related experiments such as the coherence-brightened air laser [19]. Our work combines the investigations of the YSF and SR under comparable conditions and provides an important step in the research of the cooperative emission behavior in a dense atomic medium. We expect similar results could be observed in other alkali vapors.

# 7. DUAL PATHWAY QUANTUM BEAT*

## 7.1 Introduction

Quantum coherence plays a very important role in many advances in quantum detection and control technics recently, such as Coherent anti-stokes Raman scattering Spectroscopy (CARS), multidimensional Fourier Transform Spectroscopy and wave packet control of atoms and molecules [9, 119, 120], in the sense that optical interference (beating) can reveal the quantum path along which the system evolves, and enable us to work with it. It has also been demonstrated that by comparing the shape of the Fourier spectra of measured quantum beat patterns to theoretical model, number of atoms involving in dipole-dipole interaction can be characterized in an excited atomic ensemble [121].

Many of these quantum beating experiments [122, 123, 107] were done in a pump-probe configuration which one pulse was split into two, one as pump and the other as probe, and the delay between the pump and probe pulses was scanned to get the beat pattern. At the density of atoms (or molecules) when quantum beating were observed, the first few or ten picoseconds of the coherent optical signal showed exponential decay envelopes. This was attributed to superfluorescence (SF) processes, here we will present experimental data to help clarify the time scale for this process. In our experiment, we used two beams at different wavelength for pumping and for probing, which also enable us to see some transition which are weak or negligible in other experiments [124].

In this chapter, we investigate the quantum beat via the 420 nm and 421 nm radiation from an atomic vapor of $^{87}$Rb (Figure 7.1 B)). The atoms are excited by two

---

*"Dual pathway quantum beat" by Zhenhuan Yi, Tuguldur Begzjav, Gombojav O. Ariunbold, Aleksei M. Zheltikov, Alexei V. Sokolov and Marlan O. Scully, 2016, in preparation.

photons from the $5S$ to $9S$ and $7D$ levels by ultrashort laser pulses with broadband spectrum centered at 656 nm. The broadband probe pulse centered at 1491 nm couples the fine structure levels of $9S$, $7D$ to that of $6P$. According to selection rules, all transitions from $9S$ and $7D$ to $6P$ are allowed except the $7D_{5/2} \rightarrow 6P_{1/2}$ transition. And the sum rule [1] tells us that the transition intensity of the three labeled ones in the figure are $a : b : c = 5 : 1 : 9$. For sake of simplicity, if we temporally ignore the transition $b$, we see that if one scans the delay between pump and probe pulses, the beat frequency $\Delta_1/2\pi$ can be seen on the 420 nm transition while the 421 nm transition can show the beat frequency of $\Delta_2/2\pi$ . Furthermore, since the two channels are coupled through levels $9S$ (and weakly via $7D_{3/2}$), multi-photon processes (Figure 7.1 C)) reveal themselves through beat frequency of $\Delta_2 - \Delta_1$. All these happen in typical SF time scale of $\sim$ 20 picosecond. In the following part of this paper, we discuss these aspects in detail.

## 7.2 Experiment

The experimental setup is shown in Figure 7.1 A). The femtosecond laser pulses with wavelength centered at 656 and 1491 nm were collinearly focused into a thin rubidium vapor cell. The cell is made of sapphire which allows high temperature operation and has a cylindrical shape with total length of 5.3 mm, two 1.7 mm-thick windows and a diameter of 1 inch, Rb vapor fills the 1.9-mm long space between the windows. The generated signal was analyzed using a spectrometer (Ocean Optics). The 656 nm (pump) and 1491 nm (probe) laser pulses were generated from two optical parametric amplifiers (OPAs, Coherent) pumped by 800 nm, 30 fs laser pulses from a Ti:Sapphire femtosecond laser system (Coherent) with 1 kHz repetition rate. Both pulses were linearly polarized, with the same polarization. The pulse energy of each beam was controlled by a continuous variable neutral density filter. The probe

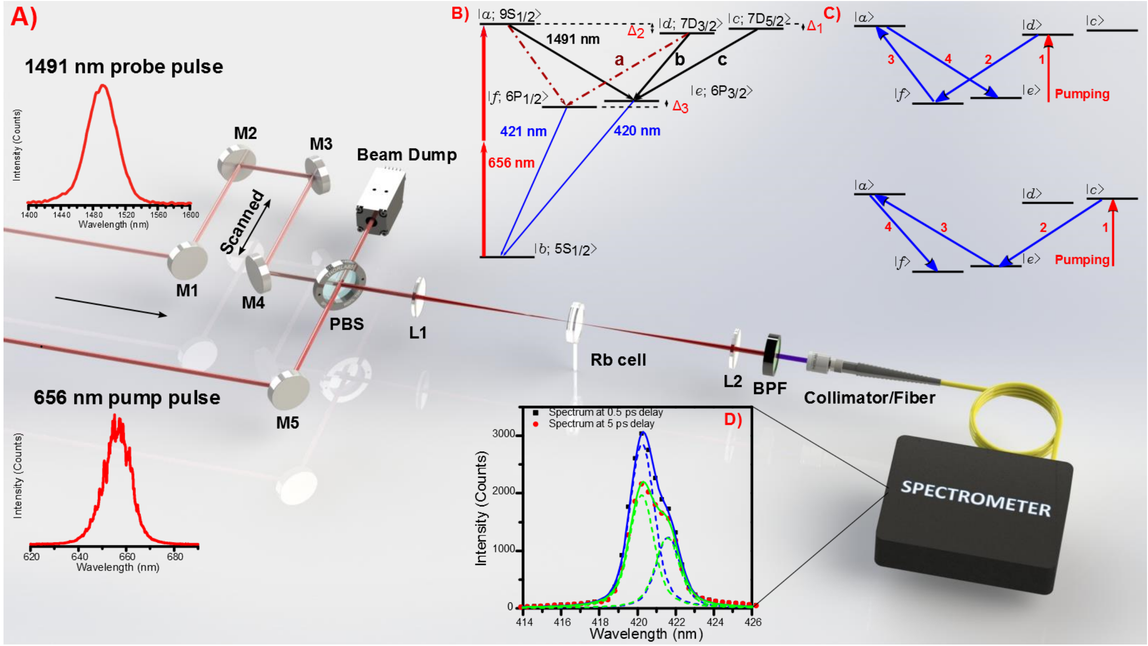

Figure 7.1: A) Experimental setup for observing the dual channel quantum beat. The pump (656 nm) and probe (1491 nm) laser pulses are collinearly combined and focused onto the Rb cell. Spectra of the input pulses are shown as they are generated from OPAs. M1-M5 are mirrors. M2 and M3 are set on translation stage. PBS is Pellicle beamsplitter. BPF is a band-pass filter centered at 420 nm with Full Width at Half Maximum (FWHM) of 10 nm. B) Simplified energy level diagram of $^{87}$Rb. Broadband pump pulse excites atoms from $5S$ to $9S$ and $7D$ levels; probe pulse couples $9S$ and $7D$ to $6P$ levels. C) Illustration of fourth order quantum paths which result in exchanging transition probabilities of two fine structure levels of $6P$ and beat pattern's envelope oscillation as discussed in the text. D) The spectra of the emission (black and red dots) measured at delay time of 0.5 ps and 5 ps between pump and probe pulses; Two distinguishable lines (dash lines) at wavelength 420 nm and 421 nm are fitted to the each set of data. The solid lines are sum of fitted Voigt profiles.

beam was sent through a pair of 90-degree cornered mirrors mounted on a digitally controlled translation stage (Newport) to precisely adjust the time delay between the pump and probe pulses. Both beams were collinearly combined by a pellicle beamsplitter (PBS) and were focused by a 200 mm focal length lens into the Rb cell. The number density of $^{87}$Rb atoms was estimated to be $1.3 \times 10^{15}$ cm$^{-3}$.

## 7.3 Results

The spectra of the coherent emission in the forward direction are shown in Figure 7.1 D). They were obtained with 2.0 mW average power and with 0.5 mW probe at different delay time between pump and probe pulses. As we scan the delay, we can see two peaks changing their intensities, thus we fit each spectrum to double peaks of Voigt profile. In the fitting, the two peaks share same Gaussian and Lorentzian widths, the positions and intensities of two peaks plus a constant baseline are independent parameters. Both spectra show fitted peaks at 420.2 nm and 421.6 nm which matches the exact values of the transitions [125] within the calibration accuracy (0.1 nm) of our spectrometer. The fitted spectra width of the Voigt profiles which is 1.5 nm, is not limited by the resolution (0.35 nm) of our spectrometer. Similar spectrum was taken at every step while the translation stage was scanned. To resolve the beat frequencies we use step size of 2 $\mu$m, which is equivalent to 0.0133 ps time delay; and to see large time scale decay curve, we choose 0.133 ps per step. Typical data of smaller step size are shown in Figure 7.2 a). These data are fitted to single exponential decay curve, and on average we get 16.14 ps decay time constant which is closely match to the delay time of SF signal (17.5 ps) in our previous work [126]. This match between the two time scale is reasonable, because Amplified Spontaneous Emission (ASE) rise from the population inversion between upper levels ($9S$ and $7D$ levels) and intermediate levels ($6P$, and $8P$, $7P$, $5P$) after the atoms being pumped.

If there is enough single pass gain (in another word, enough number of excited atoms within wavelength), the emission will evolve into SF [34, 111]. Coherence in the atomic ensemble will build up and after some delay time, a burst of pulse is emitted from the atoms. There are two time constant associate with SF process: collective damping time $\tau_r$ governs the SF pulse width, and delay time $\tau_D$ tell how long the system needs to evolve to emit a pulse. Our data suggests $\tau_D$ is a close measure of the decay time of the beating pattern. This argument rise even more naturally if we notice that many quantum beating experiments we mentioned earlier rely on the detection of the SF or Yoked SF [21] signal.

To extract a clear beat pattern, we performed a Fast Fourier Transform (FFT) filtering which filters decay and the dc offset components. The typical processed data is shown in Figure 7.2 b). To find the beat frequency, we fit the data to a damped sine function of the form $A_0 + A_1 e^{-t/\tau_0} \sin(2\pi f t)$. For 420 nm signal, we get an average beat frequency of 6.517 THz and for 421 nm signal, the average is 6.563 THz, with a difference of $46.4 \pm 2.8$ GHz between them. In literature, the calculated fine splitting of $7D$ of Rb is $45.18 \pm 0.3$ GHz [125]. If we look closely to the data points (Figure 7.2 c) and d)) we can see the effect of weak transition $b$ as shown in the energy diagram (Figure 7.1 B)). The 421 nm transition has only two quantum path from $9S$ and $7D$, the data (Figure 7.2 c)) fall closely to the fitted curve. But the 420 nm transition has three upstream quantum paths, even though transition b is relatively week compares to the other two, it still shows itself in the form which it make the data point (Figure 7.2 d)) falls off the fitted sine trace.

For the longer scan as shown in Figure 7.2 a), after the the Fourier filter, the beat pattern shows an overall envelope that has two features: a exponential decay and an oscillation with frequency of 46 GHz which matches to the fine structure splitting of $7D$. Figure 7.3 is the experimental results together with simulations showing both

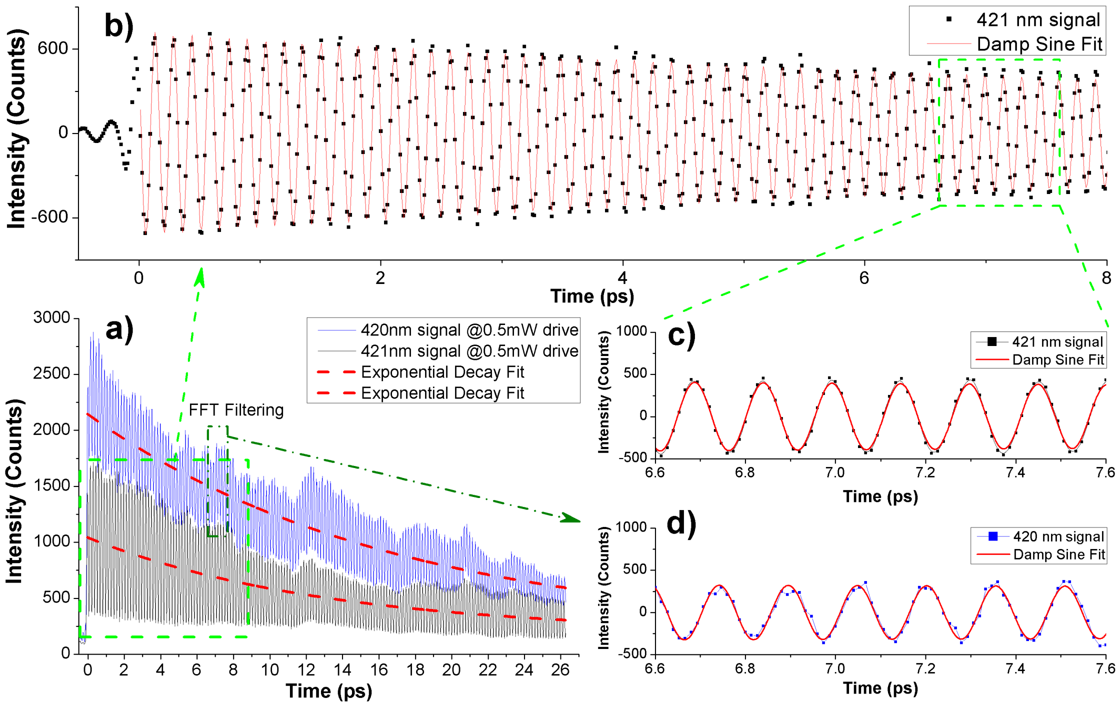

Figure 7.2: Experimental data with fitted functions. a) Full scanned data with time resolution of 0.0133 ps. Solid lines are the measured data and dashed red lines are corresponding fitted exponential decay curve. The fitted curves give an average decay time of 16.14 ps. b) Fast Fourier Transform (FFT) filtered 421 nm data (black dots) fitted to damped sine curve (red line) in 10 ps time scale. The DC offset has been dropped during data filtering. c) Zoomed in range as shown in the green dashed box. d) 420 nm data (blue dot and line )and fitted damped sine curve (red line) in same range time as c).

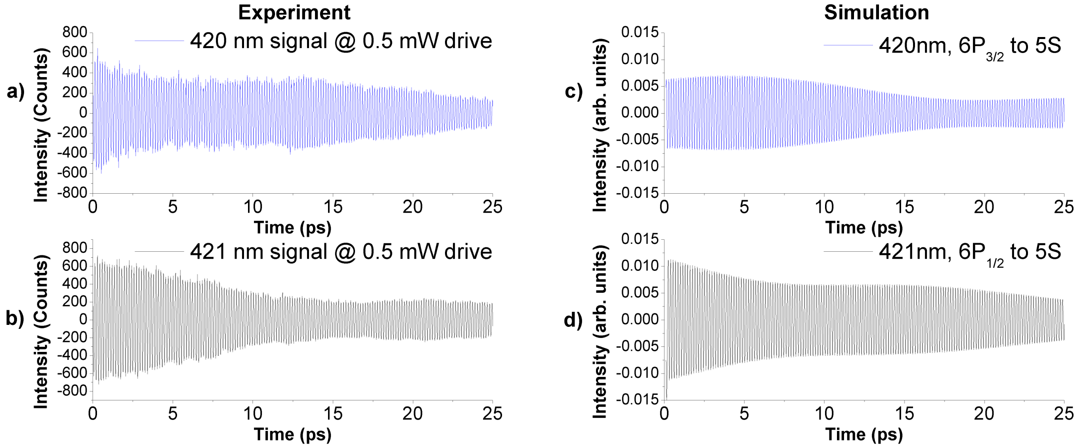

Figure 7.3: The envelopes of the beating on 420 nm and 421 nm signal. a) and b) are experimental data after a FFT high pass filtering to get rid of the DC and exponential decay components of the original data. c) and d) are simulations for the corresponding transitions of a) and b).

features. The exponential decay of this envelope is carried from the over all decay of the signals. The reason for the oscillation worth a little more discussion. Just by looking at the energy diagram (Figure 7.1), we can see that it is obvious for the signal of 420 nm to carry a frequency of 46 GHz since both levels of $7D$ are involved in its quantum path. But how can the 421 nm signal also carry this frequency? Is it from the coupling via $9S$? To find an answer to this question, we employ the following theoretical model.

## 7.4 Theoretical model

Effective atom-field interaction Hamiltonian can be written as [3, 127]

$$\begin{aligned}\mathscr{V}(t) = &-\hbar(\Omega_{eff}|a\rangle\langle b| + \Omega_{eff}\mathrm{e}^{-i\Delta_1 t}|c\rangle\langle b| + \Omega_{eff}\mathrm{e}^{-i\Delta_2 t}|d\rangle\langle b| + \Omega_{ae}|a\rangle\langle e| + \Omega_{af}\mathrm{e}^{i\Delta_3 t}|a\rangle\langle f| \\ &+ \Omega_{ce}\mathrm{e}^{-i\Delta_1 t}|c\rangle\langle e| + \Omega_{df}\mathrm{e}^{-i(\Delta_2-\Delta_3)t}|d\rangle\langle f| + \Omega_{de}\mathrm{e}^{-i\Delta_2 t}|d\rangle\langle e| + h.c),\end{aligned} \tag{7.1}$$

where we assume Gaussian pump pulses such that $\Omega_{eff} = \Omega_p^{(0)} \exp(-t^2/\alpha_p^2)$ is the effective Rabi frequency, $\Omega_{ij} = \Omega_{ij}^{(0)} \exp(-(t-\tau)^2/\alpha_c^2)$ is probe pulse Rabi frequency which couples $i$ and $j$ states. Because the pulse is very short compare to the time scale of SF, we essentially treat it in the delta function limit in our calculation. Notations we use for detunings are: $\Delta_1 = 40.99 \cdot 10^{12}\,\mathrm{s}^{-1}$ – the energy difference between $9S^{1/2}$ and $7D^{5/2}$, $\Delta_2 = 41.27 \cdot 10^{12}\,\mathrm{s}^{-1}$ – the energy difference between $9S^{1/2}$ and $7D^{3/2}$ and $\Delta_3 = 14.61 \cdot 10^{12}\,\mathrm{s}^{-1}$ – the energy difference between $6P^{3/2}$ and $6P^{1/2}$. Our goal is to find the probability of finding atom in the $|e\rangle$ and $|f\rangle$ states by using perturbation theory. The second order perturbation theory gives the explanation of beating of frequencies $\Delta_1/2\pi$ and $\Delta_2/2\pi$ but not the envelope beating in 421 nm signal. Therefore, we use perturbation theory up to fourth order term. The approximate solution can be written in the following form [†]

$$\begin{aligned} P_e &= |e_0 + e_1 \mathrm{e}^{i\Delta_1\tau} + e_2 \mathrm{e}^{i\Delta_2\tau}|^2, \\ P_f &= |f_0 + f_1 \mathrm{e}^{i\Delta_1\tau} + f_2 \mathrm{e}^{i\Delta_2\tau}|^2, \end{aligned} \tag{7.2}$$

where $e_j$ and $f_j$ $(j = 0, 1, 2)$ are constants. $e_2$ and $f_1$ are explicitly written as

$$\begin{aligned} e_2 = {} & \pi\alpha_p\alpha_c\Omega_{ed}^{(0)*}\Omega_p^{(0)} + \pi^2\alpha_p\alpha_c^3 \Big( \Omega_{ea}^{(0)*}\Omega_{ae}^{(0)}\Omega_{ed}^{(0)*}\Omega_p^{(0)} + \Omega_{ea}^{(0)*}\Omega_{af}^{(0)}\Omega_{fd}^{(0)*}\Omega_p^{(0)} \\ & + \Omega_{ec}^{(0)*}\Omega_{ce}^{(0)}\Omega_{ed}^{(0)*}\Omega_p^{(0)} + \Omega_{ed}^{(0)*}\Omega_{de}^{(0)}\Omega_{ed}^{(0)*}\Omega_p^{(0)} + \Omega_{ed}^{(0)*}\Omega_{df}^{(0)}\Omega_{fd}^{(0)*}\Omega_p^{(0)} \Big) \\ & + 3\pi^2\alpha_p^3\alpha_c\Omega_{ed}^{(0)*}\Omega_p^{(0)}\Omega_p^{(0)*}\Omega_p^{(0)}, \end{aligned} \tag{7.3}$$

$$f_1 = \pi^2\alpha_p\alpha_c^3 \left( \Omega_{fa}^{(0)*}\Omega_{ae}^{(0)}\Omega_{ec}^{(0)*}\Omega_p^{(0)} + \Omega_{fd}^{(0)*}\Omega_{de}^{(0)}\Omega_{ec}^{(0)*}\Omega_p^{(0)} \right), \tag{7.4}$$

where we change the indexes order in the complex conjugate of Rabi frequency such as $\left(\Omega_{ij}^{(0)}\right)^* = \Omega_{ji}^{(0)*}$. In this notation we can easily understand the terms in the Eqns.

---

[†] Details are found in Appendix B.

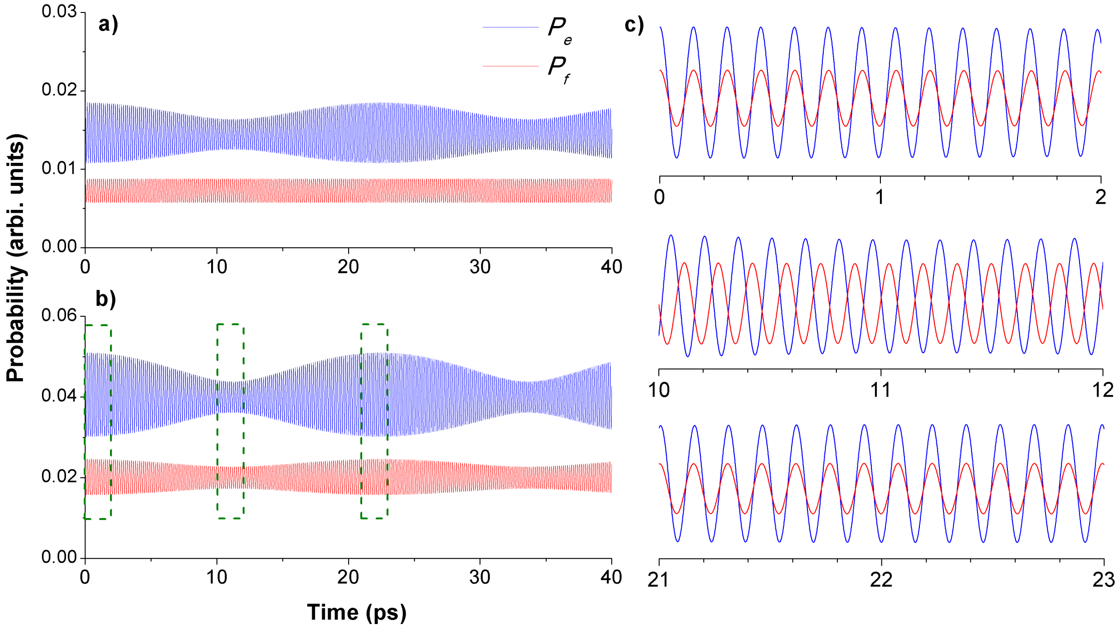

Figure 7.4: a) Probabilities of finding atoms on level $|e\rangle$ ($P_e$)and level $|f\rangle$ ($P_f$) plotted from analytical expressions keeps up to second order terms. b) Same probabilities plotted with expressions keeps up to fourth order terms. The envelope modulation of $P_e$ is effect of multi-photon (>3) interaction between levels $|c\rangle$ and $|f\rangle$ because single photon transition is forbidden. c) Probabilities zoomed into 2-ps windows, curves have been offset to show relative phase shift due to different beat frequencies of the signals. Parameters used for the plots are: $\alpha_p\Omega_p^{(0)} = 0.2$, $\alpha_c\Omega_{ae}^{(0)} = 0.6$, $\Omega_{af}^{(0)} = \Omega_{ae}^{(0)}/\sqrt{2}$, $\Omega_{ce}^{(0)} = 0.2\Omega_{ae}^{(0)}$, $\Omega_{df}^{(0)} = \Omega_{ce}^{(0)}\sqrt{5/9}$, $\Omega_{de}^{(0)} = \Omega_{ce}^{(0)}\sqrt{1/9}$. The relative transition dipole moments are estimated by sum rule [1].

(7.3) and (7.4). For example, the term $\Omega_{ea}^{(0)*}\Omega_{ae}^{(0)}\Omega_{ed}^{(0)*}\Omega_p^{(0)}$ associated with the fourth order process as pumping $\rightarrow |d\rangle \rightarrow |e\rangle \rightarrow |a\rangle \rightarrow |e\rangle$.

We plot the probability of finding atoms on level $|e\rangle$ ($P_e$) and level $|f\rangle$ ($P_f$) with parameters shown in Figure 7.4. Given conditions $e_1 \gg e_2$ and $f_1 \ll f_2$, one can verify that probabilities $P_e$ and $P_f$ oscillate at angular frequencies $\Delta_1$ and $\Delta_2$, respectively. Therefore, $e_1$ and $f_2$ terms in the Eqn. (7.2) give fast oscillations, as shown in smaller time windows in Figure 7.4 c). And because the frequencies are different, we can also see the relative phase of the beat oscillation shifts as the delay time increases. The expressions which keeps only up to second order terms is plotted in Figure 7.4 a), the envelope modulation of $P_f$ is absent; while the plot using expressions with fourth order terms clearly shows the modulation on $P_f$ and a larger modulation depth on $P_e$. We conclude that the $e_2$ and $f_1$ terms in Eqns. (7.3) and (7.4) cause the envelope modulation shown in the analytical results (Figure 7.4 b) and the experimental results (Figure 7.3). Furthermore, main reasons for the envelope oscillation are the fourth order processes coupled through $|a\rangle$ state ($9S_{1/2}$) as well as other processes in Eqns. (7.3) and (7.4). To see this more clearly, let us set $\Omega_{de}^{(0)} = 0$ because $|d\rangle \to |e\rangle$ transition intensity is 9 times less than that of $|c\rangle \to |e\rangle$ and 5 times less than $|d\rangle \to |f\rangle$ transition intensities. Then, Eqns. (7.3) and (7.4) become $e_2 = \pi^2 \alpha_p \alpha_c^3 \Omega_{ea}^{(0)*} \Omega_{af}^{(0)} \Omega_{fd}^{(0)*} \Omega_p^{(0)}$, $f_1 = \pi^2 \alpha_p \alpha_c^3 \Omega_{fa}^{(0)*} \Omega_{ae}^{(0)} \Omega_{ec}^{(0)*} \Omega_p^{(0)}$ which is symmetrically exchanging excitation probability from $|d\rangle$ ($|c\rangle$) to $|e\rangle$ ($|f\rangle$) (See Figure 7.1 D)). This fourth order process coupled through $|a\rangle$ state ($9S_{1/2}$) is the main reason for envelope oscillation in 421 nm signal and deeper modulation on 420 nm signal.

## 7.5 Conclusion

Because the beating data of 421 nm signal is much less disturbed by other quantum pathways, it is potentially a good candidate for the technic described in Ref. [121] to characterize dipole-dipole interactions. This technic requires a long time scan ($\sim$ 100 ps) in order to get enough FT spectra resolution. Our experimental data shows good sign for longer scan range despite the decay of signal. As for weak atomic excitation, both theoretical [128] and experimental [129] works have shown that the population on the excited states can survive hundreds of picoseconds.

It is also possible to detect the beat pattern by monitoring the transmission of the infrared probe [123]. Control of the beat pattern has been studied in our group by shifting the pump wavelength [107] or adding a control pulse [130]. In our case, shift the pump beam central wavelength could possibly tune the amplitudes and initial phase of the beat pattern.

In summary, we investigated the coherent emission at 420 nm and 421 nm in $^{87}$Rb. We observed different quantum beats frequencies on these two emissions when we scan the delay between pump and probe pulses. The profiles were measured and a numerical simulation was compared with the experimental results. Our results suggest the SF delay time is a good measure of the exponential decay of the beating envelope. With the help of perturbation method, a fourth order (five-photon) process was identified in presence of the beat envelope of the 421 nm emission.

# 8. CONCLUSION

While we can use various tools to increase signal in the laboratory, such as resonant Raman scattering and SERS, the strategy to boost standoff detection favors seeking laser-like directional coherent beam in the backward direction. This kind of beams has been demonstrated, but the characters and physical mechanism of them deserve more investigation.

We first showed how we can use resonant Raman scattering to probe the change of the density of dimer molecules in alkali-metal vapors and further control of the density via photodesorption process by using an ultralow-power diode-laser radiation. We also demonstrated an signal enhancement factor of $10^6$ from SERS of rhodamine 6G on template-embedded gold nanorods.

With some help of quantum coherence in an atomic system, a burst of directional emission can be observed in both forward and backward direction. The collective phenomena including superradiant emission (superfluorescence/superradiance and Yoked superfluorescence) offer many challenges and opportunities.

We study backward cooperative emissions from a dense sodium atomic vapor. The backward SF emissions, both on the $4S_{1/2} - 3P_{3/2}$ and $4S_{1/2} - 3P_{1/2}$ transitions decouple from each other due to the large difference in their spontaneous decay rates which dictate the SF delay time of each transition. This enables us to measure the absolute (rather than relative) time delay and its fluctuations (free of any possible external noise).

We also investigate cooperative emission from a rubidium vapor, and demonstrate a controlled transition from YSF to three-photon-induced SR by driving the medium with co-propagating ultrashort laser pulses. The SR signal intensity is more than 30 times of that of YSF. This result gives some insight to strategies to improve efficiency of mirrorless lasers and SR light sources.

While transition from YSF to SR can be controlled by changing the pulse energy in the probe pulse, from which the tipping angle can be experimentally determined, more interesting results are also obtained when the delay between the pump and probe pulses is scanned. Because of the signal enhancement, quantum beat from coupled dual pathways can be observed, which turnout to be a useful tool to help us reveal and understand dipole-dipole interaction and multi-photon (>5) interaction in the system we study.

Our present works study strategies to enhance optical signals in the lab-based detection and remote sensing. We hope these works can boost the interest of quantum coherence effects and cooperative emission in the optical society.

# REFERENCES

[1] G. K. Woodgate. *Elementary atomic structure.* Clarendon Press, Oxford, 2nd edition, 1980.

[2] Ch. Eisele, A. Yu. Nevsky, and S. Schiller. Laboratory test of the isotropy of light propagation at the $10^{-17}$ level. *Phys. Rev. Lett.*, 103:090401, Aug 2009.

[3] Marlan O. Scully and M. Suhail Zubairy. *Quantum Optics.* Cambridge University Press, Cambridge ; New York, 1997.

[4] Herman A. Szymanski. *Raman Spectroscopy : Theory and Practice.* Boston, MA : Springer US, 1967., 1967.

[5] Katrin Kneipp, Martin Moskovits, and Harald Kneipp. *Surface-enhanced Raman scattering : physics and applications.* Topics in applied physics: v. 103. Berlin ; New York : Springer,, 2006.

[6] Eric C. Le Ru and Pablo G. Etchegoin. *Principles of surface-enhanced Raman spectroscopy : and related plasmonic effects. 1st ed.* Amsterdam ; Boston : Elsevier, 2009. 1st ed., 2009.

[7] R. Zhang, Y. Zhang, Z. C. Dong, S. Jiang, C. Zhang, L. G. Chen, L. Zhang, Y. Liao, J. Aizpurua, Y. Luo, J. L. Yang, and J. G. Hou. Chemical mapping of a single molecule by plasmon-enhanced raman scattering. *Nature*, 498(7452):82–86, 2013.

[8] Wolfgang Demtrder. *Laser Spectroscopy.* Dordrecht : Springer-Verlag, 2008.

[9] Dmitry Pestov, Robert K. Murawski, Gombojav O. Ariunbold, Xi Wang, Miaochan Zhi, Alexei V. Sokolov, Vladimir A. Sautenkov, Yuri V. Rostovtsev, Arthur Dogariu, Yu Huang, and Marlan O. Scully. Optimizing the laser-pulse

configuration for coherent raman spectroscopy. *Science*, 316(5822):265–268, 2007.

[10] Wolfgang Steinbrecht, Karl W. Rothe, and Herbert Walther. Lidar setup for daytime and nighttime probing of stratospheric ozone and measurements in polar and equatorial regions. *Applied Optics*, 28(17):3616–3624, 1989.

[11] Scott E. Bisson, John E. M. Goldsmith, and Mark G. Mitchell. Narrow-band, narrow-field-of-view raman lidar with combined day and night capability for tropospheric water-vapor profile measurements. *Applied Optics*, 38(9):1841–1849, 1999.

[12] V. Kocharovsky, S. Cameron, K. Lehmann, R. Lucht, R. Miles, Y. Rostovtsev, W. Warren, G. R. Welch, and M. O. Scully. Gain-swept superradiance applied to the stand-off detection of trace impurities in the atmosphere. *Proceedings of the National Academy of Sciences*, 102(22):7806–7811, 2005.

[13] Philip R. Hemmer, Richard B. Miles, Pavel Polynkin, Torsten Siebert, Alexei V. Sokolov, Phillip Sprangle, and Marlan O. Scully. Standoff spectroscopy via remote generation of a backward-propagating laser beam. *Proceedings of the National Academy of Sciences*, 108(8):3130–3134, 2011.

[14] R. H. Dicke. Coherence in spontaneous radiation processes. *Physical Review*, 93(1):99–110, 1954.

[15] Nicholas E. Rehler and Joseph H. Eberly. Superradiance. *Physical Review A*, 3(5):1735–1751, 1971.

[16] R. Bonifacio and L. A. Lugiato. Cooperative radiation processes in two-level systems: Superfluorescence. *Physical Review A*, 11(5):1507–1521, 1975.

[17] J. C. MacGillivray and M. S. Feld. Theory of superradiance in an extended, optically thick medium. *Physical Review A*, 14(3):1169–1189, 1976.

[18] Arthur Dogariu, James B. Michael, Marlan O. Scully, and Richard B. Miles. High-gain backward lasing in air. *Science*, 331(6016):442–445, 2011.

[19] Andrew J. Traverso, Rodrigo Sanchez-Gonzalez, Luqi Yuan, Kai Wang, D-mitri V. Voronine, Aleksei M. Zheltikov, Yuri Rostovtsev, Vladimir A. Sautenkov, Alexei V. Sokolov, Simon W. North, and Marlan O. Scully. Coherence brightened laser source for atmospheric remote sensing. *Proceedings of the National Academy of Sciences*, 109(38):15185–15190, 2012.

[20] Alexandre Laurain, Maik Scheller, and Pavel Polynkin. Low-threshold bidirectional air lasing. *Physical Review Letters*, 113(25):253901, 2014.

[21] J. H. Brownell, X. Lu, and S. R. Hartmann. Yoked superfluorescence. *Physical Review Letters*, 75(18):3265–3268, 1995.

[22] E. B. Alexandrov, M. V. Balabas, D. Budker, D. English, D. F. Kimball, C. H. Li, and V. V. Yashchuk. Light-induced desorption of alkali-metal atoms from paraffin coating. *Physical Review A*, 66(4):042903, 2002.

[23] M. T. Graf, D. F. Kimball, S. M. Rochester, K. Kerner, C. Wong, D. Budker, E. B. Alexandrov, M. V. Balabas, and V. V. Yashchuk. Relaxation of atomic polarization in paraffin-coated cesium vapor cells. *Physical Review A*, 72(2):023401, 2005.

[24] T. Karaulanov, M. T. Graf, D. English, S. M. Rochester, Y. J. Rosen, K. T-sigutkin, D. Budker, E. B. Alexandrov, M. V. Balabas, D. F. Jackson Kimball, F. A. Narducci, S. Pustelny, and V. V. Yashchuk. Controlling atomic vapor

density in paraffin-coated cells using light-induced atomic desorption. *Physical Review A*, 79(1):012902, 2009.

[25] V. M. Acosta, A. Jarmola, D. Windes, E. Corsini, M. P. Ledbetter, T. Karaulanov, M. Auzinsh, S. A. Rangwala, D. F. Jackson Kimball, and D. Budker. Rubidium dimers in paraffin-coated cells. *New Journal of Physics*, 12(8):083054, 2010.

[26] Murray Sargent, Marlan O. Scully, and Willis E. Lamb. *Laser physics*. Reading, Mass. : Addison-Wesley Pub. Co., Advanced Book Program, 1974.

[27] Gerhard Herzberg and Klaus-Peter Huber. *Molecular spectra and molecular structure, I. Spectra of diatomic molecules*. New York : Van Nostrand, [©1945-1966; v. 1, ©1950], 1950.

[28] C. J. Foot. *Atomic physics*. Oxford master series in physics. Oxford ; New York : Oxford University Press, 2005.

[29] Alfons Weber. *Raman Spectroscopy of Gases and Liquids*. Topics in Current Physics: 11. Berlin, Heidelberg : Springer Berlin Heidelberg, 1979., 1979.

[30] Christopher J. Orendorff, Anand Gole, Tapan K. Sau, and Catherine J. Murphy. Surface-enhanced raman spectroscopy of self-assembled monolayers: Sandwich architecture and nanoparticle shape dependence. *Analytical Chemistry*, 77(10):3261–3266, 2005.

[31] Yuling Wang, Hongjun Chen, Shaojun Dong, and Erkang Wang. Surface enhanced raman scattering of p-aminothiophenol self-assembled monolayers in sandwich structure fabricated on glass. *The Journal of Chemical Physics*, 124(7):074709, 2006.

[32] Marlan O. Scully, Edward S. Fry, C. H. Raymond Ooi, and Krzysztof Wódkiewicz. Directed spontaneous emission from an extended ensemble of $n$ atoms: Timing is everything. *Physical Review Letters*, 96(1):010501, 2006.

[33] Marlan O. Scully. Single photon subradiance: Quantum control of spontaneous emission and ultrafast readout. *Physical Review Letters*, 115(24):243602, 2015.

[34] Luqi Yuan, Brett H. Hokr, Andrew J. Traverso, Dmitri V. Voronine, Yuri Rostovtsev, Alexei V. Sokolov, and Marlan O. Scully. Theoretical analysis of the coherence-brightened laser in air. *Physical Review A*, 87(2):023826, 2013.

[35] L. Essen and J. V. L. Parry. An atomic standard of frequency and time interval: A caesium resonator. *Nature*, 176(4476):280–282, 1955. 10.1038/176280a0.

[36] N. F. Ramsey. History of atomic clocks. *Journal of Research of the National Bureau of Standards*, 88(5):20, 1983.

[37] R. Frisch. Experimenteller nachweis des einsteinschen strahlungsrückstoßes. *Zeitschrift für Physik*, 86(1):42–48, 1933.

[38] Jean Brossel, Alfred Kastler, and Jacques Winter. Gréation optique d'une inégalité de population entre les sous-niveaux zeeman de l'état fondamental des atomes. *J. Phys. Radium*, 13(12):668, 1952.

[39] W. B. Hawkins and R. H. Dicke. The polarization of sodium atoms. *Physical Review*, 91(4):1008–1009, 1953.

[40] P. Kusch, S. Millman, and I. I. Rabi. The radiofrequency spectra of atoms hyperfine structure and zeeman effect in the ground state of $\mathrm{Li}^6$, $\mathrm{Li}^7$, $\mathrm{K}^{39}$ and $\mathrm{K}^{41}$. *Physical Review*, 57(9):765–780, 1940.

[41] G. Alzetta, A. Gozzini, L. Moi, and G. Orriols. An experimental method for the observation of r.f. transitions and laser beat resonances in oriented na vapour. *Il Nuovo Cimento B*, 36(1):5–20, 1976.

[42] E. L. Raab, M. Prentiss, Alex Cable, Steven Chu, and D. E. Pritchard. Trapping of neutral sodium atoms with radiation pressure. *Physical Review Letters*, 59(23):2631–2634, 1987.

[43] M. H. Anderson, J. R. Ensher, M. R. Matthews, C. E. Wieman, and E. A. Cornell. Observation of bose-einstein condensation in a dilute atomic vapor. *Science*, 269(5221):198–201, 1995.

[44] Andrei Nikolaevich Nesmeianov. *Vapour pressure of the elements.* New York : Academic Press, 1963.

[45] M. Lintz and M. A. Bouchiat. Dimer destruction in a Cs vapor by a laser close to atomic resonance. *Physical Review Letters*, 80(12):2570–2573, 1998.

[46] T. Ban, D. Aumiler, and G. Pichler. Rubidium dimer destruction by a diode laser. *Physical Review A*, 71(2):022711, 2005.

[47] D.H. Sarkisyan, A.S. Sarkisyan, and A.K. Yalanusyan. Thermal dissociation of cesium dimers. *Applied Physics B*, 66(2):241–244, 1998.

[48] A. Gozzini, F. Mango, J. H. Xu, G. Alzetta, F. Maccarrone, and R. A. Bernheim. Light-induced ejection of alkali atoms in polysiloxane coated cells. *Il Nuovo Cimento D*, 15(5):709–722, 1993.

[49] E. Mariotti, S. Atutov, M. Meucci, P. Bicchi, C. Marinelli, and L. Moi. Dynamics of rubidium light-induced atom desorption (LIAD). *Chemical Physics*, 187(1-2):111–115, 1994.

[50] R. Gupta, W. Happer, J. Wagner, and E. Wennmyr. Absorption studies of $Cs_2$ and $Rb_2$ molecular bands in the visible and near visible. *The Journal of Chemical Physics*, 68(3):799–803, 1978.

[51] S. Mukamel. *Principles of nonlinear optical spectroscopy.* Oxford series in optical and imaging sciences: 6. New York : Oxford University Press, 1995.

[52] Philip M. Morse. Diatomic molecules according to the wave mechanics. II. vibrational levels. *Physical Review*, 34(1):57–64, 1929.

[53] Derek Steele, Ellis R. Lippincott, and Joseph T. Vanderslice. Comparative study of empirical internuclear potential functions. *Reviews of Modern Physics*, 34(2):239–251, 1962.

[54] Luqi Yuan, Gombojav O. Ariunbold, Robert K. Murawski, Dmitry Pestov, X-i Wang, Anil K. Patnaik, Vladimir A. Sautenkov, Alexei V. Sokolov, Yuri V. Rostovtsev, and Marlan O. Scully. Femtosecond wave-packet dynamics in cesium dimers studied through controlled stimulated emission. *Physical Review A*, 81(5):053405, 2010.

[55] N. Bloembergen. *Nonlinear spectroscopy : Proceedings of the International school of Physics "Enrico Fermi", Course LXIV.* Amsterdam ; New York : North-Holland Pub. Co. ; Bologna, Italy : Societa Italiana Di Fisica, 1977.

[56] Martin Moskovits. Surface-enhanced spectroscopy. *Reviews of Modern Physics*, 57(3):783–826, 1985.

[57] Hongxing Xu, Erik J. Bjerneld, Mikael Käll, and Lars Börjesson. Spectroscopy of single hemoglobin molecules by surface enhanced raman scattering. *Physical Review Letters*, 83(21):4357–4360, 1999.

[58] Alan Campion and Patanjali Kambhampati. Surface-enhanced raman scattering. *Chemical Society Reviews*, 27(4):241–250, 1998.

[59] Martin Moskovits. Surface-enhanced raman spectroscopy: a brief retrospective. *Journal of Raman Spectroscopy*, 36(6-7):485–496, 2005.

[60] Keith T. Carron, Gi Xue, and Mary L. Lewis. A surface enhanced raman spectroscopy study of the corrosion-inhibiting properties of benzimidazole and benzotriazole on copper. *Langmuir*, 7(1):2–4, 1991.

[61] Shuming Nie and Steven R. Emory. Probing single molecules and single nanoparticles by surface-enhanced raman scattering. *Science*, 275(5303):1102–1106, 1997.

[62] Babak Nikoobakht and Mostafa A. El-Sayed. Surface-enhanced raman scattering studies on aggregated gold nanorods. *The Journal of Physical Chemistry A*, 107(18):3372–3378, 2003.

[63] Andrea Tao, Franklin Kim, Christian Hess, Joshua Goldberger, Rongrui He, Yugang Sun, Younan Xia, and Peidong Yang. Langmuir-blodgett silver nanowire monolayers for molecular sensing using surface-enhanced raman spectroscopy. *Nano Letters*, 3(9):1229–1233, 2003.

[64] Christy L. Haynes and Richard P. Van Duyne. Nanosphere lithography: A versatile nanofabrication tool for studies of size-dependent nanoparticle optics. *The Journal of Physical Chemistry B*, 105(24):5599–5611, 2001.

[65] N. Félidj, J. Aubard, G. Lévi, J. R. Krenn, A. Hohenau, G. Schider, A. Leitner, and F. R. Aussenegg. Optimized surface-enhanced raman scattering on gold nanoparticle arrays. *Applied Physics Letters*, 82(18):3095–3097, 2003.

[66] H. H. Wang, C. Y. Liu, S. B. Wu, N. W. Liu, C. Y. Peng, T. H. Chan, C. F. Hsu, J. K. Wang, and Y. L. Wang. Highly raman-enhancing substrates based on silver nanoparticle arrays with tunable sub-10 nm gaps. *Advanced Materials*, 18(4):491–495, 2006.

[67] Dentcho A. Genov, Andrey K. Sarychev, Vladimir M. Shalaev, and Alexander Wei. Resonant field enhancements from metal nanoparticle arrays. *Nano Letters*, 4(1):153–158, 2004.

[68] Christy L. Haynes and Richard P. Van Duyne. Plasmon-sampled surface-enhanced raman excitation spectroscopy. *The Journal of Physical Chemistry B*, 107(30):7426–7433, 2003.

[69] Xiangtao Bai, Yanan Gao, and Liqiang Zheng. Galvanic replacement mediated growth of dendritic gold nanostructures with a three-fold symmetry and their applications to SERS. *CrystEngComm*, 13(10):3562–3568, 2011.

[70] Adam D. McFarland, Matthew A. Young, Jon A. Dieringer, and Richard P. Van Duyne. Wavelength-scanned surface-enhanced raman excitation spectroscopy. *The Journal of Physical Chemistry B*, 109(22):11279–11285, 2005.

[71] Qing Liao, Cheng Mu, Dong-Sheng Xu, Xi-Cheng Ai, Jian-Nian Yao, and Jian-Ping Zhang. Gold nanorod arrays with good reproducibility for high-performance surface-enhanced Raman scattering. *Langmuir*, 25(8):4708–4714, 2009.

[72] F. J. García de Abajo and A. Howie. Retarded field calculation of electron energy loss in inhomogeneous dielectrics. *Physical Review B*, 65(11):115418, 2002.

[73] F. J. García de Abajo and A. Howie. Relativistic electron energy loss and electron-induced photon emission in inhomogeneous dielectrics. *Physical Review Letters*, 80(23):5180–5183, 1998.

[74] Seung Joon Lee, Zhiqiang Guan, Hongxing Xu, and Martin Moskovits. Surface-enhanced raman spectroscopy and nanogeometry: The plasmonic origin of SERS. *The Journal of Physical Chemistry C*, 111(49):17985–17988, 2007.

[75] Dmitri V. Voronine, Alexander M. Sinyukov, Xia Hua, Kai Wang, Pankaj K. Jha, Elango Munusamy, Steven E. Wheeler, George Welch, Alexei V. Sokolov, and Marlan O. Scully. Time-resolved surface-enhanced coherent sensing of nanoscale molecular complexes. *Scientific Reports*, 2:891, 2012.

[76] J. Kasparian, M. Rodriguez, G. Méjean, J. Yu, E. Salmon, H. Wille, R. Bourayou, S. Frey, Y.-B. André, A. Mysyrowicz, R. Sauerbrey, J.-P. Wolf, and L. Wöste. White-light filaments for atmospheric analysis. *Science*, 301(5629):61–64, 2003.

[77] A. Couairon and A. Mysyrowicz. Femtosecond filamentation in transparent media. *Physics Reports*, 441(2-4):47–189, 2007.

[78] Alexander I. Lvovsky. *Omnidirectional superfluorescence transients*. PhD thesis, Columbia University, 1998.

[79] Gombojav O. Ariunbold, Vladimir A. Sautenkov, Yuri V. Rostovtsev, and Marlan O. Scully. Ultrafast laser control of backward superfluorescence towards standoff sensing. *Applied Physics Letters*, 104(2):021114, 2014.

[80] N. Ageorges and J. C. Dainty. *Laser Guide Star Adaptive Optics for Astronomy*. NATO ASI series. Series C, Mathematical and physical sciences: 551. Dordrecht : Springer Netherlands, 2000.

[81] Jens Biegert and Jean-Claude Diels. Feasibility study to create a polychromatic guidestar in atomic sodium. *Physical Review A*, 67(4):043403, 2003.

[82] Renaud Foy, Pierre Éric, Jérôme Eysseric, Françoise Foy, Thierry Fusco, Julien Girard, Auguste Le Van Suu, Sandrine Perruchot, Pierre Richaud, Yoann Richaud, Xavier Rondeau, Michel Tallon, Éric Thiébaut, and Michel Boër. The polychromatic laser guide star for tilt measurement: progress report of the demonstrator at observatoire de haute provence. *Proc. SPIE*, 6691:66910R–66910R–8, 2007. 10.1117/12.733997.

[83] Jean-Paul Pique, Ioana Cristina Moldovan, and Vincent Fesquet. Concept for polychromatic laser guide stars: one-photon excitation of the $4P_{3/2}$ level of a sodium atom. *Journal of the Optical Society of America A*, 23(11):2817–2828, 2006.

[84] Hugues Guillet de Chatellus, Jean-Paul Pique, and Ioana Cristina Moldovan. Return flux budget of polychromatic laser guide stars. *Journal of the Optical Society of America A*, 25(2):400–415, 2008.

[85] Dennis Hite, Mark Deebel, Erik Thoreson, Casey Lengacher, Richard E. Miers, and Mark F. Masters. Construction of a heat pipe oven on a small budget. *American Journal of Physics*, 65(10):1017–1022, 1997.

[86] T. T. Grove, W. A. Hockensmith, N. Cheviron, W. Grieser, R. Dill, and M. F. Masters. Construction of an inexpensive copper heat-pipe oven. *European Journal of Physics*, 30(6):1229, 2009.

[87] Z Ficek, R Tanas, and S Keilich. Cooperative effects in the spontaneous e-mission from two non-identical atoms. *Optica Acta: International Journal of Optics*, 33(9):1149–1160, 1986.

[88] Gombojav O. Ariunbold, Michael M. Kash, Vladimir A. Sautenkov, Hebin Li, Yuri V. Rostovtsev, George R. Welch, and Marlan O. Scully. Observation of picosecond superfluorescent pulses in rubidium atomic vapor pumped by 100-fs laser pulses. *Physical Review A*, 82(4):043421, 2010.

[89] Gombojav O. Ariunbold, Vladimir A. Sautenkov, and Marlan O. Scully. Quantum fluctuations of superfluorescence delay observed with ultrashort optical excitations. *Physics Letters A*, 376(4):335–338, 2012.

[90] Q. H. F. Vrehen and J. J. der Weduwe. Quantum fluctuations in superfluorescence delay times. *Physical Review A*, 24(5):2857–2860, 1981.

[91] V. Degiorgio. Statistical properties of superradiant pulses. *Optics Communications*, 2(8):362–364, 1971.

[92] L. Yuan, A. A. Lanin, P. K. Jha, A. J. Traverso, D. V. Voronine, K. E. Dorfman, A. B. Fedotov, G. R. Welch, A. V. Sokolov, A. M. Zheltikov, and M. O. Scully. Coherent Raman umklappscattering. *Laser Physics Letters*, 8(10):736, 2011.

[93] P. N. Malevich, D. Kartashov, Z. Pu, S. Ališauskas, A. Pugžlys, A. Baltuška, L. Giniūnas, R. Danielius, A. A. Lanin, A. M. Zheltikov, M. Marangoni, and G. Cerullo. Ultrafast-laser-induced backward stimulated Raman scattering for tracing atmospheric gases. *Optics Express*, 20(17):18784–18794, 2012.

[94] F. A. Hopf, P. Meystre, M. O. Scully, and John F. Seely. Coherence brightening and laser lethargy in x-ray laser amplifiers. *Physical Review Letters*, 35(8):511–513, 1975.

[95] Anatoly A. Svidzinsky, Luqi Yuan, and Marlan O. Scully. Quantum amplification by superradiant emission of radiation. *Physical Review X*, 3(4):041001, 2013.

[96] M. Gross and S. Haroche. Superradiance: An essay on the theory of collective spontaneous emission. *Physics Reports*, 93(5):301–396, 1982.

[97] Marlan O. Scully and Anatoly A. Svidzinsky. The super of superradiance. *Science*, 325(5947):1510–1511, 2009.

[98] N. Skribanowitz, I. P. Herman, J. C. MacGillivray, and M. S. Feld. Observation of dicke superradiance in optically pumped HF gas. *Physical Review Letters*, 30(8):309–312, 1973.

[99] J. C. MacGillivray and M. S. Feld. Limits of superradiance as a process for achieving short pulses of high energy. *Physical Review A*, 23(3):1334–1349, 1981.

[100] R. Bonifacio and L. A. Lugiato. Cooperative radiation processes in two-level systems: Superfluorescence. II. *Physical Review A*, 12(2):587–598, 1975.

[101] Mitsuru Nagasono, James R. Harries, Hiroshi Iwayama, Tadashi Togashi, Kensuke Tono, Makina Yabashi, Yasunori Senba, Haruhiko Ohashi, Tetsuya Ishikawa, and Eiji Shigemasa. Observation of free-electron-laser-induced collective spontaneous emission (superfluorescence). *Physical Review Letters*, 107(19):193603, 2011.

[102] G. Timothy Noe Ii, Ji-Hee Kim, Jinho Lee, Yongrui Wang, Aleksander K. Wojcik, Stephen A. McGill, David H. Reitze, Alexey A. Belyanin, and Junichiro Kono. Giant superfluorescent bursts from a semiconductor magneto-plasma. *Nature Physics*, 8(3):219–224, 2012. 10.1038/nphys2207.

[103] K. Ikeda, J. Okada, and M. Matsuoka. Theory of cooperative cascade emission. I. Linear stochastic theory. *Journal of the Physical Society of Japan*, 48:1636, May 1980.

[104] Luqi Yuan and Anatoly A. Svidzinsky. Gain without population inversion in a yoked superfluorescence scheme. *Physical Review A*, 85(3):033836, 2012.

[105] W. R. Garrett. Forward gain suppression of optically pumped stimulated emissions due to self-induced wave-mixing interference during a pump pulse. *Physical Review Letters*, 70(26):4059–4062, 1993.

[106] A. I. Lvovsky, S. R. Hartmann, and F. Moshary. Superfluorescence-stimulated photon echoes. *Physical Review Letters*, 89(26):263602, 2002.

[107] Gombojav O. Ariunbold, Michael M. Kash, Vladimir A. Sautenkov, Hebin Li, Yuri V. Rostovtsev, George R. Welch, and Marlan O. Scully. Observation of picosecond UV pulses produced by coherent scattering of IR femtosecond pulses in atomic rubidium vapor. *J. Opt. Soc. Am. B*, 28(3):515–520, 2011.

[108] Gombojav O. Ariunbold, Wenlong Yang, Alexei V. Sokolov, Vladimir A. Sautenkov, and Marlan O. Scully. Picosecond superradiance in a three-photon resonant medium. *Physical Review A*, 85(2):023424, 2012.

[109] Gombojav O. Ariunbold, Vladimir A. Sautenkov, and Marlan O. Scully. Temporal coherent control of superfluorescent pulses. *Opt. Lett.*, 37(12):2400–2402, 2012.

[110] Michelle S. Malcuit, Jeffery J. Maki, David J. Simkin, and Robert W. Boyd. Transition from superfluorescence to amplified spontaneous emission. *Physical Review Letters*, 59(11):1189–1192, 1987.

[111] Jeffery J. Maki, Michelle S. Malcuit, Michael G. Raymer, Robert W. Boyd, and Peter D. Drummond. Influence of collisional dephasing processes on superfluorescence. *Physical Review A*, 40(9):5135–5142, 1989.

[112] P. K. Jha, A. A. Svidzinsky, and M. O. Scully. Coherence enhanced transient lasing in XUV regime. *Laser Physics Letters*, 9(5):368, 2012.

[113] P. K. Jha. Using quantum coherence to enhance gain in atomic physics. *Coherent Optical Phenomena*, 1:25–41, 2013.

[114] Konstantin E. Dorfman, Pankaj K. Jha, Dmitri V. Voronine, Patrice Genevet, Federico Capasso, and Marlan O. Scully. Quantum-coherence-enhanced surface plasmon amplification by stimulated emission of radiation. *Physical Review Letters*, 111(4):043601, 2013.

[115] Alexander Akulshin, Dmitry Budker, and Russell McLean. Directional infrared emission resulting from cascade population inversion and four-wave mixing in rb vapor. *Optics Letters*, 39(4):845–848, 2014.

[116] J. F. Sell, M. A. Gearba, B. D. DePaola, and R. J. Knize. Collimated blue and infrared beams generated by two-photon excitation in rb vapor. *Optics Letters*, 39(3):528–531, 2014.

[117] R. Friedberg and S. R. Hartmann. Superradiant lifetime: Its definitions and relation to absorption length. *Physical Review A*, 13(1):495–496, 1976.

[118] D. Polder, M. F. H. Schuurmans, and Q. H. F. Vrehen. Superfluorescence: Quantum-mechanical derivation of maxwell-bloch description with fluctuating field source. *Physical Review A*, 19(3):1192–1203, 1979.

[119] Hebin Li, Alan D. Bristow, Mark E. Siemens, Galan Moody, and Steven T. Cundiff. Unraveling quantum pathways using optical 3D fourier-transform spectroscopy. *Nature Communication*, 4:1390, 2013. 10.1038/ncomms2405.

[120] Daan Brinks, Richard Hildner, Erik M. H. P. van Dijk, Fernando D. Stefani, Jana B. Nieder, Jordi Hernando, and Niek F. van Hulst. Ultrafast dynamics

of single molecules. *Chemical Society Reviews*, 43(8):2476–2491, 2014.

[121] F. Shen, J. Gao, A. A. Senin, C. J. Zhu, J. R. Allen, Z. H. Lu, Y. Xiao, and J. G. Eden. Many-body dipole-dipole interactions between excited Rb atoms probed by wave packets and parametric four-wave mixing. *Physical Review Letters*, 99(14):143201, 2007.

[122] Valérie Blanchet, Céline Nicole, Mohamed-Aziz Bouchene, and Bertrand Girard. Temporal coherent control in two-photon transitions: From optical interferences to quantum interferences. *Physical Review Letters*, 78(14):2716–2719, 1997.

[123] C. J. Zhu, Y. Xiao, A. A. Senin, J. Gao, J. G. Eden, T. S. Varzhapetyan, and D. H. Sarkisyan. Quantum beating in Rb at 18.3 THz ($608\,\mathrm{cm}^{-1}$) detected by parametric six-wave mixing and sum-frequency generation in $\mathrm{LiIO_3}$. *Physical Review A*, 75(5):053405, 2007.

[124] Brian Ricconi. *Quantum beat observations in rubidium vapor.* Dissertation, University of Illinois at Urbana-Champaign, 2012.

[125] J. E. Sansonetti. Wavelengths, transition probabilities, and energy levels for the spectra of rubidium (Rb I through Rb XXXVII). *Journal of Physical and Chemical Reference Data*, 35(1):301–421, 2006.

[126] Zhenhuan Yi, Pankaj K. Jha, Luqi Yuan, Dmitri V. Voronine, Gombojav O. Ariunbold, Alexander M. Sinyukov, Ziyun Di, Vladmir A. Sautenkov, Yuri V. Rostovtsev, and Alexei V. Sokolov. Observing the transition from yoked superfluorescence to superradiance. *Optics Communications*, 351(0):45–49, 2015.

[127] A. H. Toor and M. S. Zubairy. Validity of the effective hamiltonian in the two-photon atom-field interaction. *Physical Review A*, 45(7):4951–4959, 1992.

[128] Anatoly A. Svidzinsky, Jun-Tao Chang, and Marlan O. Scully. Cooperative spontaneous emission of $N$ atoms: Many-body eigenstates, the effect of virtual lamb shift processes, and analogy with radiation of $N$ classical oscillators. *Physical Review A*, 81(5):053821, 2010.

[129] Hui Xia, Anatoly A. Svidzinsky, Luqi Yuan, Chao Lu, Szymon Suckewer, and Marlan O. Scully. Observing superradiant decay of excited-state helium atoms inside helium plasma. *Physical Review Letters*, 109(9):093604, 2012.

[130] Luqi Yuan, Dmitry Pestov, Robert K. Murawski, Gombojav O. Ariunbold, Miaochan Zhi, Xi Wang, Vladimir A. Sautenkov, Yuri V. Rostovtsev, Torsten Siebert, and Alexei V. Sokolov. Tracking molecular wave packets in cesium dimers by coherent Raman scattering. *Physical Review A*, 86(2):023421, 2012.

[131] Gombojav O. Ariunbold, Vladimir A. Sautenkov, and Marlan O. Scully. Switching from a sequential transition to quantum beating in atomic rubidium pumped by a femtosecond laser. *Journal of the Optical Society of America B*, 28(3):462–467, 2011.

# APPENDIX A

# USING PUMP PULSE WAVELENGTH AS CONTROL PARAMETER

We try to analyze the theory part of Ref. [131], to see how to manipulate the interference by controlling the central wavelength of pump pulses. The perturbation expansion in the interaction picture is used.

The Hamiltonian is

$$H = H_0 + H_I, \tag{A.1}$$

$$H_0 = \hbar\omega_a|a\rangle\langle a| + \hbar\omega_{b_1}|b_1\rangle\langle b_1| + \hbar\omega_{b_2}|b_2\rangle\langle b_2| + \hbar\omega_c|c\rangle\langle c|, \tag{A.2}$$

$$H_I = \left(-\wp_{ab_1}|a\rangle\langle b_1| - \wp_{ab_2}|a\rangle\langle b_2| - \wp_{b_1c}|b_1\rangle\langle c| - \wp_{b_2c}|b_2\rangle\langle c|\right) E(t) + H.C.. \tag{A.3}$$

where H. C. is Hermite conjugate. So

$$\begin{aligned} \mathscr{V}(t) = \quad & -\tfrac{\hbar}{2}[\Omega_{ab_1}e^{i(\omega_{ab_1}-\nu)t}|a\rangle\langle b_1| + \Omega_{ab_2}e^{i(\omega_{ab_1}-\nu)t}|a\rangle\langle b_2| + \Omega_{b_1c}e^{i(\omega_{ab_1}-\nu)t}|b_1\rangle\langle c| \\ & +\Omega_{b_2c}e^{i(\omega_{ab_1}-\nu)t}|b_2\rangle\langle c|] + H.C., \end{aligned} \tag{A.4}$$

We will use

$$U_I(t) = 1 - \frac{i}{\hbar}\int_0^t dt_1\mathscr{V}(t_1) + \left(-\frac{i}{\hbar}\right)^2\int_0^t dt_1\int_0^{t_1} dt_2\mathscr{V}(t_1)\mathscr{V}(t_2) + \cdots, \tag{2.28 revisited}$$

to find $c_a$, and $|c_a|^2$ is proportional to the Yoked SF signal shown in blue in Figure A.1.

Assume that $|\psi_I\rangle = \sum_i c_i|i\rangle$, and in derivation made following assumptions are used:

I) SF is much faster than spontaneous decay so only coherent processes are with

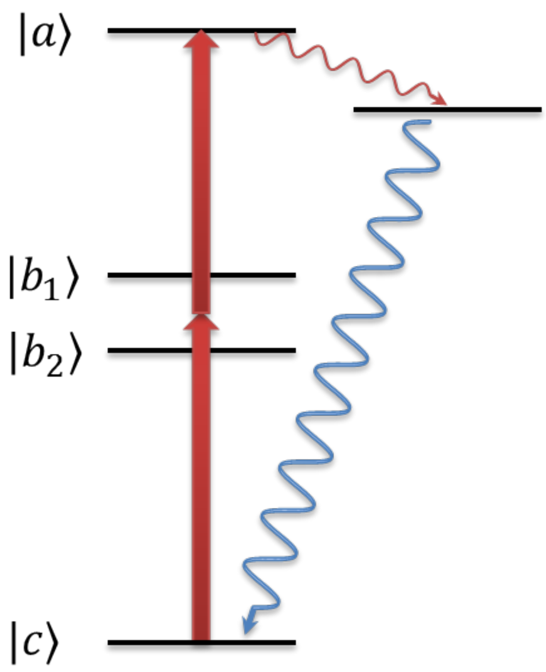

Figure A.1: Energy diagram of a five-level system.

consideration;

II) Instantaneous excitation of atoms, because the pulse is very short and the form of input is $\Omega_i = \sqrt{A_i}\,[\delta(t) + \delta(t+\tau)e^{i\nu\tau}]$;

III) Initial state is the ground state, that is $c_c = 1$;

IV) $A(\lambda) = e^{-\frac{(\lambda-\lambda_c)^2}{\Delta\lambda^2}}$, and $A_1 = A(\lambda = 780\,\text{nm})$, $A_2 = A(\lambda = 795\,\text{nm})$, where $\lambda_c$ is the center wavelength of the ultra-fast pulse;

V) SF determines the decay of $|a\rangle$ state, thus a factor of $e^{-\frac{\tau^2}{\tau_{SF}^2}} + \text{const.}$ is need to describe the decay;

VI) Rotating Wave Approximation;

VII) Resonant coupling, thus $A_1$ couples $|c\rangle \to |b_1\rangle$ while $A_2$ couples $|c\rangle \to |b_2\rangle$;

Based on these assumptions, the first integral of Eqn. (2.28) gives

$$\begin{aligned} & \tfrac{\hbar}{2}\left[\sqrt{A_1}\left(|a\rangle\langle b_1| + |b_1\rangle\langle c| + e^{-i\omega_{ab_1}\tau}|a\rangle\langle b_1| + e^{-i\omega_{b_1c}\tau}|b_1\rangle\langle c|\right)\right] \\ + \;\; & \tfrac{\hbar}{2}\left[\sqrt{A_2}\left(|a\rangle\langle b_2| + |b_2\rangle\langle c| + e^{-i\omega_{ab_2}\tau}|a\rangle\langle b_2| + e^{-i\omega_{b_2c}\tau}|b_2\rangle\langle c|\right)\right] + H.C., \end{aligned} \tag{A.5}$$

and the second integral (we only collects the terms that has $|a\rangle\langle c|$) gives

$$\frac{\hbar^2}{4}\left[A_1\left(1 + e^{-i\omega_{b_1c}\tau} + e^{-i\omega_{ab_1}\tau} + e^{-i\omega_{ac}\tau}\right) + A_2\left(1 + e^{-i\omega_{b_2c}\tau} + e^{-i\omega_{ab_2}\tau} + e^{-i\omega_{ac}\tau}\right)\right]|a\rangle\langle c|. \tag{A.6}$$

So we find that $|c_a|^2$ is

$$\begin{aligned} |c_a|^2 = \; \tfrac{1}{16}\Bigg\{ \; & A_1^2\left(4 + 4\cos\omega_{b_1c}\tau + 4\cos\omega_{ab_1}\tau + 2\cos\omega_{ac}\tau + 2\cos\Delta_1\tau\right) \\ + \;\; & A_2^2\left(4 + 4\cos\omega_{b_2c}\tau + 4\cos\omega_{ab_2}\tau + 2\cos\omega_{ac}\tau + 2\cos\Delta_2\tau\right) \\ + \;\; & 4A_1A_2\left[1 + \sum_{i=b_1,b_2}\left(\cos\omega_{ai}\tau + \cos\omega_{ic}\tau\right) + \cos\omega_{ac}\tau + \cos\Delta_0\tau + \cos\Delta_3\tau\right]\Bigg\}, \end{aligned} \tag{A.7}$$

where $\Delta_0 = \omega_{b_1c} - \omega_{b_2c}$, $\Delta_1 = \omega_{ab_1} - \omega_{b_1c}$, $\Delta_2 = \omega_{ab_2} - \omega_{b_2c} = \Delta_1 + 2\Delta_0$ and $\Delta_3 = \omega_{ab_1} - \omega_{b_2c} = \omega_{ab_2} - \omega_{b_1c} = \Delta_0 + \Delta_1$. When averaged over time scale of $1/\Delta_i$, $i = 0, 1, 2, 3$ , the signal is proportional to

$$\frac{1}{8}(e^{-\frac{\tau^2}{\tau_{SF}^2}} + C)\left[2A_1^2 + 2A_2^2 + 2A_1A_2 + A_1^2\cos\Delta_1\tau + A_2^2\cos\Delta_2\tau + 2A_1A_2\left(\cos\Delta_0\tau + \cos\Delta_3\tau\right)\right]. \tag{A.8}$$

The plot of Eqn. (A.8) with parameters matches the experimental condition is shown in Figure A.2.

As we can see, controlling the center wavelength of pump pulses in a presence of intermediate resonant levels indeed can be used as a control parameter effectively.

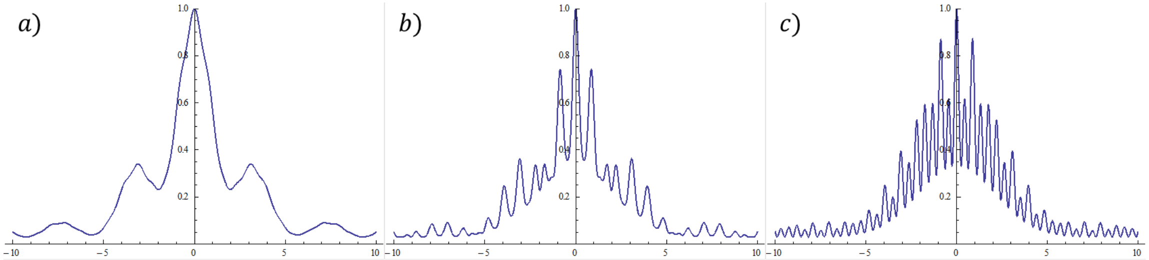

Figure A.2: (From left to right) Different beat pattern for center wavelength ($\lambda_c$) of a) 770, b) 785 and c) 795 nm. Other parameters used are $\Delta_0 = 1$, $\Delta_1 = 0.27$, $\Delta\lambda = 12$, $\tau_{SF} = 3$ and $C = 0.1$.

# APPENDIX B

## DETAIL CALCULATION FOR DUAL PATH QUANTUM BEAT

Effective atom-field interaction Hamiltonian can be written as [3, 127]

$$\begin{aligned}\mathscr{V}(t) = &-\hbar(\Omega_{eff}|a\rangle\langle b| + \Omega_{eff}\mathrm{e}^{-i\Delta_1 t}|c\rangle\langle b| + \Omega_{eff}\mathrm{e}^{-i\Delta_2 t}|d\rangle\langle b| + \Omega_{ae}|a\rangle\langle e| + \Omega_{af}\mathrm{e}^{i\Delta_3 t}|a\rangle\langle f| \\ &+ \Omega_{ce}\mathrm{e}^{-i\Delta_1 t}|c\rangle\langle e| + \Omega_{df}\mathrm{e}^{-i(\Delta_2-\Delta_3)t}|d\rangle\langle f| + \Omega_{de}\mathrm{e}^{-i\Delta_2 t}|d\rangle\langle e| + H.C),\end{aligned} \tag{B.1}$$

where we have sequence pulses such that $\Omega_{eff}$ is pump laser effective Rabi frequency, $\Omega_{ij}$ is probe pulse Rabi frequency which couples $i$ and $j$ states. Detunings are $\Delta_1$ – the energy difference between $9S^{1/2}$ and $7D^{5/2}$, $\Delta_2$ – the energy difference between $9S^{1/2}$ and $7D^{3/2}$ and $\Delta_3$ – the energy difference between $6P^{3/2}$ and $6P^{1/2}$. Our goal is to find the probability of finding atom in the $|e\rangle$ and $|f\rangle$ states by using perturbation theory.

The general solution for SE in the series form is

$$|\psi_I(t)\rangle = U_I|\psi_I(t=0)\rangle, \tag{2.27 revisited}$$

with

$$U_I(t) = 1 - \frac{i}{\hbar}\int_0^t dt_1\mathscr{V}(t_1) + \left(-\frac{i}{\hbar}\right)^2\int_0^t dt_1\int_0^{t_1} dt_2\mathscr{V}(t_1)\mathscr{V}(t_2) + \cdots, \tag{2.28 revisited}$$

We calculated this series up to fourth order, because only second and fourth order

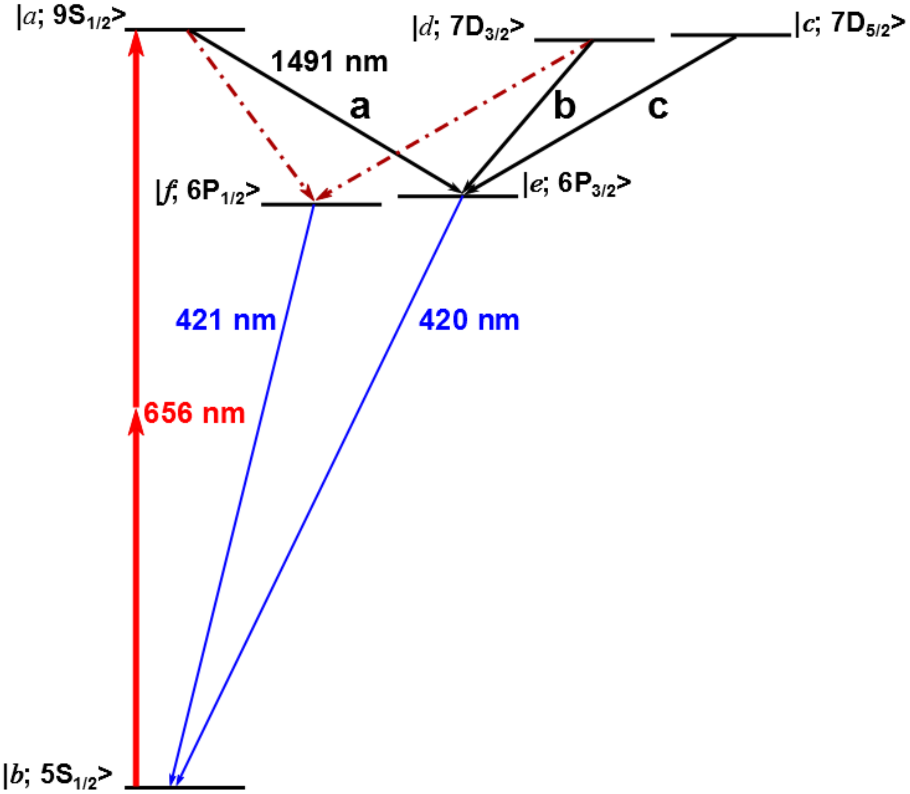

Figure B.1: Simplified energy level diagram of $^{87}$Rb. Broadband pump pulse excites atoms from $5S$ to $9S$ and $7D$ levels; probe pulse couples $9S$ and $7D$ to $6P$ levels.

terms give us $|e\rangle$ and $|f\rangle$ terms. Second order term is

$$-\left(3|\Omega_p|^2|b\rangle + \Omega_p(\Omega_{ae}^* + \Omega_{ce}^*\mathrm{e}^{i\Delta_1\tau} + \Omega_{de}^*\mathrm{e}^{i\Delta_2\tau})|e\rangle + \Omega_p(\Omega_{af}^*\mathrm{e}^{-i\Delta_3\tau} + \Omega_{df}^*\mathrm{e}^{i(\Delta_2-\Delta_3)\tau})|f\rangle\right), \tag{B.2}$$

and fourth order term is

$$\begin{aligned} &\Omega_p^*(K+L+M)|b\rangle+ \\ &(K\Omega_{ae}^* + L\Omega_{ce}^*\mathrm{e}^{i\Delta_1\tau} + M\Omega_{de}^*\mathrm{e}^{i\Delta_2\tau})|e\rangle+ \\ &(K\Omega_{af}^*\mathrm{e}^{-i\Delta_3\tau} + M\Omega_{df}^*\mathrm{e}^{i(\Delta_2-\Delta_3)\tau})|f\rangle \end{aligned} \tag{B.3}$$

$$,$$

where

$$\begin{aligned} K &= \Omega_p(3|\Omega_p|^2 + |\Omega_{ae}|^2 + |\Omega_{af}|^2 + \Omega_{ce}^*\Omega_{ae}\mathrm{e}^{i\Delta_1\tau} + (\Omega_{de}^*\Omega_{c1} + \Omega_{df}^*\Omega_{af})\mathrm{e}^{i\Delta_2\tau}), \\ L &= \Omega_p(3|\Omega_p|^2 + |\Omega_{ce}|^2 + \Omega_{ae}^*\Omega_{ce}\mathrm{e}^{-i\Delta_1\tau} + \Omega_{de}^*\Omega_{ce}\mathrm{e}^{i(\Delta_2-\Delta_1)\tau}), \\ M &= \Omega_p(3|\Omega_p|^2 + |\Omega_{df}|^2 + |\Omega_{de}|^2 + (\Omega_{ae}^*\Omega_{de} + \Omega_{af}^*\Omega_{df})\mathrm{e}^{-i\Delta_2\tau} + \Omega_{cd}^*\Omega_{de}\mathrm{e}^{i(\Delta_1-\Delta_2)\tau}). \end{aligned} \tag{B.4}$$

We are interested only in the probability of atoms in the states $|e\rangle$ and $|f\rangle$, which are

$$\begin{aligned} P_e &= |\Omega_p(\Omega_{ae}^* + \Omega_{ce}^*\mathrm{e}^{i\Delta_1\tau} + \Omega_{de}^*\mathrm{e}^{i\Delta_2\tau}) + (K\Omega_{ae}^* + L\Omega_{ce}^*\mathrm{e}^{i\Delta_1\tau} + M\Omega_{de}^*\mathrm{e}^{i\Delta_2\tau})|^2, \\ P_f &= |\Omega_p(\Omega_{af}^*\mathrm{e}^{-i\Delta_3\tau} + \Omega_{df}^*\mathrm{e}^{i(\Delta_2-\Delta_3)\tau}) + (K\Omega_{af}^*\mathrm{e}^{-i\Delta_3\tau} + M\Omega_{df}^*\mathrm{e}^{i(\Delta_2-\Delta_3)\tau})|^2. \end{aligned} \tag{B.5}$$

Further simplification leads to results in Eqn. (7.3) and (7.4).